

# **Dosimetry of Ionizing Radiation in Magnetic Fields**

## **Dissertation**

der Mathematisch-Naturwissenschaftlichen Fakultät  
der Eberhard Karls Universität Tübingen  
zur Erlangung des Grades eines  
Doktors der Naturwissenschaften  
(Dr. rer. nat.)

vorgelegt von  
M.Sc. Stefan Matthias Pojtinger  
aus Freudenstadt

Tübingen  
2021

Gedruckt mit Genehmigung der Mathematisch-Naturwissenschaftlichen Fakultät der  
Eberhard Karls Universität Tübingen.

Tag der mündlichen Qualifikation:

09.06.2021

Dekan:

Prof. Dr. Thilo Stehle

1. Berichterstatter:

Prof. Dr. Daniela Thorwarth

2. Berichterstatter:

Prof. Dr. Dr. Fritz Schick

## Contents

Contents .....	3
Abbreviations .....	4
Zusammenfassung .....	5
Abstract .....	7
List of Publications .....	8
Introduction .....	9
External Beam Radiotherapy .....	9
Linear Accelerators for Radiation Oncology .....	9
Quality Assurance .....	11
Absolute Dosimetry .....	12
Monte Carlo Simulations .....	19
Fundamental Quantities .....	19
Boltzmann Transport Equation .....	20
Condensed History Algorithms .....	22
Cross Sections .....	23
Photon Cross Sections .....	24
Electron Cross Sections .....	28
Magnetic Resonance Imaging Guided Radiotherapy .....	31
Workflow of External Beam Radiotherapy .....	31
Image-guided Radiotherapy .....	31
MR-linacs .....	32
Consequences for the Absorbed Dose .....	35
Influence of Air Cavities .....	37
Effects on Monte Carlo Simulations .....	39
Objectives .....	43
Results and Discussion .....	45
Change of Response of Ionization Chambers .....	45
Formalism .....	47
Chemical Radiation Detectors in MRgRT-Dosimetry .....	49
Magnetic Field Correction Factors for Parallel Ionization Chamber Orientations .....	51
Monte-Carlo Simulations .....	53
Dead Volumes .....	54
Conclusions for Magnetic Field Correction Factors .....	56
Literature .....	61

## Abbreviations

<b>BTE</b>	Boltzmann transport equation
<b>CBCT</b>	cone-beam computed tomography
<b>CH</b>	condensed history
<b>CT</b>	computed tomography
<b>EBRT</b>	external beam radiotherapy
<b>ERE</b>	electron return effect
<b>ESR</b>	electron spin resonance
<b>FFF</b>	flattening-filter-free
<b>ICRU</b>	International Commission on Radiation Units and Measurements
<b>IGRT</b>	image-guided radiotherapy
<b>IMRI</b>	intensity-modulated radiotherapy
<b>Linac</b>	linear accelerator
<b>MC</b>	Monte Carlo
<b>MRI</b>	magnetic resonance imaging
<b>MRIGRT</b>	magnetic resonance imaging guided radiotherapy
<b>MRI</b>	magnetic resonance tomograph
<b>PTB</b>	Physikalisch-Technische Bundesanstalt
<b>RTP</b>	radiation treatment plan
<b>SAD</b>	source-to-axis distance
<b>SID</b>	source-to-isocenter distance
<b>SSD</b>	source-to-surface distance
<b>TPS</b>	treatment planning system

## Zusammenfassung

Magnetresonanz-geführten Strahlentherapie (MRIgRT) ist eine neue Modalität der Strahlentherapie. Die Vorteile gegenüber der konventionellen bildgeführten Strahlentherapie ergeben sich aus dem erhöhten Weichteilkontrast sowie der Möglichkeit der Online-Bildgebung. Seit wenigen Jahren stehen an vielen Kliniken die ersten Geräte für diese Form der Strahlentherapie zur Verfügung (MR-linacs). MR-linacs erlauben eine Bildgebung mittels Magnetresonanztomographie und verfügen zusätzlich über einen integrierten Linearbeschleuniger zur Bestrahlung von Patienten. Der grundlegende Gedanke ist, die Bildgebung mittels Magnetresonanztomographie unmittelbar vor oder sogar während der Bestrahlung des Patienten zu ermöglichen. Da sich das magnetische Feld eines MR-linacs aber nur mit großem Aufwand abschalten lässt, müssen Messungen zur Qualitätssicherung unter dem Einfluss eines starken magnetischen Feldes durchgeführt werden. Eine Komplikation ist hierbei, dass das Ansprechvermögen typischer Detektoren zur Messung der Strahlendosis durch magnetische Felder beeinflusst wird. Aus diesem Grund können die derzeitigen Protokolle zur Referenzdosimetrie nicht an MR-linacs verwendet werden. Das Ziel dieser Arbeit war die Erarbeitung der wissenschaftlichen Grundlagen für ein neues Protokoll für die Referenzdosimetrie in der MRIgRT.

In dieser Arbeit wurden verschiedene experimentelle Methoden zur Charakterisierung von Detektoren zur Messung der Strahlendosis unter dem Einfluss magnetischer Felder erarbeitet. Eine dieser Methoden beruht auf Messungen, welche unter anderem an einem experimentellen Aufbau durchgeführt wurden. Hierzu wurde ein großer Elektromagnet vor einem konventionellen medizinischen Linearbeschleuniger positioniert. Weiterhin wurden Messungen an verschiedenen MR-linacs durchgeführt. Zusätzlich wurde eine Methode zur Berechnung der Effekte entwickelt. Hierbei wurde einer Kombination aus Monte-Carlo-Simulationen und Finite-Element-Berechnungen verwandt.

Die Ergebnisse bestätigen, dass das Ansprechvermögen von Ionisationskammern durch magnetische Felder beeinflusst wird. Die Änderung des Ansprechvermögens hängt hierbei von verschiedenen Einflussfaktoren ab. Die wichtigsten Einflussfaktoren sind die Geometrie der Ionisationskammer, die magnetische Flussdichte und die Orientierung der Ionisationskammer. Korrekturfaktoren für den Einfluss des magnetischen Feldes auf verschiedene Ionisationskammern wurden tabelliert. Diese Korrekturfaktoren wurden durch die Verwendung chemischer Strahlungsdetektoren

verifiziert. Die hier ermittelten Korrekturfaktoren können somit für dosimetrische Messungen in der MRIgRT verwendet werden. Es wurde gezeigt, dass das übliche Vorgehen zur Simulation von Ionisationskammern in magnetischen Feldern angepasst werden muss. Hierzu wurde eine neue Methode entwickelt, welche solche Simulationen ermöglicht. Zusätzlich wurden Richtlinien zur Referenzdosimetrie unter dem Einfluss magnetischer Felder erarbeitet und somit die Grundlagen für ein neues Protokoll zur Referenzdosimetrie in der MRIgRT geschaffen.

## Abstract

Magnetic resonance imaging guided radiotherapy (MRIgRT) is a new modality in radiotherapy. The benefits over conventional imaging guided radiotherapy are an increase in soft tissue contrast and the option of real time imaging. Recently, many clinics implemented first devices for this form of therapy (MR-linacs). These new devices offer magnetic resonance imaging but also include a linear accelerator for the treatment of patients. The idea is, that a magnetic resonance image can be acquired immediately before as well as during the irradiation of the patient. As the magnetic field of MR-linacs cannot be shut down easily, measurements for quality assurance are done under the influence of a strong magnetic field. Unfortunately, the magnetic field affects the response of radiation detectors. Because of this, current protocols for reference dosimetry are not applicable for MR-linacs. The aim of this work was to lay the foundations for a new protocol for reference dosimetry for MRIgRT.

In this work, several experimental methods were established for the characterization of radiation detectors under the influence of magnetic fields. These included measurements at an experimental setup, that combined a big electromagnet with a conventional linac as well as measurements at MR-linacs. In addition, a simulation method for the quantification of the effects of magnetic fields on the response of ionization chambers has been developed by combining finite element with Monte-Carlo methods.

The response of ionization chambers is influenced by magnetic fields. The change of response depends on several conditions, the most important are the geometry of the ionization chamber, the magnetic flux density, and the orientation of the ionization chamber. A dataset of magnetic field correction factors was derived for different types of ionization chambers. These correction factors have been validated by utilizing chemical radiation detectors. The derived correction factors can be used for dosimetry in MRIgRT. It was shown that the way in which Monte Carlo simulation of ionization chambers are done has to be adapted to account for an external magnetic field. A new technique has been developed to overcome the issues found for Monte Carlo simulations. Guidelines have been derived for reference dosimetry under the influence of a magnetic field. The foundation for a new protocol for reference dosimetry for MRIgRT were set in this work and Monte-Carlo methods were refined so that they can be used the questions related to MRIgRT in clinical radiation oncology.

## List of Publications

### **Ionization chamber correction factors for MR-linacs**

**Pojtinger, S.**, Dohm, O.S., Kapsch, R.-P., Thorwarth, D. (2018)  
Physics in Medicine & Biology. Institute of Physics, 63(11), p. 11NT03  
DOI: 10.1088/1361-6560/aac4f2

*Pojtinger, S. participated in the formulation of the scientific problem and took over the major part in the formulation of the research program, conduction of measurements, analysis of the results and writing of the manuscript.*

### **A finite element method for the determination of the relative response of ionization chambers in MR-linacs: simulation and experimental validation up to 1.5 T**

**Pojtinger S.**, Kapsch R.-P., Dohm O.S., Thorwarth D. (2019)  
Physics in Medicine & Biology. Institute of Physics, 64(13), p. 135011  
DOI: 10.1088/1361-6560/ab2837

*Pojtinger, S. took over the major part in the formulation of the scientific problem, formulation of the research program, conduction of measurements, analysis of the results and writing of the manuscript.*

### **Chemical radiation dosimetry in magnetic fields: characterization of a Fricke-type chemical detector in 6 MV photon beams and magnetic fields up to 1.42 T**

Trachsel, M. A., **Pojtinger, S.**, Meier, M., Schrader, M., Kapsch, R.-P., Kottler, C. (2020)  
Physics in Medicine & Biology. Institute of Physics, 65(6), p. 065005  
DOI: 10.1088/1361-6560/ab7360

*Pojtinger, S. participated in the formulation of the research program, conduction of measurements, analysis of the results and writing of the manuscript.*

### **Experimental determination of magnetic field correction factors for ionization chambers in parallel and perpendicular orientations**

**Pojtinger, S.**, Nachbar, M., Ghandour, S., Pisaturo, O., Pachoud, M., Kapsch, R.-P., Thorwarth, D. (2020)  
Physics in Medicine & Biology. Institute of Physics, 65(24), p. 245044  
DOI: 10.1088/1361-6560/abca06

*Pojtinger, S. took over the major part in the formulation of the scientific problem, formulation of the research program, conduction of measurements, analysis of the results and writing of the manuscript.*



## Introduction

### External Beam Radiotherapy

According to the Global Burden of Disease 2016 Study (Naghavi *et al* 2017) neoplasms are the second leading cause of death worldwide. Furthermore, the number of new cases increases every year. With regard to the “best available evidence”, 52% of cancer patients should be treated by radiotherapy (Delaney *et al* 2005). Therefore, there is already a large and still increasing need for advances in radiotherapy techniques, like external beam radiotherapy (EBRT).

EBRT is carried out by exposing the tumorous tissue to ionizing radiation. For this purpose, different types of particle accelerators and radioactive sources are used to produce ionizing radiation. A common method is to accelerate electrons and direct these on a high-Z material to produce Bremsstrahlung. Then, this Bremsstrahlung is collimated to a treatment beam which is directed on the tumor. The ideal collimation and beam direction are calculated based on detailed Monte Carlo (MC) simulations of the radiation transport through the patient’s anatomy. In most cases, the aim of radiotherapy is to maximize the number of ionizations in the tumorous tissue, while sparing the healthy tissue.

The content of this thesis is focused on radiotherapy with X-rays. Though, there are many other particles that can be used for radiotherapy, like electrons, protons and heavy ions.

### Linear Accelerators for Radiation Oncology

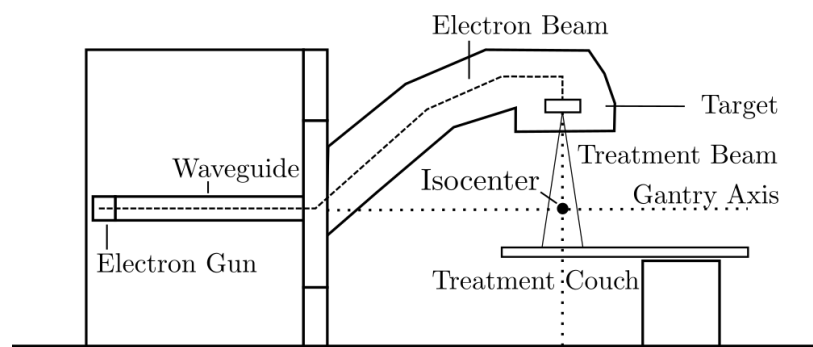


Figure 1: Schematic illustration of a typical linear accelerator used for radiation oncology. The position of the accelerating waveguide can differ for different linacs.

Figure 1 shows the main components of a linear accelerator (linac) for radiation oncology. The electron gun generates free electrons by thermionic emission. Then, the electrons are injected into an accelerating waveguide. Usually, a magnetron is used to

generate microwaves, which in turn generate radio frequency fields in the accelerating waveguide to bunch and accelerate the electrons. Many linacs are traveling wave accelerators, hence the nominal accelerating voltage can be changed easily. The magnetron as well as the electron gun are pulsed with a pulse repetition frequency of several hundred Hz. Focusing and steering magnets are used to direct the electron beam through a gantry that can be rotated around the gantry axis. This allows multiple beam directions. The target for Bremsstrahlung production is placed in the accelerator head. The accelerator head also includes a complex collimator system to form the emerging photon beam and a transmission ionization chamber (monitor chamber) to monitor the linac's output.

The spectral fluence of the Bremsstrahlung photons depends on the nominal accelerating voltage that is used to accelerate the electrons. For medical linacs, it is common to note the nominal accelerating voltage as a specifier for the photon energy. For example, a linac that produces Bremsstrahlung photons by accelerating electrons with a nominal accelerating voltage of 6 MV is often called a 6 MV linac. Figure 2 shows the spectral fluence of a typical 6 MV linac (Precice, Elekta AB, Stockholm, Sweden). To achieve a flat beam profile, most linacs include a cone-shaped flattening filter behind the target. This also reduces the fluence of photons at the isocenter. If the flattening filter is removed, the beam or accelerator is called flattening-filter-free (FFF). Modern irradiation techniques do not depend on a flat beam profile. Thus, the usage of FFF beams became more common in the recent years.

The intersection of the treatment beam axis and the gantry axis is referred to as isocenter (figure 1). Usually, the collimation of the treatment beam is calibrated to produce certain field sizes on isocenter level. E.g. a  $10 \times 10 \text{ cm}^2$  beam describes a treatment beam, that is collimated to a  $10 \times 10 \text{ cm}^2$  square area at the isocenter. In most treatment scenarios, the tumor is aligned with the isocenter. The field shapes that are used for the treatment of patients are much more complex than square fields. The distance between the target and the gantry axis is called source-to-axis distance (SAD) and the distance between the source and the isocenter is called source-to-isocenter distance (SID). It is common practice to do the measurements that are needed for the calibration and quality assurance of the linac by irradiation of radiation detectors that are placed inside of a water tank or similar (phantom). In this experimental scenario, the distance

between the target and the surface of the phantom is called source-to-surface distance (SSD).

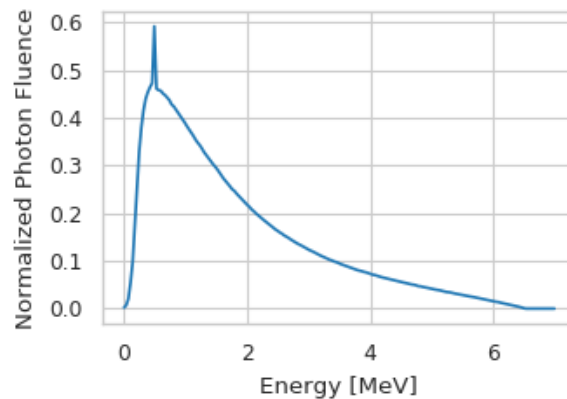


Figure 2: MC simulated spectral photon fluence of a 6 MV linac. The peak at 511 keV is caused by annihilation radiation.

### Quality Assurance

The amount of ionizing radiation, that is prescribed for the irradiation of a tumor is characterized by the absorbed dose ( $D$ ) in the units of gray (Gy). “The absorbed dose is the quotient of  $d\bar{\epsilon}$  by  $dm$ , where  $d\bar{\epsilon}$  is the mean energy imparted to matter of mass  $dm$ ”, (Allisy *et al* 1998):

$$D = \frac{d\bar{\epsilon}}{dm}$$

Physically, the energy transfer is caused by many different scattering and absorption processes that will be described later. The absorbed dose depends on the irradiation conditions but also on the irradiated material. For example, the absorbed dose to graphite differs from the absorbed dose to water, for the same irradiation conditions. In clinical practice, particle accelerators for radiotherapy are calibrated by measuring the absorbed dose to water in a certain reference setup. Achieving low uncertainties on this calibration is critical for the success of radiation therapy: “by increasing the precision of the delivery of dose, the cure of early stage patients increases at a rate of about 2% per 1% improvement of accuracy”, (Boyer and Schultheiss 1988). Methods for this calibration are described in detail in many national and international protocols for reference dosimetry. The best-known protocols for reference dosimetry are the protocol of the American Association of Physicists in Medicine (AAPM) Task Group 51 (TG-51, Almond *et al.*, 1999), the protocol of the International Atomic Energy Agency

(IAEA) (TRS-398, Andreo et al., 2000) and in Germany the German standard (DIN 6800-2, Deutsches Institut für Normung, 2020).

The most used detectors for calibration measurements are air-filled ionization chambers due to their good long-time stability and low energy dependence. But with the advent of new modalities and devices in EBRT, the suitability of air-filled ionization chambers needs to be reassessed for the respective conditions.

### Absolute Dosimetry

The term absolute dosimetry is used to describe measurements of the absorbed dose to a medium (usually water) in absolute values. Absolute dosimetry differs from relative dosimetry, that describes the measurement of relative beam characteristics, like the shape of a photon beam profile. The most common way to measure the absolute dose to water is by irradiation of a detector (like an ionization chamber) inside of a water phantom.

### Ionization Chamber Measurements

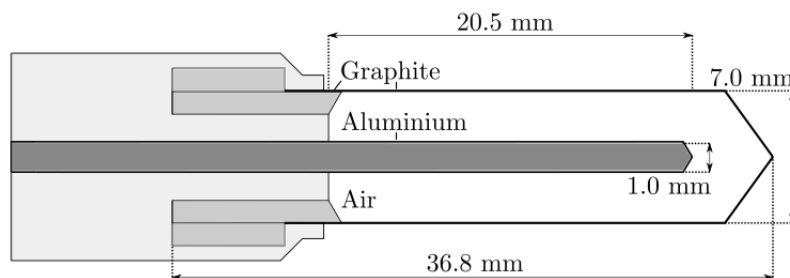


Figure 3: Design of a Farmer type ionization chamber, measures taken from the literature (Aird and Farmer 1972).

The type of ionization chamber most frequently used for absolute dosimetry in linac photon radiation fields is the Farmer type ionization chamber (figure 3). The design was originally presented by Farmer (Farmer 1944) and modified later, as described by Aird and Farmer (Aird and Farmer 1972). An electric voltage of several hundred volts is set between the aluminum central electrode (collector) and the outer graphite wall. Because of the resulting electric field, charges that are produced inside of the sensitive volume travel either to the collector or to the wall of the ionization chamber. An electrometer is connected to the collector to measure charges that arrive at the collector (figure 4).

To avoid any leakage between the collector and the wall (that can occur near the stem of the ionization chamber), modern designs include a guard ring (figure 4). The guard

is set to the same electric potential as the collector but is not connected to the electrometer.

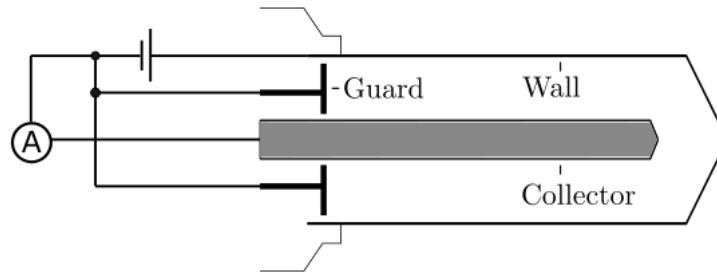


Figure 4: Illustration of the functional parts of an ionization chamber and the corresponding electric circuit. Charges that arrive at the guard are not seen by the electrometer.

If an air-filled ionization chamber is irradiated in a photon field of ionizing radiation, the charge that is produced inside of the sensitive volume ( $Q_{ch}$ ) is proportional to the absorbed dose to air ( $D_{air}$ ):

$$Q_{ch} \sim D_{air}$$

Typically, ionization chambers are placed inside of a water tank for irradiation. In this scenario, the primary photons generate secondary electrons inside of the water tank. For most secondary electrons, the kinetic energy is too high for them to be caught by the electric field inside of the ionization chamber. Hence, most secondary electrons pass through the sensitive volume of the ionization chamber in a straight line. But while passing the sensitive volume, the secondary electrons generate more generations of charged particles. These charged particles follow the electric field lines and are detected by the electrometer. In this sense, ionizations inside of the ionization chamber can be caused by photons as well as by electrons. If the ionization chamber is small compared to the range of the passing particles and all of the energy deposition is caused by charged particles (Bragg-Gray conditions),  $D_{air}$  can be used to determine the absorbed dose to the medium surrounding the ionization chamber ( $D_{med}$ ) by multiplying  $D_{air}$  with the electron stopping-power ratio  $s$  (Ma and Nahum 1991).

$$D_{med} = D_{air} s$$

This equation applies only to high photon energies. For low photon energies, the energy deposition that is caused by photons increases inside of the air cavity, what invalidates the Bragg-Gray conditions (Ma and Nahum 1991).

It has been shown, that the mean energy needed for the creation of an ion pair in air ( $W_{\text{air}}$ ) is constant for the typical energy range of medical accelerators (Burns *et al* 2014). Therefore, the absorbed dose in a medium surrounding an ideal Bragg-Gray detector can be calculated as:

$$D_{\text{med}} = \frac{Q_{\text{ch}}}{m_{\text{air}} e} W_{\text{air}} s$$

But the calculation of  $D_{\text{med}}$  introduces several challenges. One is the exact determination of  $m_{\text{air}}$ . This is problematic as the sensitive volume of the ionization chamber is not necessarily the same as the geometrical volume of the ionization chamber (Pojtinger *et al* 2019, Ross 2009, Boag 1964). Also, ionization chambers do not completely fulfil the Bragg-Gray conditions and must be corrected for several perturbation effects.

One approach to overcome this issue is to determine a calibration factor  $N$  by cross-calibration with other detectors:

$$N = \frac{W_{\text{air}}}{m_{\text{air}} e} s = D_{\text{med}}/Q_{\text{ch}}$$

Ionization chambers that are used in clinical practice rely on a calibration factor  $N$  that has been determined by a measurement of  $D_{\text{med}}/Q_{\text{ch}}$ . Usually manufacturers determine these calibration factors by cross-calibration with another ionization chamber, that has been calibrated previously at a primary or secondary standards dosimetry lab. In Germany, the primary standard for the absorbed dose to water is realized by a water calorimeter maintained at the Physikalisch-Technische Bundesanstalt (PTB, Braunschweig) (figure 5).

In addition, the signal of the ionization chamber ( $M$ ) is not necessarily equal to  $Q_{\text{ch}}$ . In fact, the ratio of  $M$  and  $Q_{\text{ch}}$ , depends on several conditions. The most important are:

- air pressure and temperature
- saturation effects
- polarity of applied voltage
- radiation quality (type of particles and spectral fluence of the treatment beam)

Therefore, a set of corrections must be applied, that are usually called correction factors  $k_i$ :

$$Q_{\text{ch}} = M \prod_i k_i \rightarrow D_{\text{med}} = N M \prod_i k_i$$

The correction for the radiation/beam quality is usually called  $k_Q$ . The calculation of  $k_Q$  often relies on a measurement of the beam quality specifier  $TPR_{20,10}$ , what described in detail in the literature (Andreo *et al* 2006).

The correction for air pressure and temperature is usually called  $k_p$ , the correction for saturation effects  $k_s$  and for the polarity  $k_p$ . Methods to determine these correction factors are described in details in the protocols for reference dosimetry (Almond *et al* 1999, Andreo *et al* 2006, Deutsches Institut für Normung 2020) and can vary for different protocols.



Figure 5: Detector of the water calorimeter that is used for the primary standard of absorbed dose to water at PTB (Braunschweig). A detailed description of the calorimeter can be found in the literature (Krauss 2006).

### *Reference Conditions*

In a clinical setting, measurements of the absolute dose to water should be done under reference conditions. Reference conditions are described in the protocols for reference dosimetry (Almond *et al* 1999, Andreo *et al* 2006, Deutsches Institut für Normung 2020). These include conditions for the collimation of the photon beam and the positioning of the ionization chamber. The measurement of the absorbed dose to water under reference conditions is used to cross-calibrate a transmission ionization chamber that is permanently placed inside of the linacs accelerator head (internal monitor chamber) with the ionization chamber that is irradiated in the reference setup. After the calibration of the internal monitor chamber, this internal monitor chamber is used to monitor the beam output during the irradiation of patients. Typical reference conditions for a 6 MV linac are SSD = 100 cm, a field size of  $10 \times 10 \text{ cm}^2$  and a measurement depth of 10 cm.

Measurements under non-reference conditions are possible but additional corrections must be applied. One example is a measurement in a small photon field. As the sensitive volume of an ionization chamber might not be fully covered by the dose profile, and the dose response of an ionization chamber varies over the sensitive volume, an additional correction  $k_V$  must be applied.

### *Chemical Detector Systems for Absolute Dosimetry:*

#### *Alanine*

In the work of Regulla and Deffner (Regulla and Deffner 1982), the authors gave a detailed description on the principles of alanine dosimetry. The following is a brief description of the most important points.

Alanine is an amino acid that forms several radical species under irradiation and can be purified in crystalline form. If irradiated in crystalline form, the produced radicals are stable within the medium. For irradiation, alanine is pressed into pellets, that can be positioned in dedicated holders. Alanine pellets consist “of a mixture of crystalline grains and a low-Z binder (typically paraffin or polyethylene)”, (Seltzer *et al* 2014).

After irradiation, the change of the number of free radicals can be determined by electron spin resonance (ESR). A typical ESR setup is shown in figure 6. For the readout process, the probe is placed inside of a resonator cavity. An electromagnet is used to generate a magnetic field inside of the cavity. Due to Zeeman splitting, the magnetic



field splits the energy states of the radicals' unpaired valence electrons depending on the corresponding spin orientations. In addition, microwaves are coupled into the resonator cavity. Then, the magnitude of the magnetic flux density  $B$  is altered, and therefore the energy difference that is needed to excite an electron into the higher Zeeman state  $\Delta E$  changes according to:

$$\Delta E = \mu_B g B$$

In this equation,  $g$  is the Landé-factor and  $\mu_B$  the Bohr magnetron. If  $\Delta E$  matches the energy of the microwave, the microwave is absorbed. As the absorbed energy is small, a phase sensitive amplifier is used to improve the signal to noise ratio (lock-in technique), for the detection of the absorption curve. For this, the magnetic field is modulated with a radio frequency field. Usually, the first derivative of the absorption curve is measured, relative to the magnetic flux density.

For the determination of the absorbed dose, the alanine system is cross-calibrated to another detector. At PTB, the alanine system is calibrated to the water calorimeter that is maintained as the primary standard for the absorbed dose to water.

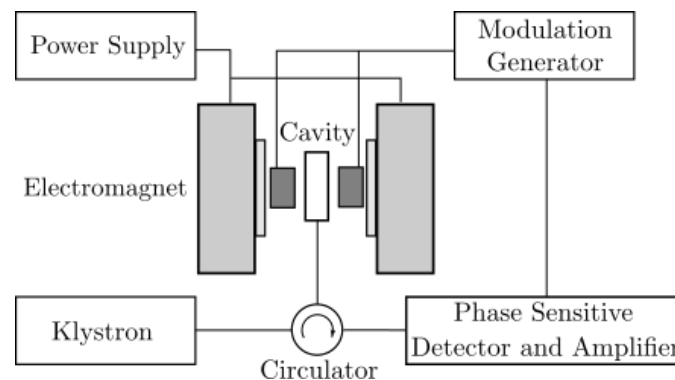


Figure 6: Schematic representation of a setup for ESR-spectrometry.

### Fricke Solution

A detailed description of Fricke dosimetry can be found in the literature (Olszanski *et al* 2002). The section below describes the general concept of this method.

A Fricke solution consists of ferrous ammonium sulfate, sodium chloride, sulfuric acid and water. As the main component is water (96% by weight), the typical radiolysis products are formed during irradiation. The radiolysis products lead to an oxidation of

the ferrous ions ( $\text{Fe}^{2+}$ ) to ferric ions ( $\text{Fe}^{3+}$ ). The change of the concentration of the ferric ions in the Fricke solution is linked to the absorbed dose to the Fricke solution by the chemical yield of the ferric ions ( $G(\text{Fe}^{3+})$ ).  $G(\text{Fe}^{3+})$  depends on the temperature during measurement and changes for different beam energies. The energy dependence is considered by a correction factor  $k_E$ . The ratio between the absorbed dose to water and the absorbed dose to the Fricke solution is called  $R_F^W$ . Additional correction factors must be applied for the perturbation effect of the vial ( $k_{\text{vial}}$ ) and the non-uniformity of the radiation field ( $k_{\text{dd}}$ ).

After the irradiation, the increase of ferric ions can be quantified by measuring the change in the optical density ( $\Delta OD$ ) at a wavelength of 224 nm and 303 nm using spectrophotometry.  $\Delta OD$  is linked to the change of concentration of the ferric ions by the molar extinction coefficient ( $\epsilon$ ), that also depends on the temperature.

Finally, the dose to water can be calculated as:

$$D_W = \frac{\Delta OD}{G(\text{Fe}^{3+}) \epsilon \rho L} R_F^W k_{\text{vial}} k_{\text{dd}} k_E$$

Here,  $\rho$  is the density of the Fricke solution and  $L$  is the optical path length of the spectrometer cuvette. The influence of the temperature during measurement and readout can be corrected, as it is described in (Shortt 1989). The product  $\epsilon G(\text{Fe}^{3+})$  can be determined by water calorimetry.

## Monte Carlo Simulations

The MC method is a “a statistical approach to the study of differential equations, or more generally, of integro-differential equations that occur in various branches of the natural sciences”, (Metropolis and Ulam 1949). Starting from the fifties, the MC method has become a common approach to solve problems in medical physics (Rogers 2006) due to the fact that many problems of radiation physics can be formulated as an integro-differential equation.

Many quantities which are needed for MC simulations in medical physics and for dosimetry in general, were defined by the International Commission on Radiation Units and Measurements (ICRU, Bethesda, USA). The most important quantities and equations that form the foundation of MC simulations for radiation transport are described below. The following definitions are based on ICRU Report 60 (Allisy *et al* 1998) and ICRU Report 90 (Seltzer *et al* 2014).

### Fundamental Quantities

Allisy *et al.* (Allisy *et al* 1998) defined “the cross section,  $\sigma$ , of a target entity, for a particular interaction produced by incident charged or uncharged particles” as:

$$\sigma = \frac{P}{\phi}$$

In this, “ $P$  is the probability of that interaction for a single target entity when subjected to the particle fluence”, (Allisy *et al* 1998). The fluence  $\phi$  “is the quotient of  $dN/d\alpha$ , where  $dN$  is the number of particles incident on a sphere of cross-sectional area  $d\alpha$ ”, (Allisy *et al* 1998).

For a full MC simulation, the cross sections must be known for any interaction and type of particle that is part of the simulation. Also, the cross sections must be known differential in energy and angle.

### Uncharged Particles

The mass attenuation coefficient  $\mu/\rho$  is closely linked to the cross sections for interactions of uncharged particle  $\sigma_j$ . It can be expressed as:

$$\frac{\mu}{\rho} = \frac{N_A}{M} \sum_j \sigma_j$$

Where  $N_A$  is the Avogadro constant and  $M$  is the molar mass of the target material. Allisy et al. (Allisy *et al* 1998) define the quantity as the “quotient of  $\frac{dN}{N}$  by  $\rho dl$ , where  $\frac{dN}{N}$  is the fraction of particles that experience interactions in transferring a distance  $dl$  in the material of density  $\rho$ :

$$\frac{\mu}{\rho} = \frac{1}{\rho} \frac{dN}{dl N}$$

### *Charged Particles*

For charged particles, the ratio of the mean energy  $dE$ , that is lost on a distance  $dl$ , and  $dl$  is called the linear stopping power (Seltzer *et al* 2014):

$$S = \frac{dE}{dl}$$

If the linear stopping power is weighted by  $\rho$ , it is called the mass stopping power (Seltzer *et al* 2014):

$$\frac{S}{\rho} = \frac{1}{\rho} \frac{dE}{dl}$$

Often, the mass stopping power is separated into the “mass electronic (or collision) stopping power due to interactions with atomic electrons resulting in ionization or excitation”, the “mass radiative stopping power due to emission of bremsstrahlung in the electric fields of atomic nuclei or atomic electrons” and the “mass nuclear stopping power due to elastic Coulomb interactions in which recoil energy is imparted to atoms”, (Seltzer *et al* 2014):

$$\frac{S}{\rho} = \frac{1}{\rho} \left( \frac{dE}{dl} \right)_{el} + \frac{1}{\rho} \left( \frac{dE}{dl} \right)_{rad} + \frac{1}{\rho} \left( \frac{dE}{dl} \right)_{nuc}$$

### *Boltzmann Transport Equation*

The transport of particles through matter can be described by the Boltzmann transport equation (BTE). A good example of an application of the BTE is the transport equation for electron transport, as it is implemented in the EGSnrc code system for MC simulations (Kawrakow *et al* 2019). The following formalism is taken from a publication of Kawrakow et al. (Kawrakow *et al* 2019).

The current state of all electrons is described by phase space coordinates. The phase space coordinates are the position  $\vec{x}$ , the direction  $\vec{\Omega}$  and the energy  $E$ . The transport equation links the change of the fluence  $\Phi$  per time interval  $dt$  to a source term  $S$  and a collision integral  $I$ .

$$\frac{d\Phi(\vec{x}, \vec{\Omega}, E, t)}{dt} = S(\vec{x}, \vec{\Omega}, E, t) + vI[\Phi]$$

$S(\vec{x}, \vec{\Omega}, E, t)$  characterizes “the number of electrons with energy  $E$  and velocity  $\vec{v}(v, \vec{\Omega})$  at a position  $\vec{x}$  per unit volume, energy and solid angle interval, imparted per unit time by an external source or by photons interacting with the medium at time  $t$ . This latter part of the source term causes the coupling of the electron and photon fluences”, (Kawrakow *et al* 2019).

The collision integral includes all possible interactions of electrons that lead to a change of the fluence, at a specific phase space coordinate:

$$I[\Phi] = -n(\vec{x})\Phi(\vec{x}, \vec{\Omega}, E, t) \int_0^E dE' \int_{4\pi} d\vec{\Omega}' \sigma(E, E', \Omega', \vec{x}) \\ + n(\vec{x}) \int_E^\infty dE' \int_{4\pi} d\vec{\Omega}' \Phi(\vec{x}, \vec{\Omega}, E, t) \sigma(E', E' - E, \Omega' \cdot \Omega, \vec{x})$$

In this,  $n$  is the atom or molecule density and  $\sigma$  the total cross section of all possible interactions that can change the fluence at a specific point in phase space.

A transport equation like this can be written as a Fredholm equation of the second kind. The solution to a Fredholm equation of the second type can be calculated by generation of a specific Markov chain. This is described in detail in the literature (Vassiliev 2017). The algorithm for solving a transport equation for radiation transport becomes very intuitive if the actual physical process is implemented as Markov process. This results in an algorithm as follows:

- Sample an initial electron from the source.
- Dice a random electron track based on the underlying cross sections.
- Calculate the observable (e.g. the deposited dose) based on the track (tallying).
- Repeat this for many particles and take the mean value.

In general, it is also possible to choose different Markov processes, what is called biasing (Vassiliev 2017). Modern MC algorithms include many different options for biasing. This is done to reduce the variance for a certain computation time (variance reduction techniques).

### Condensed History Algorithms

If single-scattering cross sections are used for the modeling of the electron interactions, the resulting algorithm can be demanding on computation time. Therefore, modern MC codes utilize condensed history (CH) algorithms for the electron transport. The CH approach is presented in an early publication by Berger (Berger 1963). For this, many steps of the actual physical random walk are condensed into a single step of a “condensed” random walk. CH algorithms can be classified in two schemes. A Class I CH algorithm “relies entirely on the grouping of collisions and involves the use of a predetermined set of pathlengths. Class II is based on a mixed procedure in which collisions with small energy losses and deflections are subject to grouping, but occasional “catastrophic” collisions, in which the loss or deflection are very large, are treated separately by conventional random sampling according to the single-scattering cross sections.”, (Berger 1963). Both approaches are based on multi scattering theories, like the distribution of Moliere (Moliere 1948) or the theory of Goudsmit and Saunderson (Goudsmit and Saunderson 1940).

## Cross Sections

ICRU Report 90 (Seltzer *et al* 2014) gives a comprehensive description of all physical processes and the corresponding cross sections that are needed for the calculation of the deposited dose to several media by MC simulations. This includes a description of the photoelectric effect, coherent (Rayleigh) scattering, incoherent (Compton) scattering and pair production, for photon interactions. The online database XCOM (Berger and Hubbell 1987) has become a standard source for cross sections for photon interactions. All simulations presented in this work are based on the XCOM database and followed the recommendations of ICRU Report 90 (Seltzer *et al* 2014). A comprehensive “review of the history of photon cross section calculations” can be found in the literature (Hubbell 2006).

For electrons, the National Institute of Standards and Technologies (NIST, Gaithersburg, USA) provides the ESTAR database (Berger *et al* 1998). This database includes values of the mass stopping power for many materials.

In the following, the relevant photon and electron interactions are described briefly. In addition, the original publications, that form the basis of the XCOM and ESTAR database are described and the most important recommendations of ICRU Report 90 (Seltzer *et al* 2014) are set into context.

## Photon Cross Sections

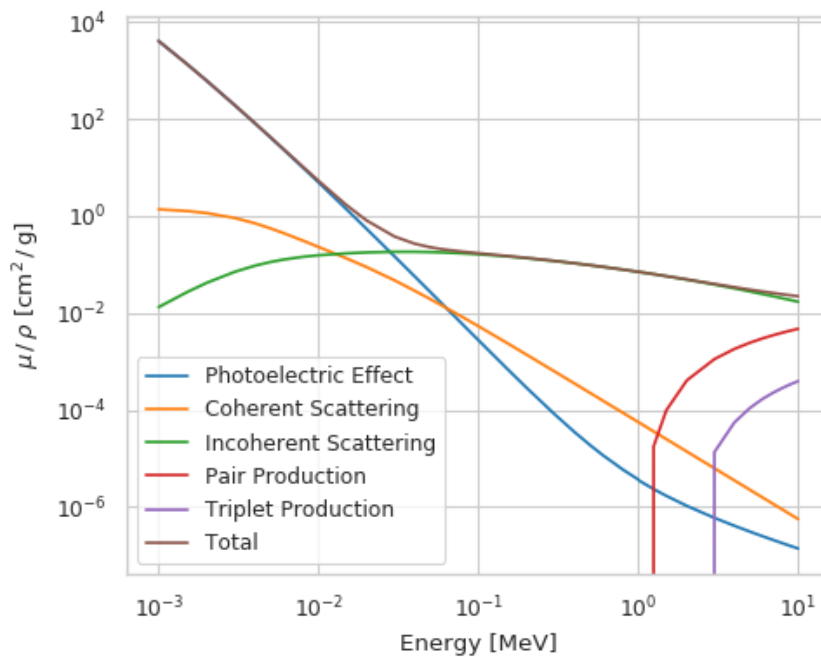


Figure 7: Mass attenuation coefficients for photon interactions in water. Data taken from (Berger and Hubbell 1987).

### *Photoelectric Effect*

The photoelectric effect describes the absorption of a photon by an electron that is bound to an atom. After the absorption of the photon, the electron is ejected from the atom. The energy of the emitted electron is determined by the difference of the energy of the incoming photon and the binding energy of the electron. As the electron is lost for the corresponding shell, this leads to the emission of fluorescence photons and Auger electrons. In the energy range of radiation oncology, the most relevant interactions are with electrons of the K-shell, where the electrons are bound most tightly (Hubbell 2006).

A theoretical description for the determination of the corresponding cross sections up to 1.5 MeV is given in the literature (Scofield 1973). This publication is the basis of the cross sections listed in the XCOM database (figure 7). The calculations presented by Scofield (Scofield 1973) are based on the Dirac equation for relativistically moving electrons in a Hartree-Slater central potential. As the Hartree-Slater potential includes some simplifications for the electron-electron interactions, Scofield (Scofield 1973) also provided renormalization factors to convert the results for  $Z = 2$  to 54 “to values expected from a relativistic Dirac-Hartree-Fock computation” (Hubbell 2006). The



influence of this renormalization is discussed in detail in ICRU Report 90 (Seltzer *et al* 2014). The reason for this is, that some experimental results agree better with theory, if no normalization is applied. But in ICRU Report 90 (Seltzer *et al* 2014), no clear recommendation is given, if the renormalization should be applied or not. However, the effect of the renormalization on typical MC simulations for radiation oncology is small (Czarnecki *et al* 2018).

As seen in figure 7, the photoelectric effect is dominant for energies in the keV range. The dependence of the cross section of the photoelectric effect ( $\sigma_{\text{ph}}$ ) on the atomic number  $Z$  can be approximated as (Demtröder 2017):

$$\sigma_{\text{ph}} \sim Z^5$$

Therefore, the absorption of photons is highly dependent on  $Z$ , for low energies. The angular distribution of the photoelectron can be calculated with help of the Sauter's distribution (Kawrakow *et al* 2019):

$$f(x)dx = \frac{1 - x^2}{(1 - \beta x)^4} (1 + k(1 - \beta x))dx$$

$$k = \frac{\gamma}{2}(\gamma - 1)(\gamma - 2), \quad \gamma = \frac{1}{\sqrt{1 - \beta^2}}$$

In this,  $\beta$  is the velocity of the electron weighted by the speed of light and  $x = \cos(\theta)$  is the polar angle. In figure 8, the angular dependence of this distribution is shown for different energies. For low energies, the photoelectrons are directed perpendicular to the direction of the incident photon. For higher energies, the photoelectrons are more likely to be directed in the same direction as the incident electron. A detailed description of an efficient implementation of the Sauter's distribution into a MC algorithm can be found in the literature (Bielajew and Rogers 1986).

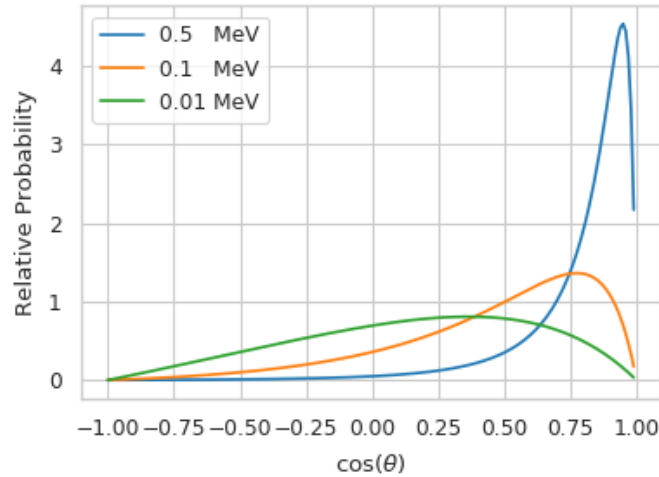


Figure 8: Sauter's photoelectron angular distribution for different energies.  $\theta$  is the angle between the direction of the incident photon and the direction of the photoelectron.

### *Coherent (Rayleigh, Elastic) Scattering*

“Rayleigh scattering is the elastic scattering of photons without electronic excitation of the target atom”, (Seltzer *et al* 2014). One approach for the calculation of cross sections for this effect is integrating the product of the Thomson formula (that quantifies the interaction of a photon with a free electron) and the relativistic Hartree-Fock atomic form factor ( $F(q, Z)$ ).  $F(q, Z)$  was tabulated in the literature (Hubbell *et al* 1975). Based on this, the differential cross section can be expressed as described by Kawrakow *et al* (Kawrakow *et al* 2019):

$$\frac{d\sigma_{cs}}{dx} = \pi r_e^2 (1 + x^2) [F(q, Z)]^2$$

Here,  $r_e$  is the classical electron radius and  $q$  is the momentum transfer. The same approach was chosen for the XCOM database (figure 7).

Like the photoelectric effect, coherent scattering incidents have a high probability at low energies but become less prominent in the MeV range (figure 7). The dependence of the cross section for incoherent scattering on the atomic number  $Z$  can be roughly approximated as (Demtröder 2017):

$$\sigma_{cs} \sim Z^2$$

### *Incoherent (Compton) Scattering*

In Compton scattering, “an incident photon [...] is absorbed, and a scattered photon is emitted with lower energy [...]. The energy difference between the incident and the

scattered photons is transferred to an atomic electron in a bound orbital”, (Seltzer *et al* 2014). The probably most known approach for the calculation of the cross-sections for incoherent scattering is the integration of the Klein-Nishina formula (Klein and Nishina 1929). Similar to the Thomson formula, the Klein-Nishina formula is based on the calculation of the interaction of a photon with a free electron at rest. Therefore, this approach neglects any electron-binding effects. To compensate for this, the cross section for incoherent scattering can be derived by combining the Klein-Nishina cross sections ( $\frac{d\sigma_{kn}}{dx}$ ) with the nonrelativistic Hartree-Fock incoherent scattering functions  $S(q, Z)$ , that can be found in the literature (Hubbell *et al* 1975):

$$\frac{d\sigma_{cs}}{dx} = \frac{d\sigma_{kn}}{dx} S(q, Z) = \pi r_e^2 P(\beta, x)^2 [P(\beta, x) + P(\beta, x)^{-1} + x^2 - 1] S(q, Z)$$

In this,  $P(\beta, x)$  is the ratio of the photon energy before and after the interaction. This approach has been chosen for the XCOM database. In case of  $P(\beta, x) = 1$ , the Klein-Nishina formula reduces to the Thomson formula. Figure 9 shows the angular dependence of the Klein-Nishina distribution.

Incoherent scattering is the most prominent interaction at the energy range of the primary photons coming from medical linacs (figure 7). The dependence of the cross section for incoherent scattering on the atomic number  $Z$  can be approximated as described in the literature (Demtröder 2017):

$$\sigma_{is} \sim Z$$

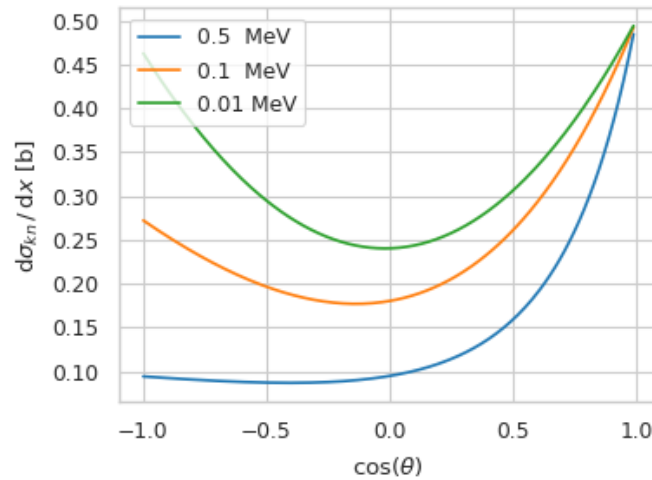


Figure 9: Differential Klein-Nishina cross sections.  $\theta$  is the angle between the direction of the incident photon and the direction of the photoelectron.

### Pair and Triplet Production

In this interaction, “a photon disappears in the field of a charged particle, and an electron-positron pair appears”, (Hubbell 2006). Pair and Triplet production can occur under the influence of the nuclear field (pair production) of an atom, as well as under the influence of the atom’s electron field (triplet production). Like for Rayleigh scattering, in pair production the whole atom recoils the electron-positron pair. Therefore, the interaction is coherent. In contrast, triplet production is incoherent and the “target electron recoil significantly affects the dynamics”, (Hubbell 2006). In triplet production, the atom is either excited or ionized. Hubbell et al. (Hubbell *et al* 1980) presented cross sections for both interactions that are based on the Bethe-Heitler formula (Bethe and Heitler 1934) modified by several corrections. The values presented by Hubbell et al. (Hubbell *et al* 1980) are included in the XCOM database.

Pair and Triplet production become an important interaction for energies  $> 10$  MeV. For most medical applications, energies above 10 MeV are not useful and avoided because of neutron production. The dependence of the cross sections ( $\sigma_{pp}$  and  $\sigma_{trp}$ ) on the atomic number  $Z$  can be approximated as (Hubbell 2006):

$$\sigma_{pp} \sim Z^2$$

$$\sigma_{trp} \sim Z$$

### Electron Cross Sections

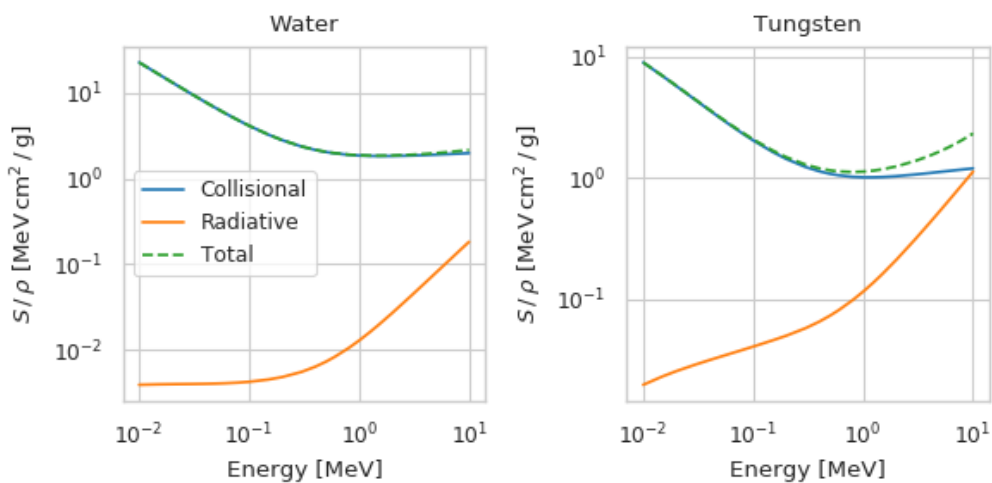


Figure 10: Mass stopping power for electron interactions in water (left) and tungsten (right). Data taken from (Berger *et al* 1998).

### *Radiative Losses (Bremsstrahlung)*

Bremsstrahlung (braking radiation) photons are produced if a charged particle is accelerated by interaction with an electromagnetic field. This could be caused by interaction with the electromagnetic field of a bound electron of an atom, or with the electromagnetic field of an atomic nucleus.

A summary of bremsstrahlung cross-section formulas can be found in the literature (Koch and Motz 1959). Koch and Motz (Koch and Motz 1959) presented approaches based on perturbed free-particle wavefunctions (Born approximation theory). The cross-section formulas by Koch and Motz (Koch and Motz 1959) are also used in multiple MC codes to sample the angular distribution of the Bremsstrahlung photons, as it is described in detail in the literature (Bielajew *et al* 1989). This results in an angular distribution that is peaked into the initial direction of the accelerated electron (Bielajew *et al* 1989). The cross-sections that set the basis of the ESTAR database were described by Seltzer and Berger (Seltzer and Berger 1986, 1985).

The influence of Bremsstrahlung-effects for different energies can be seen in figure 10. For small energies, the proportion of the radiative mass stopping power in the total mass stopping power is low, but this changes for higher energies. For water, Bremsstrahlung is the most important effect for energies above 100 MeV (Berger *et al* 1998). For high-Z materials (like Tungsten) Bremsstrahlung is already dominant at around 10 MeV (figure 10).

### *Collisional Losses*

Electrons can interact with atomic electrons (inelastic collisions). If the binding of the atoms electrons is ignored, these discrete interactions can be described by the cross sections derived by Møller (Møller 1932). A similar approach can be chosen for positrons, using the results presented by Bhaba (Bhaba 1936). The mass electronic (or collision) stopping power can be calculated based on the analytical approach presented by Bethe (Bethe 1932, 1930), what is also the basis of the data tabulated in the ESTAR database and in the work of Berger and Seltzer (Berger and Seltzer 1964). An important note is, that the mass electronic (or collision) stopping power depends on the mean excitation energy  $I$ .  $I$  cannot be calculated accurately from first principles and must be derived from experimental data (Berger *et al* 1998).

An important correction to these cross-sections is the density-effect correction. “When a charged particle moves through a medium, the polarization of atoms in medium decreases the field acting on the particle, so as to reduce the stopping power. This reduction is large in a condensed medium compared with that of a gas with the same composition, and thus is called the density effect”, (Seltzer *et al* 2014). An analytical description of this effect can be found in the literature (Fermi 1940, Sternheimer 1966, 1967). One key finding mentioned by Seltzer *et al.* (Seltzer *et al* 2014) is, that the density effect of graphite (what is a material commonly used for the construction of ionization chambers) must be calculated based on the crystalline density of graphite, instead of “the density of the grains that form the bulk material”. Similar effects must be taken into account for the calculation of the density effect of alanine pellets, where also the crystalline density must be used (Seltzer *et al* 2014).

But electrons can also be scattered at atoms (elastic collision). This can be described as an interaction of the electron with the screened nucleus of the atom. The effect can be quantified based on cross sections derived in the literature (Wentzel 1926). More advanced formulations of cross sections for this effect can be found in a review by Motz *et al.* (Motz *et al* 1964). Tabulated values for the corresponding mass nuclear stopping power can be found in the work of Seltzer and Berger (Seltzer and Berger 1985), what is the basis of the ESTAR database.

As seen in figure 10 the mass electronic (or collision) stopping power contributes most to the energy deposition in water, for the typical energy range of linacs. “The nuclear stopping power is negligible for electrons”, (Seltzer *et al* 2014).

## Magnetic Resonance Imaging Guided Radiotherapy

### Workflow of External Beam Radiotherapy

In EBRT, the dose deposition that is expected inside of a patient is calculated beforehand. The calculations are based on an electron density map acquired by a computed tomography scan (CT scan). For this, the CT scan is imported into a treatment planning system (TPS). The TPS includes a detailed model of the linac and an algorithm for the calculation of the expected dose distribution inside of the patient, based on the given CT scan. Several parameters, like the gantry position and the collimation of the beam can be varied in the TPS. Based on these parameters, the expected dose distribution inside of the patient can be optimized. For more advanced techniques, like the intensity-modulated radiotherapy (IMRT), the TPS includes an optimization algorithm to help the user to find an optimal set of parameters. The optimal set of parameters is saved within the radiation treatment plan (RTP).

Usually, the treatment is fractionated into multiple treatment appointments. As an example, an conventional treatment for localized prostate cancer consists of 74 Gy in 37 fractions over 4 weeks (Dearnaley *et al* 2016). For each treatment appointment, the patient must be positioned on the treatment couch of the linac. In most scenarios, the RTP is not adapted in-between the treatment appointments. This can be problematic, because the position of the tumor can change between the different radiation fractions (Rietzel *et al* 2004, Hector *et al* 2001, Booth and Zavgorodni 1999, Ashamalla *et al* 2005). In addition, the size of the tumor can change during the course of therapy due to treatment response or tumor progression.

### Image-guided Radiotherapy

In image-guided radiotherapy (IGRT), in-room imaging is used to improve the positioning of patients during EBRT. In recent years, different methods became available for this purpose, e.g. the detection of the transmitted treatment beam or imaging with a CT scanner that is integrated into to the linac (Kamino *et al* 2006, Jaffray 2007, Onishi *et al* 2003, Pouliot *et al* 2005, Berbeco *et al* 2004). These methods can be used for optimizing the patient's positioning, based on the location of bones or markers.

In many aspects, IGRT can be improved by the implementation of methods that are based on magnetic resonance imaging (MRI). This is, because MRI has many advantages compared to the conventional techniques used in IGRT, that are so far mostly based on cone-beam CT (CBCT). The main limitation of CBCT-IGRT is motion blurring:

“a poor image quality in regions of the body with much internal motion due to respiration and gas, causing blurring of soft tissue interfaces” (Grégoire *et al* 2020). MRI provides a better soft tissue contrast in these regions and therefore enables an improved online monitoring of the tumor position. In addition, the good soft tissue contrast of MRI improves the delineation of the tumor volume in general. The delineation of the tumor volume was found to be the “weakest link in the search for accuracy in radiation therapy”, (Njeh *et al* 2013).

Also, MRI can be used for accessing various functional information, e.g. about perfusion or diffusion inside of a tumor. This information is linked to the tumor’s microscopic architecture. Consequently, measuring functional information may have the potential to enable the adaption of the treatment in-between the fractions but also to monitor the treatment efficacy and success (Thorwarth 2015, Troost *et al* 2015, Grégoire *et al* 2020, Thorwarth *et al* 2020). Therefore, some authors have concluded, that the “future of image-guided radiotherapy will be MR guided”, (Pollard *et al* 2017).

In addition, different groups are in the process of developing methods for real-time MR reconstruction, e.g. based on convolutional neural networks (Dietz *et al* 2019), as well as for real-time dose calculation (Voss *et al* 2019). In the future, such techniques might enable real-time adaption of the treatment plan during the irradiation.

Efforts to develop systems for MRlgRT were intensified during the last 20 years. Today, two commercial systems are clinically available for the treatment of patients. The content of this work is focused on perpendicular MR-linac systems (figure 11, left).

### MR-linacs

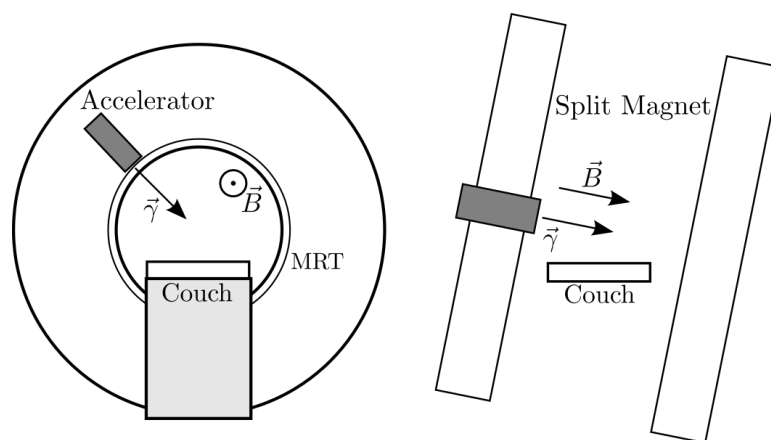


Figure 11: Schematic representation of two designs for MR-linacs. Perpendicular system (left) and inline system (right). For perpendicular systems the treatment beam is always perpendicular to the magnetic field vector.



## Perpendicular Systems

### The 7 MV FFF 1.5 T MR-linac

In 2004, a group based at the University Medical Center Utrecht (UMC Utrecht, Netherlands, Utrecht) presented a design for a device, that combines a clinical 6 MV linac with a 1.5 T magnetic resonance tomograph (MRI), an MR-linac (Raaymakers *et al* 2004). Five years later, the same group presented a prototype of the described device as a proof of concept (Raaymakers *et al* 2009). Finally, in 2017 the group reported the first treatment of a patient with a 1.5 T MR-linac, which took place in May 2017 (Raaymakers *et al* 2017). The final design of the device (Unity, Elekta AB, Stockholm, Sweden) utilizes a 7 MV FFF standing wave accelerator that is mounted on a ring-based gantry. The gantry rotates around a closed-bore MRI (bore size 70 cm, figure 11, left). Though there is a gap of 15 cm in the superconducting coils of the MRI for beam passage, the beam passes through various other parts of the MRI cryostat (Friedel *et al* 2019). This leads to attenuation and scattering effects (Raaymakers *et al* 2004). The accelerator is actively shielded against the fringe field of the MRI. This is realized with the help of shield coils that generate a field of opposite polarity (Raaymakers *et al* 2009). The SID of the system is 143.5 cm. The field size can be varied between  $0.5 \times 0.5 \text{ cm}^2$  and  $57 \times 22 \text{ cm}^2$ . The leaf size at the isocenter is approximately 0.72 cm. In a system like this, the beam is always perpendicular to the direction of the magnetic field vector. Different results have been published for the beam quality specifier  $TPR_{20,10}$ , these are presented in table 1. The pulse repetition frequency of the linac lies at 275 Hz, what results in “an water absorbed-dose-per-pulse of approximately 0.34 mGy/pulse”, (de Prez *et al* 2019), in reference conditions.

Author	$TPR_{20,10}$	Method	Beam Model
O'Brien <i>et al.</i> , 2016	0.695(?)	Monte Carlo	(O'Brien <i>et al</i> 2016)
Malkov and Rogers, 2018	0.691(1)	Monte Carlo	(Ahmad <i>et al</i> 2016)
de Prez <i>et al.</i> , 2019	0.701(2)	Experiment	-
Snyder <i>et al.</i> , 2020	0.704(?)	Experiment	-
Pojtinger <i>et al.</i> , 2020b	0.7028(14)	Monte Carlo	(Friedel <i>et al</i> 2019)

Table 1:  $TPR_{20,10}$  for the 7 MV FFF 1.5 T MR-linac reported by different authors.

### The 6 MV FFF 0.35 T MR-linac

In the meantime, another proposal for a system in which the beam is perpendicular to the magnetic field was presented by Kron *et al.* (Kron *et al* 2006). Kron *et al.* (Kron *et al* 2006) speculated, that “a linear accelerator to produce radiation may be

incompatible with the pulsed radiofrequency and the high and pulsed magnetic fields required for MRI". Therefore, the authors suggest a system that combines an open 0.25 T MRI with two Cobalt-60 sources. In the commercial adaption of the system, three Cobalt-60 sources are used, to compensate for the low dose rate of Cobalt-60 (Mutic and Dempsey 2014). Also, the final design utilizes a 0.35 T MRI (70 cm bore) instead of a 0.25 T MRI. In this setup, the MRI is split, to allow the treatment beam to pass. The first patient was treated in January 2014 (Olsen *et al* 2015). Later, the design of this system was changed by replacing the three Cobalt-60 sources with a 6 MV FFF standing wave accelerator. Also, the SID was changed from 105 cm to 90 cm. In addition, the maximum field size was changed from  $27.3 \times 27.3 \text{ cm}^2$  to  $24.1 \times 27.4 \text{ cm}^2$ . The minimum field size is  $0.2 \times 0.415 \text{ cm}^2$  and can be varied in steps of 0.415 cm. A detailed description of the modifications can be found in the literature (Klüter 2019). The first treatment of a patient with the modified system (MRIdian, ViewRay, Oakwood, USA) took place in July 2017 (Liney *et al* 2018b). For the beam quality specifier, Krauss *et al.* (Krauss *et al* 2020) reported  $TPR_{20,10} = 0.648$ .

### *Inline Systems*

A different MR-linac design was proposed by Fallone *et al.* (Fallone *et al* 2009). The idea of this design is to use a linac that is fixed to a split magnet. For different beam angles, the linac and the magnet rotate together around the axis of the treatment couch (figure 11, right). First experiments were done by combining a 6 MV linac with a 0.2 T MRI. The magnetic field of the MRI was generated by a permanent magnet (Fallone *et al* 2009). Later, the 0.2 T MRI was replaced by a 0.6 T MRI (Fallone 2014). In the new setup, the magnetic field is generated by an electromagnet that must be cooled. The cooling of the upgraded magnet is realized by a cryocooler. Therefore, no cryogenic liquids are needed. This system allows beam directions that are in line with the direction of the magnetic field vector.

A similar system was described by Keall *et al.* (Keall *et al* 2014). This system was developed as part of the Australian Magnetic Resonance Imaging-linac program. In the design described by Liney *et al.* (Liney *et al* 2018a), the system consists of a movable linear accelerator that can be used in 4 or 6 MV mode. The accelerator is placed in front of a 1 T split magnet. The gap between the coils is 50 cm. Several different ideas for the treatment from different beam angles were discussed by Keall *et al.* (Keall *et al* 2014), including the rotation of the patient. A prototype of a MRI compatible patient

rotation system is described in the literature (Whelan *et al* 2017). An upgraded prototype of the system was presented by Liney *et al.* (Liney *et al* 2016). In contrast to the previous prototype, the upgraded system combines the same mobile linear accelerator with a commercial 1.5 T MRI (60 cm bore).

At this point, no inline system has been used for the treatment of patients and the systems are in an early, non-commercial state.

### Consequences for the Absorbed Dose

If a water phantom is irradiated inside of a MR-linac, the magnetic field influences the spatial distribution of the absorbed dose to water (Raaymakers *et al* 2004, O'Brien *et al* 2016, Richter *et al* 2017). As described before, the most common interaction of the primary photons (generated by a linac) with water is by incoherent scattering. The trajectories of the emerging secondary electrons determine the spatial distribution of the absorbed dose to water. But, as electrons are charged particles, they are influenced by Lorentz force. Consequently, the magnetic field of an MR scanner shifts the distribution of the dose to water. The direction of this dose shift can be approximated by the direction of the Lorentz force:

$$\vec{F} = q (\vec{v} \times \vec{B})$$

In a perpendicular MR-linac system, the initial direction of the secondary electrons, and consequently the velocity vector  $\vec{v}$  are approximately perpendicular to  $\vec{B}$ . Therefore,  $\vec{F}$  is also perpendicular to  $\vec{v}$ . As the trajectories of the secondary electrons are shifted in direction of the Lorentz force, the electrons are bend in a direction perpendicular to the beam direction. Because of this, the secondary electrons travel a shorter distance in the beam direction and the depth dose curve is shifted (figure 12, left). This also changes the lateral spread of the dose distribution (figure 13). The change of the dose to water caused by the magnetic field ( $c_{\vec{B}}$ ) is an important quantity for absolute dosimetry in MR-linacs (van Asselen *et al* 2018).  $c_{\vec{B}}$  is expressed as the ratio of the dose to water under the influence of the magnetic field ( $D_{w,Q_{\vec{B}}}$ ) to the dose to water without the influence of the magnetic field ( $D_{w,Q}$ ):

$$c_{\vec{B}} = \frac{D_{w,Q_{\vec{B}}}}{D_{w,Q}}$$

Several authors reported MC simulated values for this quantity that were calculated for a  $10 \times 10 \text{ cm}^2$  photon field (table 2). For a  $10 \times 10 \text{ cm}^2$  photon field, the effect is independent of the depth in water, starting from a depth of about 3 mm (O'Brien *et al* 2017). Currently, no experimental results are available for  $c_{\bar{B}}$ . The main reason for this is, that for the direct measurement of  $c_{\bar{B}}$  one would need a detector with a response that must not be influenced by magnetic fields.

Not only the distribution of the dose to water is changed by the magnetic field, but also the dose distribution inside of a patient. Therefore, the algorithm implemented in the TPS (that is used to simulate the dose distribution inside of a patient for clinical radiotherapy) must be capable of simulating the dose distribution in the patient under the influence of a magnetic field (Ahmad *et al* 2016).

Some authors speculated, that the influence of a magnetic field on the dose deposition can be beneficial for the treatment of small, isolated lung tumors (Oborn *et al* 2015).

Author	Beam Quality	Magnetic Flux Density [T]	$c_{\bar{B}}$
O'Brien et al., 2016	7 MV	1.5	0.995(1)
Billas et al., 2020	8 MV	1.5	0.9958(4)
van Asselen et al., 2018	7 MV	1.5	0.9949(3)
Malkov and Rogers, 2018	7 MV	1.5	0.9914(2)
Pojtinger et al., 2020a	7 MV	1.5	0.9936(20)
Billas et al., 2020	6 MV	1.5	0.9969(4)
Delfs <i>et al.</i> , 2018	6 MV	1.42	0.9925(?)
van Asselen et al., 2018	7 MV	0.35	0.9991(3)
Billas et al., 2020	6 MV	0.35	0.9997(4)
Delfs et al., 2018	6 MV	0.35	0.9953(?)

Table 2: MC simulated values of  $c_{\bar{B}}$  for different beam qualities and magnetic flux densities.

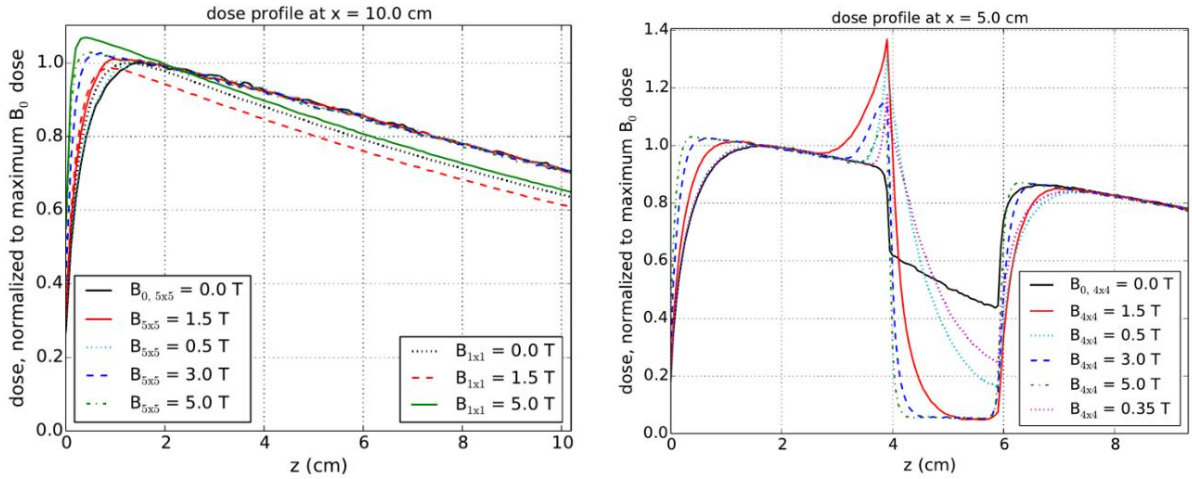


Figure 12: Results of MC simulations of depth dose curves (in water) of a 6 MV linac under the influence of an external magnetic field. The magnetic field vector is perpendicular to the beam direction. The indices of  $B$  represent the corresponding collimation of the photon beam. In the right part of the figure, an air gap was introduced into the water phantom between  $z = 4$  and  $z = 6$ . The figure was taken from (Richter et al., 2017, licensed under CC BY-NC-ND 4.0 ).

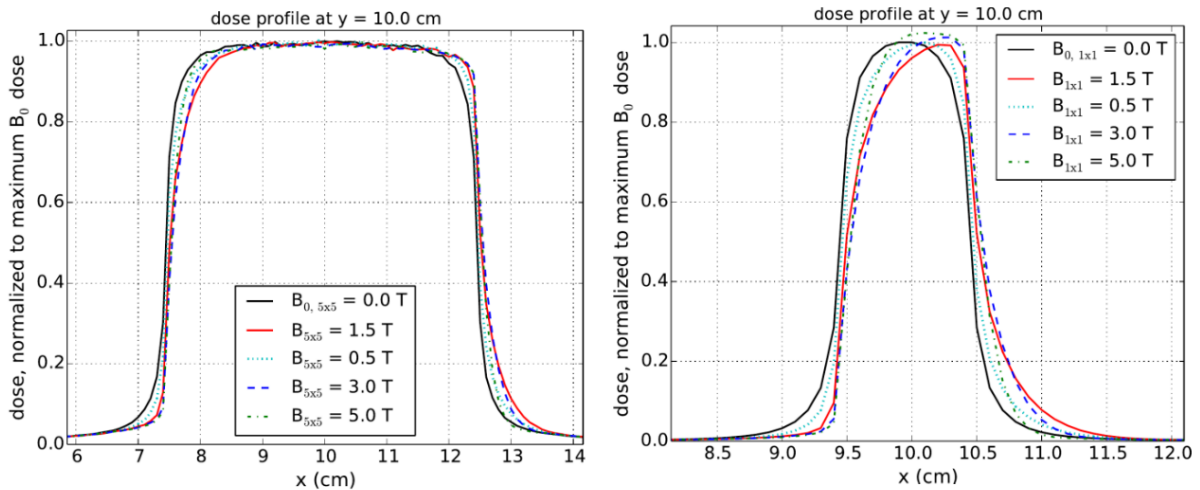


Figure 13: Results of MC simulations of beam profiles (in water) of a 6 MV linac under the influence of an external magnetic field. The magnetic field vector is perpendicular to the beam direction. The indices of  $B$  represent the corresponding collimation of the photon beam. The figure was taken from (Richter et al., 2017, licensed under CC BY-NC-ND 4.0).

### Influence of Air Cavities

One specific problem in this scenario are air cavities. If secondary electrons transit from a dense material like water into an air cavity, the mean free path length increases and the energy lost per distance decreases, as there are less interactions per path length (figure 14, right).

For illustration, the path of an electron in air, can be approximated by the relativistic gyroradius  $r_g$  in vacuum:

$$r_g = \gamma \frac{m_e v}{B e}$$

In this,  $m_e$  is the rest mass of the electron,  $e$  the elementary charge and  $\gamma$  the Lorentz factor. The speed of the electron can be expressed by the Lorentz factor as:

$$v = c \sqrt{1 - 1/\gamma^2}$$

The resulting radii for a typical energy range are shown in (figure 15, left). Considering a typical energetic spectrum of the secondary electrons (figure 15, mid), the expectation value of  $r_g$  lies around  $\langle r_g \rangle \approx 2$  mm, for a magnetic flux density of  $B = 1.5$  T (figure 15, right). This value can be smaller for an individual electron. Assuming secondary electrons move from a dense material like water into a less dense material like air, the trajectories of the secondary electrons become similar to the trajectories expected in vacuum, that are described by a helical movement around the magnetic field vector, with radius  $r_g$ . If the air cavity is big enough, the electrons can take a full turn inside of the air volume and return to the dense medium. This causes an increase of dose at the surface area (figure 12, right). This effect is called the electron return effect (ERE) and was first described in the work of Raaijmakers et al. (Raaijmakers *et al* 2005).

A common experimental practice in clinics is to replace the water phantom by water-equivalent plastic slabs. These slabs include an air cavity in which the detector can be positioned. The reason for this practice is, that it takes less time and effort to set up plastic slabs instead of a water phantom. But in the described scenario, this can be problematic because of the eventuality of the occurrence of the ERE, if there are air gaps between the detector and the plastic material (Hackett *et al* 2016, O'Brien and Sawakuchi 2017). Asymmetric air gaps of only 0.2 mm have been shown to effect ionization chamber measurements by 1.6% (O'Brien and Sawakuchi 2017).

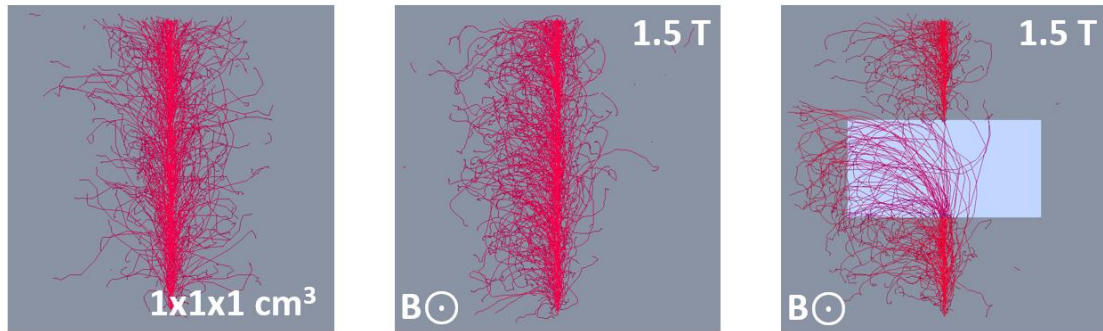


Figure 14: MC simulation snapshots of secondary electron trajectories that are emerging from a 1.2 MeV photon pencil beam. By bringing in a magnetic field, the electron trajectories are changed, as electrons are charged particles, that are influenced by Lorentz force (middle). If a second medium like air is involved, where the mean free path length of electrons differs a lot from these of the surrounding medium, the deflection increases (right).

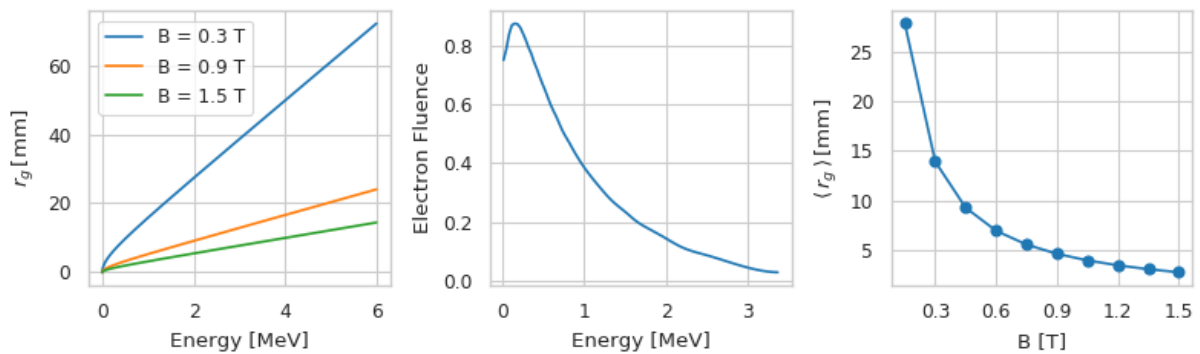


Figure 15: Relativistic gyroradius for different magnetic flux densities (left), an MC-calculated electron spectrum scored inside the sensitive volume of an ionization chamber positioned in a water phantom (middle) and the corresponding expectation values for the gyroradius (right). The electron spectrum (middle) was created by a spline interpolation of the data provided in (Benmakhlouf and Andreo 2017).

## Effects on Monte Carlo Simulations

### *Implementation of the Magnetic Field*

Malkov and Rogers (Malkov and Rogers 2016) described a method to implement the effects of static magnetic fields into a CH electron transport algorithm, as it is implemented in EGSnrc. In a CH algorithm, typically a certain step length is calculated first. Then, the algorithm decides on a random position (the position of the multiple scattering interaction) on the resulting path. An algorithm like this intrinsically includes three position and velocity vectors (figure 16), as the velocity of the particle must be known at the point of interaction. Malkov and Rogers (Malkov and Rogers 2016) found, that this can be used for an algorithm that includes the Lorentz force into the simulation by a three-point integration, that uses the velocities that are calculated by the CH

algorithm. Based on this, Malkov and Rogers (Malkov and Rogers 2016) derived, that the change of the direction vector ( $\vec{u}$ ) due to the magnetic field can be expressed as:

$$\Delta\vec{u} = \frac{qt c^2}{6v_0 E_0} (\vec{v}_0 + 4\vec{v}_{rp} + \vec{v}_t) \times \vec{B}$$

Here,  $q$  is the particle charge,  $t$  the time interval of the CH step,  $c$  is the speed of light,  $v$  is the particle velocity and  $E_0$  the initial energy of the particle. The time interval  $t$  can be approximated by the velocity before ( $v_0$ ) and after ( $v_f$ ) the CH step, and the original step length  $s$ :

$$t \cong \frac{s}{v_0} \left( \frac{1}{2} + \frac{v_0}{2v_f} \right)$$

Finally, the change of position due to Lorentz force can be expressed as:

$$\Delta\vec{x} = \frac{s}{2} \left( \frac{1}{2} + \frac{v_0}{2v_f} \right) \Delta\vec{u}$$

In the final algorithm presented by Malkov and Rogers (Malkov and Rogers 2016), the position of the charged particle is updated by  $\Delta\vec{x}$ , after each CH step.

Algorithms like this have been implemented to several MC codes for the simulation of coupled electron-photon transport and have been described in detail in (Bielajew 1988). In dosimetry for medical applications, the most frequently used MC codes are: EGSnrc (Kawrakow *et al* 2019), Geant4 (Agostinelli *et al* 2003) and Penelope (Salvat *et al* 2009).

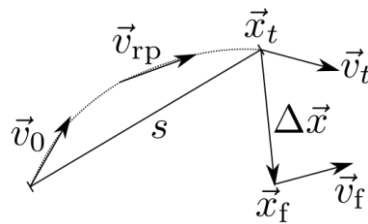


Figure 16: Representation of a CH step as it is implemented in EGSnrc. The arrows represent the velocity vectors at the positions  $\vec{x}_i$ . The velocity at the randomly drawn point is used to calculate a shift of position  $\Delta\vec{x}$  by a three-point integration, that accounts for the influence of the Lorentz force.

### Fano Cavity Test

The Fano cavity test is a method to benchmark MC simulations of transport equations. The method is based on the Fano theorem: "In a medium of given composition exposed to a uniform flux of primary radiation (such as X-rays or neutrons) the flux of secondary



radiation is also uniform and independent of the density of the medium as well as of the density variations from point to point”, (Fano 1954). This theorem can be derived analytically from the BTE (Fano 1954). Smyth (Smyth 1986) presented the first benchmark of an MC algorithm, based on the Fano theorem.

In general, the effect of the magnetic field can be included into the BTE, this is described in the literature (Bouchard and Bielajew 2015). In two important publications (de Pooter *et al*/2015, Bouchard *et al*/2015), the authors derived, that the Fano theorem does not hold for the BTE, if the BTE is modified to account for the magnetic field effects. Anyway, additional conditions can be introduced for the primary radiation to overcome this issue. A sufficient condition is, that the source is isotropic (de Pooter *et al*/2015).

One method to utilize the Fano cavity test for the benchmark of MC simulations of ionization chambers in magnetic fields is presented in the literature (Malkov and Rogers 2016). For this, all cross sections in the simulation geometry are changed to the cross sections of one specific material, e.g. water or graphite. A uniform per unit mass electron source is used to sample electrons all over the simulation geometry. In case of the creation of a photon by an electron, the photon is discarded immediately, and the corresponding energy is deposited at current position. In this scenario, the deposited dose  $D$  in a sensitive volume can be calculated as a product of the total number of simulated electrons per unit mass  $I$  and the initial energy of the electrons  $E_0$ . This leads to the Fano condition:

$$\frac{D}{IE_0} = 1$$

Following the Fano theorem, this equation is true, even if the density in some parts of the simulation geometry is changed. A typical approach for the application of the Fano test is to change the density of the sensitive volume of an ionization chamber by a factor of 1000. The exact volume of the sensitive volume must be known for the calculation of  $I$ .

If no magnetic field is included, modern MC algorithms fulfill this condition with deviations of less than 0.2% (Kawrakow 2000, Sempau and Andreo 2006, Sterpin *et al*/2014, Yi *et al* 2006). Several authors have adapted this or similar tests to benchmark the implementation of the magnetic field to the MC algorithm and the geometrical models

of the ionization chambers under investigation (Malkov and Rogers 2016, Spindeldreier *et al* 2017, Pojtinger *et al* 2018, Simiele and DeWerd 2018, O'Brien *et al* 2016, de Pooter *et al* 2015).

## Objectives

For conventional linacs, measurements of the absorbed dose to water are mandatory and must be traceable to primary standards for the absorbed dose to water. This also applies for MR-linacs. The procedures for an accurate measurement of the absorbed dose to water at conventional linacs are described in the protocols for reference dosimetry (TG-51 (Almond *et al* 1999), TRS-398 (Andreo *et al* 2006) and in Germany DIN 6800-2 (Deutsches Institut für Normung 2020)).

The overarching aim of this work was to set the foundation for extending and adapting existing protocols for reference dosimetry in radiation therapy to MR-linac environments. As the current protocols exclusively describe ionization chamber measurements, the influence of magnetic fields on the reading of ionization chambers was of particular interest.

Consequently, the main objective of this work was to systematically investigate and quantify the effects of magnetic fields on the response of ionization chambers. Three different approaches were identified for this purpose.

The first approach was to quantify the effects of magnetic fields on the response of ionization chambers in an experimental setup, that combines a big electromagnet with a conventional linac. In contrast to the situation in MR-linacs, the magnetic flux density can be changed easily when generating the magnetic field using an electromagnet. Consequently, this setup is a valuable tool for the investigation of magnetic field effects on any kind of radiation detector and to benchmark MC simulations.

Another approach investigated in this thesis was based on chemical radiation dosimetry. Chemical radiation detectors may be good candidates for the quantification of magnetic field effects on the response of ionization chambers by cross-calibration. In contrast to ionization chambers, the density of the chemical detector's sensitive is closer to water. This might be an advantage compared to ionization chambers, as air cavities can influence the secondary electron fluence.

The third approach was to use MC methods. In the past, MC simulations played an important role in the determination of correction factors for ionization chambers and simulations of ionization chambers have been benchmarked in many experiments. On the other hand, up to now there was no need to implement any magnetic field effects into the MC algorithms, for this kind of simulations. Therefore, an additional objective

of this work was to investigate if the current algorithms are suitable for the simulations of ionization chambers in magnetic fields.

## Results and Discussion

In the course of the investigations, the results of this work were published in several research papers (Pojtinger *et al* 2018, 2019, Trachsel *et al* 2020, Pojtinger *et al* 2020a, 2020b, de Pooter *et al* 2020). As the absolute dosimetry of photon radiation under the influence of magnetic fields is a new and rapidly developing topic, it is important to see the results in the context of the developments that took place in the recent years. The next chapters describe the publications linked to this work in the context of other important publications on the topic.

### Change of Response of Ionization Chambers

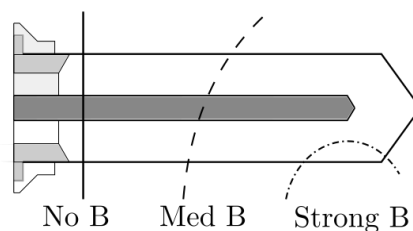


Figure 17: Illustration of secondary electron trajectories under the influence of a magnetic field. Without the influence of the magnetic field, the secondary electrons pass the sensitive volume approximately in a straight line (left), if the secondary electrons are influenced by Lorentz force, they describe a curved trajectory (middle). For high magnetic flux densities, the electrons can leave the sensitive volume right after entering the volume, what is similar to the ERE effect (right).

As the sensitive volume of the types of ionization chambers that are used for dosimetry in radiation oncology is filled with air, the effects described above have important consequences for the response of these types of radiation detectors. In a scenario without the influence of a magnetic field, most of the secondary electrons produced inside of a water phantom pass the air volume of the ionization chamber in a straight line. In contrast, under the influence of the magnetic field, the trajectories of the secondary electrons are bent. Consequently, the secondary electrons travel a longer or shorter distance inside of the sensitive volume (figure 17). Because of this, more (or less) ionizations occur. This can change the response of ionization chambers by several percent (Meijssing *et al* 2009). In fact, the problem is much more complex, as the secondary electron spectrum is not monoenergetic and therefore multiple trajectories are possible for each magnetic flux density. One way to approach this problem by theory is by MC simulations. In the first part of this work, the MC code system EGSnrc (Kawrakow *et al* 2019) was used to investigate the response of different ionization chamber geometries under the influence of magnetic fields. Multiple ionization chamber types have been

included into this study to decide on a geometry and ionization chamber orientation that is beneficial for the purpose of absolute dosimetry in MR-linacs. The results of this MC experiment were published in a research paper (Pojtinger *et al* 2018) and include an adapted Fano cavity test, to benchmark the implementation of the complex ionization chamber models as well as an benchmark experiment. For the benchmark experiment, the response of a Farmer type ionization chamber was measured in a setup that combines a clinical linac with a big electromagnet (figure 18).

It was found that the geometry of the ionization chamber plays an important role for the change of response caused by the magnetic field. At 1.5 T, the simulations of plane-parallel ionization chambers showed that the response of these type of detectors was altered by more than 1.5%, up to 7%. In addition, other authors showed that small angular misalignments of plane-parallel ionization chambers can change the influence of the magnetic field drastically (Malkov and Rogers 2018). In contrast, for thimble type ionization chambers there are orientations in which the response of the ionization chamber is influenced less than 1%.

On the other hand, changing the positioning of a thimble type ionization chamber (e.g. from a position in which the magnetic field vector is parallel to the ionization chamber axis to a position in which the ionization chamber axis is perpendicular to the magnetic field vector) changes the effects of the magnetic field. Therefore, thimble type ionization chambers are relatively stable against small angular misalignment, but the user must take care about the correct orientation of the ionization chamber axis relative to the direction of the magnetic field vector.

The peak of these effects lies at a magnetic flux density of roughly 1 T. In this sense, it is not necessarily an advantage to do measurements in a 0.35 T instead of a 1.5 T environment. This is because the effects are not linear and the influence of the magnetic field can vanish for magnetic flux densities above 1 T (figure 19).

Based on the results of this work, waterproof Farmer type ionization chambers seem to be the best choice for absolute dosimetry under the influence of magnetic fields, if they are used in an orientation in which the axis of the ionization chamber is parallel to the magnetic fields vector.

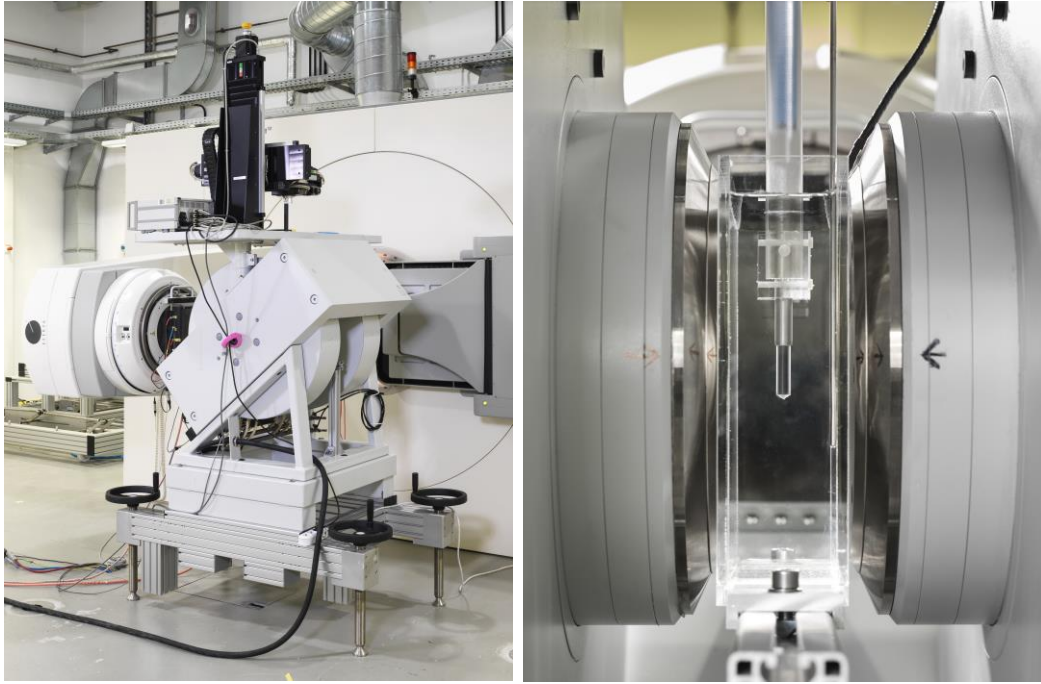


Figure 18: Experimental setup at PTB, for the investigation of magnetic field effects on radiation detectors. “A large electromagnet (Bruker ER073W) [...] was placed in front of an Elekta Precise accelerator (151605). A [...] water phantom (constructed by PTB) was positioned between the pole shoes of the magnet at a source-to-surface distance (SSD) of 110 cm. Ionization chambers were mounted within this phantom at a well-defined reference point and irradiated by a horizontal photon beam with a nominal accelerating voltage of 6 MV”, (Pojtinger *et al* 2019).

### Formalism

In early publications, the authors present the influence of magnetic fields on the response of ionization chambers in the form of relative response curves (Meijsing *et al* 2009, Smit *et al* 2013, Hackett *et al* 2016, Malkov and Rogers 2016). For this, the authors measured (or simulated) the signal of an ionization chamber for a specific magnetic flux density ( $M_{\vec{B}}$ ). Then, to obtain a relative response curve,  $M_{\vec{B}}$  was also measured or simulated for many other magnetic flux densities and the results were normalized to the situation without the influence of the magnetic field ( $M$ ). Many different names have been used for the inverse of the relative response ( $M/M_{\vec{B}}$ ), e.g.  $k_{\vec{B},M,Q}$  (table 3).

More recent publications suggest different formalisms to quantify the influence of the magnetic field on the response of ionization chambers (van Asselen *et al* 2018, O'Brien *et al* 2016). All of these formalisms have been developed following the typical approach in protocols for reference dosimetry, to quantify any change to the response of an ionization chambers (due to changes in measurement conditions) by a multiplicative correction factor.

In the work of O'Brien et al. (O'Brien *et al* 2018), the authors defined a magnetic field correction factor called  $k_B^{Q_{msr}}$ :

$$k_B^{Q_{msr}} = \frac{M}{M_{\bar{B}}} \frac{D_{w,Q_{\bar{B}}}}{D_{w,Q}} = k_{\bar{B},M,Q} c_{\bar{B}} = k_{\bar{B},Q}$$

The correction factor  $k_B^{Q_{msr}}$  complements  $k_{\bar{B},M,Q}$  by considering the change of the dose to water  $c_{\bar{B}}$ . This is explained in more detail below as well as in the literature (Pojtinger *et al* 2018).

$M$  is different from  $M_{\bar{B}}$  for of two reasons. The first reason is, that the magnetic field influences the response of the ionization chamber itself. But in addition, the dose distribution itself changes due the influence of the magnetic field, even if the ionization chamber is not present. In this sense, a measurement of  $M$  is a measurement of the undisturbed deposited dose to water, with an ionization chamber which is not influenced by a magnetic field. The measurement of  $M_{\bar{B}}$  is a measurement of the changed deposited dose to water, with an ionization chamber, that is influenced by a magnetic field. If a measurement that was taken under the influence of a magnetic field would be corrected with the ratio  $M/M_{\bar{B}}$  alone, one would correct for both of the mentioned effects. This would represent a calculation of the undisturbed deposited dose to water (the dose that would have been deposited if there would be no magnetic field). But as said before, in the actual measurement situation as well as in the treatment situation, the deposited dose to water differs from the undisturbed deposited dose to water.

Because the aim of the measurement is to measure the deposited dose to water, that is changed by the magnetic field, a correction with the ratio  $M/M_{\bar{B}}$  is not enough. Hence, the idea of O'Brien et al. (O'Brien *et al* 2018) was to use  $M/M_{\bar{B}}$  as a correction but to take the change of the deposited dose to water into account by multiplying  $c_{\bar{B}}$  as an additional factor (figure 19).

Later, different techniques were used for the experimental determination of the influence of the magnetic field, on the ionization chamber. The work of de Prez et al. (de Prez *et al* 2019) includes calorimetric measurements done inside of a MR-linac. Comparing these results with results of the same measurement using a Cobalt-60 source, allows the experimental determination of the product  $k_B^{Q_{msr}} k_Q$ . The authors called this



product  $k_{Q,B}$ . Table 3 shows a list of more quantities, that were used by different authors.

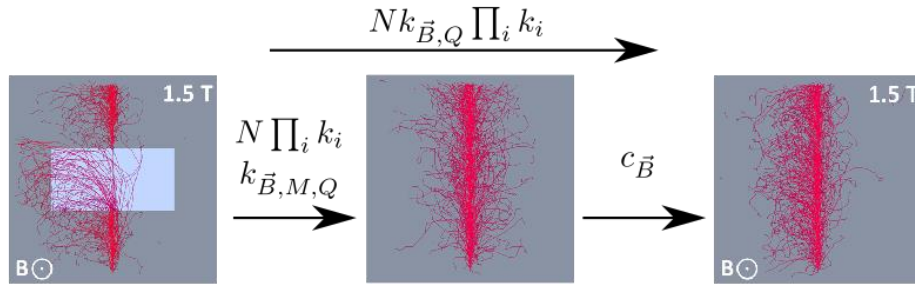


Figure 19: Illustration of the formalism to correct the response of an ionization chamber that is influenced by a magnetic field. First  $k_{\vec{B},M,Q}$ , the calibration factor  $N$  and the usual correction factors  $k_i$  are applied to calculate the dose that would have been deposited, if there wouldn't be any magnetic field. Then,  $c_{\vec{B}}$  is used to calculate the deposited dose in the measurement situation (with magnetic field).

Quantity	Used by	Corrects for	Equivalent to
$P_{1.5\text{ T}}$	Smit et al., 2013	Magnetic Field (1.5 T), Change of Dose to Water	$k_{\vec{B},M,Q}$
$k_{\vec{B},M,Q}$	van Asselen et al., 2018, Pojtinger et al., 2019	Magnetic Field, Change of Dose to Water	$k_{\vec{B},Q}/c_{\vec{B}}, P_{1.5\text{ T}}$
$k_{\vec{B},Q}$	van Asselen et al., 2018 Pojtinger et al., 2020	Magnetic Field	$k_B^{Q_{\text{mrs}}}, k_B, k_B^Q$
$k_B^{Q_{\text{msr}}}$	O'Brien et al., 2016	Magnetic Field	$k_{\vec{B},Q}$
$k_B$	Malkov and Rogers, 2018, Pojtinger et al., 2018	Magnetic Field	$k_{\vec{B},Q}$
$k_B^Q$	Spindeldreier et al., 2017	Magnetic Field	$k_B$
$k_{Q,B}$	De Prez et al., 2018	Magnetic Field, Beam Quality	$k_B^Q k_Q$
$k_Q^{\text{mag}}$	Malkov and Rogers, 2018 Iakovenko et al., 2020	Magnetic Field, Beam Quality	$k_{Q,B}$

Table 3: Quantities that have been defined by different authors for the characterization of the response of ionization chambers in magnetic fields.

## Chemical Radiation Detectors in MRgRT-Dosimetry

As chemical radiation detectors like alanine pellets and Fricke solutions do not contain any air cavities and have similar properties to water, it can be assumed, that magnetic fields have no impact on the response of this type of detectors. Accordingly, these

types of detectors are a promising option to be used as a secondary standard for the absorbed dose to water or for the measurement of  $c_{\bar{B}}$ .

In this part, PTB cooperated with the Federal Institute of Metrology (METAS, Wabern, Switzerland) to gain information about the suitability of dosimetry based on Fricke solutions in the presence of magnetic fields. The experiments were carried out at PTB and the results were published in a research paper (Trachsel *et al* 2020). The influence of magnetic fields on alanine dosimetry was investigated by the National Physics Laboratory (NPL, London, Great Britain). The results can be found in the literature (Billas *et al* 2020). Both publications report  $k_{\bar{B},Q}$  values for the chemical detectors under investigation.

For dosimetry based on a Fricke solution, it was found that  $k_{\bar{B},Q} = 0.9948$  and  $k_{\bar{B},Q} = 0.9980$ , for magnetic flux densities of  $B = 0.35$  T and  $B = 1.42$  T, respectively. “These small corrections hardly exceed the measurement uncertainties. In addition, Trachsel *et al.* (Trachsel *et al* 2020) included an uncertainty budget that results in a relative combined standard uncertainty of 0.494%. “Hence, we could proof that the Fricke detector is not significantly influenced by the presence of a magnetic field”, (Trachsel *et al* 2020). For the calculation of  $k_{\bar{B},Q}$ , the  $c_{\bar{B}}$  values were taken from Delfs *et al.* (Delfs *et al* 2018). These values were chosen because they were calculated for the same experimental setup that has been used in the experiments of Trachsel *et al.* (Trachsel *et al* 2020) and was described in detail by Pojtinger *et al.* (Pojtinger *et al* 2019). Anyway, using the  $c_{\bar{B}}$  values presented by Billas *et al.* (Billas *et al* 2020),  $k_{\bar{B},Q}$  for the Fricke solution results in  $k_{\bar{B},Q} = 0.9992$  for a magnetic flux density of  $B = 0.35$  T. This value is within the relative combined standard uncertainty. These results show that dosimetry based on Fricke solution is a promising tool for absolute dosimetry in magnetic fields.

In the work of Billas *et al.* (Billas *et al* 2020), the authors published  $k_{\bar{B},Q}$  values as well as the corresponding uncertainty budget for alanine dosimetry in magnetic fields. For 6 MV, the authors reported  $k_{\bar{B},Q} = 1.0011 \pm 0.0030$  and  $k_{\bar{B},Q} = 1.0067 \pm 0.0061$ , for magnetic flux densities of  $B = 0.35$  T and  $B = 1.5$  T, respectively. For 8 MV, the authors reported  $k_{\bar{B},Q} = 1.0038 \pm 0.0030$  and  $k_{\bar{B},Q} = 1.0099 \pm 0.0056$ , for  $B = 0.35$  T and  $B = 1.5$  T, respectively. The authors concluded that the magnetic field changes the intrinsic sensitivity of alanine, and that these effects do not depend on the beam

quality. In a later publication, that is also part of this thesis, it was shown that the response of the PTB alanine system is not influenced for measurements at the 7 MV FFF 1.5 T MR-linac (Pojtinger *et al* 2020a).

The detailed knowledge about the influence of a magnetic field on chemical radiation detectors can be utilized for the determination of magnetic field correction factors for ionization chambers, what will be discussed in the following.

#### Magnetic Field Correction Factors for Parallel Ionization Chamber Orientations

There is one major drawback on the magnetic field correction factors that were calculated in the first part of this work. They were only benchmarked for orientations, in which the ionization chamber axis is perpendicular to the magnetic field direction. The reason for this is, that the space between the pole shoes of the electromagnet that was used for the experiments is too small to holder ionization chambers in an orientation in which the ionization chamber axis is parallel to the magnetic field direction (figure 18). But there are several benefits in using ionization chambers in the parallel orientation for dosimetric purposes. For Farmer type ionization chambers, it was shown, that the magnetic field correction factors are smaller for this orientation (Pojtinger *et al* 2017, 2018, Spindeldreier *et al* 2017, Malkov and Rogers 2018, O'Brien *et al* 2016, van Asselen *et al* 2018, de Prez *et al* 2019, Iakovenko *et al* 2020, Smit *et al* 2013). In this sense, also the uncertainties that are introduced by the correction factors are small. Another reason is, that the impact of dead volume effects is smaller in the parallel orientation (Malkov and Rogers 2018). This is an important point for small cavity ionization chambers.

To overcome this issue, two new methods were developed to measure magnetic field correction factors for parallel ionization chamber orientations. The first method is based on the use of chemical radiation detectors. For this, alanine dosimetry was used to derive experimental determined correction factors for ionization chambers in parallel orientations by cross-calibration. The second method is based on a combination of relative measurements. Magnetic field correction factors for parallel orientations were derived by combining measurements in perpendicular orientation done in an electromagnet (figure 18) with relative measurements taken at a MR-linac.

The results have been published in a research paper (Pojtinger *et al* 2020a). De Pooter *et al.* (de Pooter *et al* 2020) published the full response curves for the measurements in perpendicular orientation (figure 20), that have been measured as a part of this work.

In addition to measurements of the Farmer type ionization chamber PTW 30013 (PTW, Freiburg, Germany), this part of this work also includes results for the small cavity thimble type ionization chambers PTW 31010 (PTW, Freiburg, Germany) and PTW 31021 (PTW, Freiburg, Germany).

The results show that it is possible to derive values for  $k_{\vec{B},M,Q}$  based on alanine dosimetry. It became clear, that this method results in uncertainty budgets close to 1%. The correction factors, that have been derived from relative measurements resulted in uncertainties of less than 0.25%.

In agreement with earlier MC simulations (Pojtinger *et al* 2018), the experiments confirmed, that Farmer type ionization chambers should be used in an orientation, in which the ionization chamber axis is parallel to the magnetic field vector, as the influence of the magnetic field on the response of the ionization chamber is small in this orientation.

In the perpendicular orientation, there are two possible orientations for thimble type ionization chambers, the orientation in which the secondary electrons are deflected into the direction of the tip of the ionization chamber and the orientation in which the secondary electrons are deflected to the stem of the ionization chamber. In the following these orientations are referred to as CtT (charge to tip) and CtS (charge to stem). For the Farmer type ionization chamber under investigation the difference between the CtS and CtT orientation is of minor interest, as this type of ionization chambers should be used in parallel orientation. But in contrast to Farmer type ionization chambers, the effect of the magnetic field on the response of small cavity ionization chambers lies close to 1%, in the CtS orientation. This can result in  $k_{\vec{B},Q}$  correction factors of less than 0.5%. Therefore, the perpendicular orientation can be the better choice for small cavity ionization chambers. But the difference between the CtS and CtT orientation can exceed 5%, for small volume ionization chambers.

A measurement of the beam profile of the 7 MV MR-linac revealed, that Farmer type ionization chambers must be corrected for volume averaging effects (Pojtinger *et al* 2020a). That might be a reason for using small cavity ionization chambers for 7 MV MR-linacs. But there are other problems for small cavity ionization chambers. Though it was shown that intra-type variations are small for Farmer type ionization chambers (Woodings *et al* 2019), it was shown that this is not necessarily the case for small volume ionization chambers (Pojtinger *et al* 2020a).

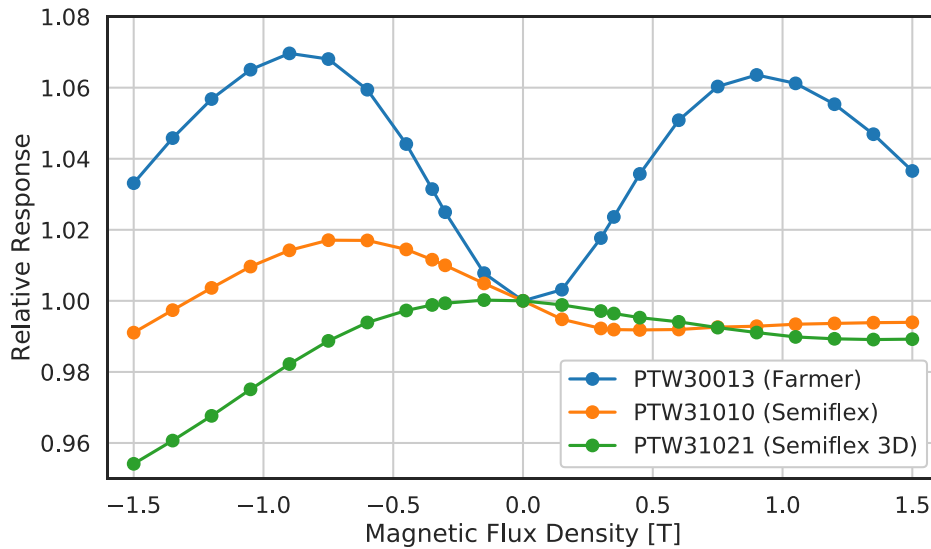


Figure 20: Relative response curves of the Farmer type ionization chamber PTW 30013 (PTW, Freiburg, Germany) and the small cavity thimble type ionization chambers PTW 31010 (PTW, Freiburg, Germany) and PTW 31021 (PTW, Freiburg, Germany). The measurements were carried out in the experimental setup described in (Pojtinger *et al* 2019). This figure was provided for the publication of (de Pooter *et al.*, 2020, licensed under CC BY 3.0).

### Monte-Carlo Simulations

Many of the early experiments and simulations were done using the Farmer type ionization chambers NE 2571 (Phoenix Dosimetry, Sandhurst, Britain) and PTW 30013 (PTW, Freiburg, Germany) in an orientation in which the magnetic field was perpendicular to the magnetic field vector, this allows some comparisons.

Pojtinger *et al.* (Pojtinger *et al* 2018) published an experimental benchmark of the presented MC-simulations up to a magnetic flux density of 1.43 T, for a PTW 30013 ionization chamber. For this, a large electromagnet was placed in front of a medical linac (figure 18) and the response of a PTW 30013 ionization chamber was measured as a function of the magnetic flux density (relative response curve), for an orientation in which the ionization chamber is perpendicular to the magnetic field vector. Similar experiments are described in literature for lower magnetic flux densities: Meijsing *et al.* (Meijsing *et al* 2009) presented magnetic field dependent response curves up to 1.2 T, for an NE 2571 ionization chamber and Spindeldreier *et al.* (Spindeldreier *et al* 2017) up to 1 T, for an PTW 30013 ionization chamber.

These experimental results were used by many authors as an experimental benchmark of their own MC simulations (Malkov and Rogers 2016, Spindeldreier *et al* 2017, Meijsing *et al* 2009, Reynolds *et al* 2013, Pojtinger *et al* 2018). In the work of Meijsing

et al. (Meijsing *et al* 2009) it was noted, that the experimental results do not align with the MC results that were included in the same publication. Discrepancies between MC calculated results and the experimental result of Meijsing et al. (Meijsing *et al* 2009) were also reported by Malkov and Rogers (Malkov and Rogers, 2016). Spindeldreier et al. (Spindeldreier *et al* 2017) described discrepancies between their own experiments and simulations. Pojtinger et al. (Pojtinger *et al* 2018) reported that “differences appear with increasing magnetic flux density”.

In addition, experimental results are published for a magnetic flux density of 1.5 T, for an NE 2571 ionization chamber (Smit et al., 2013). Also, O’Brien et al. (O’Brien *et al* 2016) published experimental results at 1.5 T for an PTW 30013 as well as a NE 2571 ionization chamber. There’s an excellent agreement between the experimental values of Smit et al. (Smit *et al.*, 2013) and the simulated results of Malkov and Rogers (Malkov and Rogers 2016). This is peculiar, as the simulated results of Malkov and Rogers (Malkov and Rogers, 2016) do not align with the the experimental results of Meijsing et al. (Meijsing *et al* 2009), for lower magnetic flux densities. O’Brien et al. (O’Brien *et al* 2016) also presented MC calculated results, that do not agree with the experimental results of Smit et al. (Smit *et al* 2013).

The experimental results of O’Brien et al. (O’Brien *et al* 2016) and the MC simulated results of Reynolds et al. (Reynolds *et al* 2017) are not suitable to be used for an experimental benchmark, due to the high uncertainties reported by the authors. In addition, experimental results for different Farmer type ionization chambers were published by Iakovenko et al. (Iakovenko *et al* 2020), but the reported uncertainties exceed 1.1%.

An overview of the most important publications on this topic is given in table 4.

### Dead Volumes

Different ideas were proposed to explain the mentioned discrepancies. One idea was, that the experiments are prone to a misalignment of the magnetic field, relative to the beam direction during the experiments (Malkov and Rogers 2016, Pojtinger *et al* 2018, Meijsing *et al* 2009).

An alternative explanation was presented in two publications (Malkov and Rogers 2017, Spindeldreier *et al* 2017). The authors speculated, that the experiments were valid but that there were problems with the MC simulations. The authors noted that the

introduction of a dead volume near the guard ring of an ionization chambers can change the effect of a magnetic field on the response of an ionization chamber drastically. To show the potential effects of the introduction of a dead volume around the guard ring, the authors modified the sensitive volume of the simulated ionization chambers by systematically including different cylindrically shaped dead volumes around the guard. With this method, the authors succeeded to fit their simulations to the experimental results up to 1.2 T.

The problem about this method is, that simulations that have been altered in a way like this, cannot be used for independent validation of experimental results. Also, it has been shown later, that the resulting cylindrical dead volumes presented (Spindeldreier *et al* 2017, Malkov and Rogers 2017) are not suitable for simulations at 1.5 T. At 1.5 T some simulations based on the dead volumes calculated by Spindeldreier *et al.* (Spindeldreier *et al.*, 2017) do not align with experimental results (figure 21).

Therefore, the second part of this work was dedicated to test the initial hypothesis of Malkov and Rogers and Spindeldreier *et al.* (Malkov and Rogers, 2017, Spindeldreier *et al.*, 2017) by a more advanced approach. This was done by combining finite-element methods (FEM) with MC methods to calculate a magnetic field dependent response curve. The MC simulations were based on a dead volume that is defined not by a fitted cylindrical form but by calculation of the actual electric field lines inside of the ionization chamber. The results were published in a research article (Pojtinger *et al* 2019). This publication also includes new experimental results. By modifying the electromagnet used for the experimental setup, it was possible to reach magnetic flux densities up to 1.5 T.

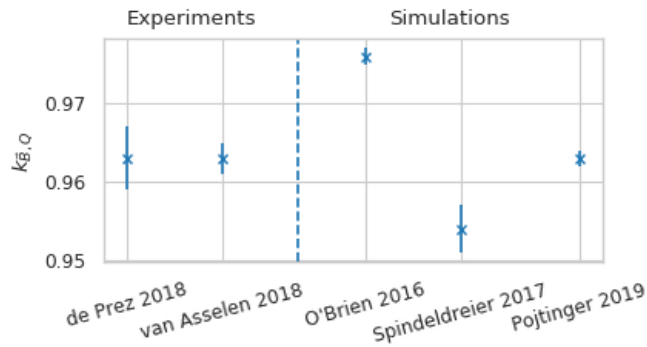


Figure 21: Comparison of the magnetic field correction for the PTW 30013 ionization chambers in an orientation in which the secondary electrons are deflected to the tip of the ionization chamber. The magnitude of the magnetic flux density was 1.5 T, for all results. Note that the simulations of (O'Brien *et al* 2016) do not include a correction for dead volume effects, the results of (Spindeldreier *et al* 2017) were simulated including a simplified, cylindrical dead volume geometry and the results of (Pojtinger *et al* 2019) were simulated including a dead volume geometry based on finite element simulations. For the calculation of the magnetic field correction of (Pojtinger *et al* 2019) the  $c_{\bar{B}}$  value of (van Asselen *et al* 2018) was used (table 1), as (Pojtinger *et al* 2019) includes values for  $k_{\bar{B},M,Q}$  only.

## Conclusions for Magnetic Field Correction Factors

Based on the presented results, the best way to do absolute dosimetry in an MR-linac environment is to use waterproof Farmer type ionization chambers in a parallel orientation. In addition, the measurements must be taken inside of a water phantom. The benefits are:

- Farmer chambers have a high response because of big sensitive volume.
- Farmer chambers are prone to misalignment, because both possible parallel orientations lead to the same magnetic field corrections and the influence of small angular misalignments is neglectable.
- Intra-type variability is low for Farmer type ionization chambers.
- There is no air gap effect caused by ERE for measurements with waterproof ionization chambers in water.

Magnetic field correction factors for ionization chambers should fulfill the following conditions:

- The Type A uncertainty given by the author should be reasonable (e.g. below 0.5%).
- For experimental setups: the field size of the photon field should be at least  $4 \times 4 \text{ cm}^2$ .



- Correction factors based on Monte-Carlo simulations should only be considered for parallel orientations or if the sensitive volume is determined by FEM.
- The correction factors must have been reproduced at least one time by an independent method.

Based on these criteria, there are currently two ionization chambers, that can be used for absolute dosimetry in magnetic fields. Namely, the PTW 30013 (PTW, Freiburg, Germany) and the IBA FC65-G ionization chamber. (IBA, Louvain-la-Neuve, Belgium). An appropriate choice of correction factors can be derived from table 4, as it is done in table 5 and table 6.

With the recommendations and correction factors elaborated in this work, precise absolute dosimetry and thus safe treatment of patients can be achieved in MRIgRT.

Method	Publication	Ionization Chamber	Orientation	Phantom	Beam Quality	Magnetic Flux Density	Limitations
Electromagnet and linac	(Meijsing <i>et al</i> 2009)	NE 2571	CtS	Delrin build-up cap (cylinder: $d = 4.3$ cm, $l = 6.9$ cm)	6 MV	0 – 1.2 T	Solid phantom material, no results for 1.5 T
MC (Geant4)	(Meijsing <i>et al</i> 2009)	NE 2571	CtS	Water (cylinder: $d = 4.3$ cm, $l = 6.9$ cm)	6 MV	0 – 2 T	No simulation of dead volume
MR and linac	(Smit <i>et al</i> 2013)	NE 2571	CtS	PMMA ( $20 \times 20 \times 13$ cm <sup>3</sup> , depth: 3.6, 7.4, 10.8 cm)	6 MV	1.5 T	Solid phantom material
MC (EGSnrc)	(Malkov and Rogers 2016)	NE 2571	CtS	Delrin (cylinder: $d = 4.3$ cm, $l = 6.9$ cm)	6 MV	0 – 2 T	No simulation of dead volume
MC (Geant4)	(O'Brien <i>et al</i> 2016)	PTW 30013, NE 2571	CtS, CtT, parallel	Water ( $30 \times 30 \times 30$ cm <sup>3</sup> , depth: 10 cm)	7 MV FFF	1.5 T	No simulation of dead volume
MC (EGSnrc)	(Spindeldreier <i>et al</i> 2017)	PTW 30013	CtS, CtT, parallel	Water ( $50 \times 50 \times 50$ cm <sup>3</sup> , depth: 10 cm)	6 MV	0 – 3 T	For CtS, CtT at 1.5 T: to simple dead volume
Electromagnet and linac	(Spindeldreier <i>et al</i> 2017)	PTW 30013	CtS, CtT	Water ( $12 \times 3.5 \times 15$ cm <sup>3</sup> , depth: 10 cm)	6 MV	0 – 1.1 T	Small field size ( $3 \times 10$ cm <sup>2</sup> ). No results for 1.5 T
MC (EGSnrc)	(Pojtinger <i>et al</i> 2018)	PTW 30013, NE 2571	CtT, parallel	Water ( $30 \times 30 \times 20$ cm <sup>3</sup> , depth: 10 cm)	7 MV FFF, 6 MV FFF	0 – 2.5 T (7 MV FFF), 0.35 T (6 MV FFF)	No simulation of dead volume
MC (EGSnrc)	(Pojtinger <i>et al</i> 2018)	PTW 30013	CtT, parallel	Water ( $21 \times 7 \times 21$ cm <sup>3</sup> , depth: 10 cm)	6 MV	0 – 1.5 T	No simulation of dead volume

MC (EGSnrc)	(Pojtinger <i>et al</i> 2018)	NE 2571	CtS	PMMA ( $30 \times 30 \times 20 \text{ cm}^3$ , depth: 10 cm)	6 MV	1.5 T	No simulation of dead volume
Electromagnet and linac	(Pojtinger <i>et al</i> 2018)	PTW 30013	CtT	Water ( $21 \times 7 \times 21 \text{ cm}^3$ , depth: 10 cm)	6 MV	0 – 1.43 T	No results for 1.5 T
MC (EGSnrc)	(Malkov and Rogers 2018)	PTW 30013, IBA FC65-G, NE 2571, SI Exradin (A12, A19)	CtS, CtT, parallel	Water ( $30 \times 30 \times 30 \text{ cm}^3$ , depth: 10 cm)	7 MV FFF	1.5 T	For CtS, CtT at 1.5 T: to simple dead volume
MR-linac	(van Asselen <i>et al</i> 2018)	PTW 30013, IBA FC65-G	CtT, parallel	Water ( $37 \times 32 \times 32 \text{ cm}^3$ , depth: 10 cm)	7 MV FFF	1.5 T	
MR-linac (calorimeter)	(de Prez <i>et al</i> 2019)	PTW 30013, IBA FC65-G	CtT, parallel	Water ( $25 \times 32 \times 37 \text{ cm}^3$ , depth: 10 cm)	7 MV FFF	1.5 T	
MC (EGSnrc)	(Pojtinger <i>et al</i> 2019)	PTW 30013	CtS, CtT	Water ( $30 \times 30 \times 20 \text{ cm}^3$ , depth: 10 cm)	6 MV	0 – 1.5 T	No results for parallel orientations
Electromagnet and linac	(Pojtinger <i>et al</i> 2019)	PTW 30013	CtS, CtT	Water ( $21 \times 6 \times 21 \text{ cm}^3$ , depth: 10 cm)	6 MV	0 – 1.5 T	No results for parallel orientations
MR-linac (calorimeter)	(Krauss <i>et al</i> 2020)	IBA FC65-G, PTW 30013, SI Exradin A19MR	CtS, parallel	( $22 \times 24 \times 30 \text{ cm}^3$ , depth: 10 cm)	6 MV FFF	0.35 T	No results for 1.5 T
MR-linac in combination with conventional linacs and electromagnet	(Pojtinger <i>et al</i> 2020a)	PTW 30013	Parallel	Water ( $21 \times 6 \times 21 \text{ cm}^3$ , depth: 10 cm)	7 MV FFF	1.5 T	No results for 0.35 T

Table 4: List of experimental and simulation results for the quantification of the response of Farmer type ionization chambers in magnetic fields. Only results that have been published in peer-reviewed journals, that include at least results up to 0.35 T and report Type A uncertainties below 0.5% have been included. CtT notes the ionization chamber orientation, in which the secondary electrons are deflected to the tip of the ionization chamber, CtS notes the orientation in which the secondary electrons are deflected to the stem of the ionization chamber and parallel notes the orientation, in which the ionization chamber axis is parallel to the magnetic field vector. For all results, the magnetic field vector is always perpendicular to the beam direction. In the range of 0 – 1 T, MC simulations should include at least a simplified dead volume modelling, in CtT and CtS orientations. For higher magnetic flux densities, a detailed model of the dead volume must be used for CtT and CtS orientations.

<b>PTW 30013 parallel</b>	<b>0.35 T</b>	<b>1.5 T</b>
(O'Brien <i>et al</i> 2016)	-	0.9940(15)
(Spindeldreier <i>et al</i> 2017)*	0.9968(30)	0.9930(30)
(Pojtinger <i>et al</i> 2018)	0.9976(16)	0.9963(16)
(Malkov and Rogers 2018)	-	0.9881(10)
(van Asselen <i>et al</i> 2018)	-	0.9920(20)
(de Prez <i>et al</i> 2019)	-	0.9850(50)
(Pojtinger <i>et al</i> 2020a)	-	0.9926(22)
(Krauss <i>et al</i> 2020)	0.9936(77)	-
<b>mean and standard error</b>	<b>0.9960(12)</b>	<b>0.9916(15)</b>

Table 5:  $k_{\bar{B},Q}$  values for the PTW 30013 ionization chamber. \*As the authors did not report any results for  $B = 0.35$  T, the average value was taken from the results for  $B = 0.3$  T and  $B = 0.4$  T.

<b>IBA FC65-G parallel</b>	<b>0.35 T</b>	<b>1.5 T</b>
(Malkov and Rogers 2018)	-	0.9970(30)
(van Asselen <i>et al</i> 2018)	-	0.9970(30)
(de Prez <i>et al</i> 2019)	-	0.9950(40)
(Krauss <i>et al</i> 2020)	0.9936(77)	-
<b>mean and standard error</b>	<b>-</b>	<b>0.9946(15)</b>

Table 6:  $k_{\bar{B},Q}$  values for the IBA FC65-G ionization chamber.

## Literature

Agostinelli S, Allison J, Amako K, Apostolakis J, Araujo H, Arce P, Asai M, Axen D, Banerjee S, Barrand G, Behner F, Bellagamba L, Boudreau J, Broglia L, Brunengo A, Burkhardt H, Chauvie S, Chuma J, Chytracek R, Cooperman G, Cosmo G, Degtyarenko P, Dell'Acqua A, Depaola G, Dietrich D, Enami R, Feliciello A, Ferguson C, Fesefeldt H, Folger G, Foppiano F, Forti A, Garelli S, Giani S, Giannitrapani R, Gibin D, Gomez Cadenas J J, Gonzalez I, Gracia Abril G, Greeniaus G, Greiner W, Grichine V, Grossheim A, Guatelli S, Gumplinger P, Hamatsu R, Hashimoto K, Hasui H, Heikkinen A, Howard A, Ivanchenko V, Johnson A, Jones F W, Kallenbach J, Kanaya N, Kawabata M, Kawabata Y, Kawaguti M, Kelner S, Kent P, Kimura A, Kodama T, Kokoulin R, Kossov M, Kurashige H, Lamanna E, Lampen T, Lara V, Lefebure V, Lei F, Liendl M, Lockman W, Longo F, Magni S, Maire M, Medernach E, Minamimoto K, Mora de Freitas P, Morita Y, Murakami K, Nagamatu M, Nartallo R, Nieminen P, Nishimura T, Ohtsubo K, Okamura M, O'Neale S, Oohata Y, Paech K, Perl J, Pfeiffer A, Pia M G, Ranjard F, Rybin A, Sadilov S, di Salvo E, Santin G, Sasaki T, et al 2003 GEANT4 - A simulation toolkit *Nucl. Instruments Methods Phys. Res. Sect. A Accel. Spectrometers, Detect. Assoc. Equip.* 506 250–303 DOI: 10.1016/S0168-9002(03)01368-8

Ahmad S B, Sarfehnia A, Paudel M R, Kim A, Hissoiny S, Sahgal A and Keller B 2016 Evaluation of a commercial MRI Linac based Monte Carlo dose calculation algorithm with GEANT 4 *Med. Phys.* 43 894–907 DOI: 10.1118/1.4939808

Aird E G A and Farmer F T 1972 The design of a thimble chamber for the Farmer dosimeter *Phys. Med. Biol.* 17 169–74 DOI: 10.1088/0031-9155/17/2/001

Allisy A, Jennings W A, Kellerer A M, Müller J W, Rossi H H and Seltzer S M 1998 ICRU Report 60: Fundamental Quantities and Units for Ionizing Radiation *J. Int. Comm. Radiat. Units Meas.* os31 DOI: 10.1093/jicru/os31.1.Report60

Almond P R, Biggs P J, Coursey B M, Hanson W F, Huq M S, Nath R and Rogers D W O O 1999 AAPM's TG-51 protocol for clinical reference dosimetry of high-energy photon and electron beams *Med. Phys.* 26 1847–70 DOI: 10.1118/1.598691

Andreo P, Huq M S, Kanai T, Laitano F, Smyth V, Zealand N, Vynckier S, Burns D T

- and Hohlfeld K 2006 *IAEA TRS-398: Absorbed Dose Determination in External Beam Radiotherapy: An International Code of Practice for Dosimetry based on Standards of Absorbed Dose to Water* ISBN: 9789201022004
- Ashamalla H, Rafla S, Parikh K, Mokhtar B, Goswami G, Kambam S, Abdel-Dayem H, Guirguis A, Ross P and Evola A 2005 The contribution of integrated PET/CT to the evolving definition of treatment volumes in radiation treatment planning in lung cancer *Int. J. Radiat. Oncol. Biol. Phys.* 63 1016–23 DOI: 10.1016/j.ijrobp.2005.04.021
- van Asselen B, Woodings S J, Hackett S L, Van Soest T L, Kok J G M, Raaymakers B W and Wolthaus J W H 2018 A formalism for reference dosimetry in photon beams in the presence of a magnetic field *Phys. Med. Biol.* 63 125008 DOI: 10.1088/1361-6560/aac70e
- Benmakhlouf H and Andreo P 2017 Spectral distribution of particle fluence in small field detectors and its implication on small field dosimetry *Med. Phys.* 44 713–24 DOI: 10.1002/mp.12042
- Berbeco R I, Jiang S B, Sharp G C, Chen G T Y, Mostafavi H and Shirato H 2004 Integrated radiotherapy imaging system (IRIS): Design considerations of tumour tracking with linac gantry-mounted diagnostic x-ray systems with flat-panel detectors *Phys. Med. Biol.* 49 243–55 DOI: 10.1088/0031-9155/49/2/005
- Berger M 1963 *Monte Carlo calculation of the penetration and diffusion of fast charged particles* vol 1 (New York: Academic Press)
- Berger M J, Coursey J S, Zucker M A and Chang J 1998 Stopping-Power & Range Tables for Electrons, Protons, and Helium Ions *Natl. Inst. Stand. Technol. Stand. Ref. Database 124* 4999 1–17 DOI: 10.18434/T4NC7P
- Berger M J and Hubbell J H 1987 *XCOM: Photon cross sections on a personal computer* (Oak Ridge, TN) DOI: 10.2172/6016002
- Berger M J and Seltzer S M 1964 Tables of Energy Losses and Ranges of Electrons and Positrons *Natl. Aeronaut. Sp. Adm. Rep. Nasa Sp-3012* 1–134
- Bethe H 1932 Bremsformel für Elektronen relativistischer Geschwindigkeit *Zeitschrift für Phys.* 76 293–9 DOI: 10.1007/BF01342532

- Bethe H 1930 Zur Theorie des Durchgangs schneller Korpuskularstrahlen durch Materie *Ann. Phys.* 397 325–400 DOI: 10.1002/andp.19303970303
- Bethe H and Heitler W 1934 On the stopping of fast particles and on the creation of positive electrons *Proc. R. Soc. London. Ser. A, Contain. Pap. a Math. Phys. Character* 146 83–112 DOI: 10.1098/rspa.1934.0140
- Bhaba H J 1936 The scattering of positrons by electrons with exchange on Dirac's theory of the positron *Proc. R. Soc. London. Ser. A - Math. Phys. Sci.* 154 195–206 DOI: 10.1098/rspa.1936.0046
- Bielajew A F 1988 Electron Transport in E and B Fields *Monte Carlo Transport of Electrons and Photons* (Springer) pp 421–34 DOI: 10.1007/978-1-4613-1059-4\_19
- Bielajew A F, Mohan R and Chui C-S 1989 Improved bremsstrahlung photon angular sampling in the EGS4 code system *Natl. Res. Counc. Canada Rep. PIRS-0203* 1–20
- Bielajew A F and Rogers D W O 1986 Photoelectron angular distribution in the EGS4 code system *Natl. Res. Counc. Canada Rep. PIRS-0058*
- Billas I, Bouchard H, Oelfke U, Shipley D, Gouldstone C and Duane S 2020 Alanine dosimetry in strong magnetic fields: use as a transfer standard in MRI-guided radiotherapy *Phys. Med. Biol.* 65 115001 DOI: 10.1088/1361-6560/ab8148
- Boag J W 1964 Distortion of the Electric Field in an Ionization Chamber due to a Difference in Potential between Guard Ring and Collector *Phys. Med. Biol.* 9 25–32 DOI: 10.1088/0031-9155/9/1/302
- Booth J T and Zavgorodni S F 1999 Set-up error & organ motion uncertainty: a review. *Australas. Phys. Eng. Sci. Med.* 22 29–47 ISSN: 0158-9938
- Bouchard H and Bielajew A 2015 Lorentz force correction to the Boltzmann radiation transport equation and its implications for Monte Carlo algorithms *Phys. Med. Biol.* 60 4963–71 DOI: 10.1088/0031-9155/60/13/4963
- Bouchard H, de Pooter J, Bielajew A and Duane S 2015 Reference dosimetry in the presence of magnetic fields: conditions to validate Monte Carlo simulations *Phys. Med. Biol.* 60 6639–54 DOI: 10.1088/0031-9155/60/17/6639

- Boyer A L and Schultheiss T 1988 Effects of dosimetric and clinical uncertainty on complication-free local tumor control *Radiother. Oncol.* 11 65–71 DOI: 10.1016/0167-8140(88)90046-1
- Burns D T, Picard S, Kessler C and Roger P 2014 Use of the BIPM calorimetric and ionometric standards in megavoltage photon beams to determine  $W_{\text{air}}$  and  $I_c$  *Phys. Med. Biol.* 59 1353–65 DOI: 10.1088/0031-9155/59/6/1353
- Czarnecki D, Poppe B and Zink K 2018 Impact of new ICRU Report 90 recommendations on calculated correction factors for reference dosimetry *Phys. Med. Biol.* 63 155015 DOI: 10.1088/1361-6560/aad148
- Dearnaley D, Syndikus I, Mossop H, Khoo V, Birtle A, Bloomfield D, Graham J, Kirkbride P, Logue J, Malik Z, Money-Kyrle J, O'Sullivan J M, Panades M, Parker C, Patterson H, Scrase C, Staffurth J, Stockdale A, Tremlett J, Bidmead M, Mayles H, Naismith O, South C, Gao A, Cruickshank C, Hassan S, Pugh J, Griffin C and Hall E 2016 Conventional versus hypofractionated high-dose intensity-modulated radiotherapy for prostate cancer: 5-year outcomes of the randomised, non-inferiority, phase 3 CHHiP trial *Lancet Oncol.* 17 1047–60 DOI: 10.1016/S1470-2045(16)30102-4
- Delaney G, Jacob S, Featherstone C and Barton M 2005 The role of radiotherapy in cancer treatment: Estimating optimal utilization from a review of evidence-based clinical guidelines *Cancer* 104 1129–37 DOI: 10.1002/cncr.21324
- Delfs B, Schoenfeld A A, Poppinga D, Kapsch R P, Jiang P, Harder D, Poppe B and Looe H K 2018 Magnetic fields are causing small, but significant changes of the radiochromic EBT3 film response to 6 MV photons *Phys. Med. Biol.* 63 035028 DOI: 10.1088/1361-6560/aa9bd5
- Demtröder W 2017 *Experimentalphysik 4* (Berlin, Heidelberg: Springer) DOI: 10.1007/978-3-662-52884-6
- Deutsches Institut für Normung 2020 DIN 6800-2: Dosismessverfahren nach der Sondenmethode für Photonen- und Elektronenstrahlung, Teil 2: Ionisationsdosimetrie
- Dietz B, Yun J, Yip E, Gabos Z, Fallone B G and Wachowicz K 2019 Single patient convolutional neural networks for real-time MR reconstruction: a proof of concept



- application in lung tumor segmentation for adaptive radiotherapy *Phys. Med. Biol.* 64 195002 DOI: 10.1088/1361-6560/ab408e
- Fallone B G 2014 The Rotating Biplanar Linac-Magnetic Resonance Imaging System *Semin. Radiat. Oncol.* 24 200–2 DOI: 10.1016/j.semradonc.2014.02.011
- Fallone B G, Murray B, Rathee S, Stanescu T, Steciw S, Vidakovic S, Blosser E and Tymofichuk D 2009 First MR images obtained during megavoltage photon irradiation from a prototype integrated linac-MR system *Med. Phys.* 36 2084–8 DOI: 10.1118/1.3125662
- Fano U 1954 Note on the Bragg-Gray Cavity Principle for Measuring Energy Dissipation *Radiat. Res.* 1 237 DOI: 10.2307/3570368
- Farmer F T 1944 A New Integrating Dosimeter for X-ray Therapy *Br. J. Radiol.* 17 160–2 DOI: 10.1259/0007-1285-17-197-160
- Fermi E 1940 The ionization loss of energy in gases and in condensed materials *Phys. Rev.* 57 485–93 DOI: 10.1103/PhysRev.57.485
- Friedel M, Nachbar M, Mönnich D, Dohm O and Thorwarth D 2019 Development and validation of a 1.5 T MR-Linac full accelerator head and cryostat model for Monte Carlo dose simulations *Med. Phys.* 46 5304–13 DOI: 10.1002/mp.13829
- Goudsmit S and Saunderson J L 1940 Multiple scattering of electrons *Phys. Rev.* 57 24–9 DOI: 10.1103/PhysRev.57.24
- Grégoire V, Guckenberger M, Haustermans K, Lagendijk J J W, Ménard C, Pötter R, Slotman B J, Tanderup K, Thorwarth D, van Herk M and Zips D 2020 Image-guidance in radiation therapy for better cure of cancer *Mol. Oncol.* 1878-0261.12751 DOI: 10.1002/1878-0261.12751
- Hackett S L, van Asselen B, Wolthaus J W H, Kok J G M, Woodings S J, Lagendijk J J W and Raaymakers B W 2016 Consequences of air around an ionization chamber: Are existing solid phantoms suitable for reference dosimetry on an MR-linac? *Med. Phys.* 43 3961–8 DOI: 10.1118/1.4952727
- Hector C L, Evans P M and Webb S 2001 The dosimetric consequences of inter-fractional patient movement on three classes of intensity-modulated delivery techniques in breast radiotherapy *Radiother. Oncol.* 59 281–91 DOI:

10.1016/S0167-8140(01)00309-7

Hubbell J H 2006 Review and history of photon cross section calculations *Phys. Med. Biol.* 51 245–62 DOI: 10.1088/0031-9155/51/13/R15

Hubbell J H, Gimm H A and Overbo I 1980 Pair, Triplet, and Total Atomic Cross Sections (and Mass Attenuation Coefficients) for 1 MeV–100 GeV Photons in Elements Z=1 to 100 *J. Phys. Chem. Ref. Data* 9 1023–148 DOI: 10.1063/1.555629

Hubbell J H, Veigele W J, Briggs E A, Brown R T, Cromer D T and Howerton R J 1975 Atomic form factors, incoherent scattering functions, and photon scattering cross sections *J. Phys. Chem. Ref. Data* 4 471–538 DOI: 10.1063/1.555523

Iakovenko V, Keller B, Sahgal A and Sarfehnia A 2020 Experimental measurement of ionization chamber angular response and associated magnetic field correction factors in MR-linac *Med. Phys.* 47 1940–8 DOI: 10.1002/mp.14025

Jaffray D A 2007 *Image-Guided Radiation Therapy: From Concept to Practice* vol 17 (Elsevier) DOI: 10.1016/j.semradonc.2007.08.001

Kamino Y, Takayama K, Kokubo M, Narita Y, Hirai E, Kawawada N, Mizowaki T, Nagata Y, Nishidai T and Hiraoka M 2006 Development of a four-dimensional image-guided radiotherapy system with a gimbaled X-ray head *Int. J. Radiat. Oncol. Biol. Phys.* 66 271–8 DOI: 10.1016/j.ijrobp.2006.04.044

Kawrakow I 2000 Accurate condensed history Monte Carlo simulation of electron transport. II. Application to ion chamber response simulations *Med. Phys.* 27 499–513 DOI: 10.1118/1.598918

Kawrakow I, Mainegra-Hing E, Rogers D W O, Tessier F and Walters B R B 2019 The EGSnrc Code System: Monte Carlo Simulation of Electron and Photon Transport *Natl. Res. Counc. Canada Rep. PIRS-701*

Keall P J, Barton M and Crozier S 2014 The Australian Magnetic Resonance Imaging–Linac Program *Semin. Radiat. Oncol.* 24 203–6 DOI: 10.1016/j.semradonc.2014.02.015

Klein O and Nishina T 1929 Über die Streuung von Strahlung durch freie Elektronen nach der neuen relativistischen Quantendynamik von Dirac *Zeitschrift für Phys.*

52 853–68 DOI: 10.1007/BF01366453

Klüter S 2019 Technical design and concept of a 0.35 T MR-Linac *Clin. Transl. Radiat. Oncol.* 18 98–101 DOI: 10.1016/j.ctro.2019.04.007

Koch H W and Motz J W 1959 Bremsstrahlung cross-section formulas and related data *Rev. Mod. Phys.* 31 920–55 DOI: 10.1103/RevModPhys.31.920

Krauss A 2006 The PTB water calorimeter for the absolute determination of absorbed dose to water in 60 Co radiation *Metrologia* 43 259–72 DOI: 10.1088/0026-1394/43/3/008

Krauss A, Spindeldreier C K and Klüter S 2020 Direct determination of kBQ for cylindrical ionization chambers in a 6 MV 0.35 T MR-linac *Phys. Med. Biol.* 65 235049 DOI: 10.1088/1361-6560/abab56

Kron T, Eyles D, Schreiner L J and Battista J 2006 Magnetic resonance imaging for adaptive cobalt tomotherapy: A proposal *J. Med. Phys.* 31 242–54 DOI: 10.4103/0971-6203.29194

Liney G P, Dong B, Begg J, Vial P, Zhang K, Lee F, Walker A, Rai R, Causer T, Alnaghy S J, Oborn B M, Holloway L, Metcalfe P, Barton M, Crozier S and Keall P 2016 Technical Note: Experimental results from a prototype high-field inline MRI-linac *Med. Phys.* 43 5188–94 DOI: 10.1118/1.4961395

Liney G P, Dong B, Weber E, Rai R, Destruel A, Garcia-Alvarez R, Manton D J, Jelen U, Zhang K, Barton M, Keall P and Crozier S 2018a Imaging performance of a dedicated radiation transparent RF coil on a 1.0 Tesla inline MRI-linac *Phys. Med. Biol.* 63 DOI: 10.1088/1361-6560/aac813

Liney G P, Whelan B, Oborn B, Barton M and Keall P 2018b MRI-Linear Accelerator Radiotherapy Systems *Clin. Oncol.* 30 686–91 DOI: 10.1016/j.clon.2018.08.003

Ma C and Nahum A E 1991 Bragg-Gray theory and ion chamber dosimetry for photon beams *Phys. Med. Biol.* 36 413–28 DOI: 10.1088/0031-9155/36/4/001

Malkov V N and Rogers D W O 2016 Charged particle transport in magnetic fields in EGSnrc *Med. Phys.* 43 4447–58 DOI: 10.1118/1.4954318

Malkov V N and Rogers D W O 2018 Monte Carlo study of ionization chamber magnetic field correction factors as a function of angle and beam quality *Med.*

*Phys.* 45 908–25 DOI: 10.1002/mp.12716

Malkov V N and Rogers D W O 2017 Sensitive volume effects on Monte Carlo calculated ion chamber response in magnetic fields *Med. Phys.* DOI: 10.1002/mp.12421

Meijsing I, Raaymakers B W, Raaijmakers A J E, Kok J G M, Hogeweg L, Liu B and Legendijk J J W 2009 Dosimetry for the MRI accelerator: the impact of a magnetic field on the response of a Farmer NE2571 ionization chamber *Phys. Med. Biol.* 54 2993–3002 DOI: 10.1088/0031-9155/54/10/002

Metropolis N and Ulam S 1949 The Monte Carlo Method *J. Am. Stat. Assoc.* 44 335–41 DOI: 10.1080/01621459.1949.10483310

Moliere G 1948 Theorie der Streuung schneller geladener Teilchen II Mehrfach- und Vielfachstreuung *Zeitschrift für Naturforsch. A* 3 78–97 DOI: 10.1515/zna-1948-0203

Møller C 1932 Zur Theorie des Durchgangs schneller Elektronen durch Materie *Ann. Phys.* 406 531–85 DOI: 10.1002/andp.19324060506

Motz J W, Olsen H and Koch H W 1964 Electron scattering without atomic or nuclear excitation *Rev. Mod. Phys.* 36 881–928 DOI: 10.1103/RevModPhys.36.881

Mutic S and Dempsey J F 2014 The ViewRay System: Magnetic Resonance–Guided and Controlled Radiotherapy *Semin. Radiat. Oncol.* 24 196–9 DOI: 10.1016/j.semradonc.2014.02.008

Naghavi M, Abajobir A A, Abbafati C, Abbas K M, Abd-Allah F, Abera S F, Aboyans V, Adetokunboh O, Afshin A, Agrawal A, Ahmadi A, Ahmed M B, Aichour A N, Aichour M T E, Aichour I, Aiyar S, Alahdab F, Al-Aly Z, Alam K, Alam N, Alam T, Alene K A, Al-Eyadhy A, Ali S D, Alizadeh-Navaei R, Alkaabi J M, Alkerwi A, Alla F, Allebeck P, Allen C, Al-Raddadi R, Alsharif U, Altirkawi K A, Alvis-Guzman N, Amare A T, Amini E, Ammar W, Amoako Y A, Anber N, Andersen H H, Andrei C L, Androudi S, Ansari H, Antonio C A T, Anwari P, Ärnlöv J, Arora M, Artaman A, Aryal K K, Asayesh H, Asgedom S W, Atey T M, Avila-Burgos L, Avokpaho E F G, Awasthi A, Babalola T K, Bacha U, Balakrishnan K, Barac A, Barboza M A, Barker-Collo S L, Barquera S, Barregard L, Barrero L H, Baune B T, Bedi N, Beghi E, Béjot Y, Bekele B B, Bell M L, Bennett J R, Bensenor I M, Berhane A,

- Bernabé E, Betsu B D, Beuran M, Bhatt S, Biadgilign S, Bienhoff K, Bikbov B, Bisanzio D, Bourne R R A, Breitborde N J K, Bulto L N B, Bumgarner B R, Butt Z A, Cahuana-Hurtado L, Cameron E, Campuzano J C, Car J, Cárdenas R, Carrero J J, Carter A, Casey D C, Castañeda-Orjuela C A, Catalá-López F, Charlson F J, Chibueze C E, et al 2017 Global, regional, and national age-sex specific mortality for 264 causes of death, 1980–2016: a systematic analysis for the Global Burden of Disease Study 2016 *Lancet* 390 1151–210 DOI: 10.1016/S0140-6736(17)32152-9
- Njeh C F, Dong L and Orton C G 2013 IGRT has limited clinical value due to lack of accurate tumor delineation *Med. Phys.* 40 040601 DOI: 10.1118/1.4789492
- O'Brien D J, Dolan J, Pencea S, Schupp N and Sawakuchi G O 2017 Relative dosimetry with an MR-linac: Response of ion chambers, diamond, and diode detectors for off-axis, depth dose, and output factor measurements *Med. Phys.* DOI: 10.1002/mp.12699
- O'Brien D J, Dolan J, Pencea S, Schupp N and Sawakuchi G O 2018 Relative dosimetry with an MR-linac: Response of ion chambers, diamond, and diode detectors for off-axis, depth dose, and output factor measurements *Med. Phys.* 45 884–97 DOI: 10.1002/mp.12699
- O'Brien D J, Roberts D A, Ibbott G S and Sawakuchi G O 2016 Reference dosimetry in magnetic fields: formalism and ionization chamber correction factors *Med. Phys.* 43 4915–27 DOI: 10.1118/1.4959785
- O'Brien D J and Sawakuchi G O 2017 Monte Carlo study of the chamber-phantom air gap effect in a magnetic field *Med. Phys.* DOI: 10.1002/mp.12290
- Oborn B M, Ge Y, Hardcastle N, Metcalfe P E and Keall P J 2015 Dose enhancement in radiotherapy of small lung tumors using inline magnetic fields: A Monte Carlo based planning study *Med. Phys.* 43 368–77 DOI: 10.1118/1.4938580
- Olsen J, Green O and Kashani R 2015 World's First Application of MR-Guidance for Radiotherapy. *Mo. Med.* 112 358–60 ISSN: 0026-6620
- Olszanski A, Klassen N V, Ross C K and Shortt K R 2002 The IRS Fricke Dosimetry System *Natl. Res. Counc. Rep. PIRS-0815*

- Onishi H, Kuriyama K, Komiyama T, Tanaka S, Sano N, Aikawa Y, Tateda Y, Araki T, Ikenaga S and Uematsu M 2003 A new irradiation system for lung cancer combining linear accelerator, computed tomography, patient self-breath-holding, and patient-directed beam-control without respiratory monitoring devices *Int. J. Radiat. Oncol. – Biol. – Phys.* 56 14–20 DOI: 10.1016/S0360-3016(02)04414-0
- Pojtinger S, Dohm O S, Kapsch R-P and Thorwarth D 2018 Ionization chamber correction factors for MR-linacs *Phys. Med. Biol.* 63 11NT03 DOI: 10.1088/1361-6560/aac4f2
- Pojtinger S, Dohm O S and Thorwarth D 2017 Optimal orientation for ionization chambers in MRgRT reference dosimetry *Curr. Dir. Biomed. Eng.* 3 273–5 DOI: 10.1515/cdbme-2017-0056
- Pojtinger S, Kapsch R-P, Dohm O S and Thorwarth D 2019 A finite element method for the determination of the relative response of ionization chambers in MR-linacs: simulation and experimental validation up to 1.5 T *Phys. Med. Biol.* 64 135011 DOI: 10.1088/1361-6560/ab2837
- Pojtinger S, Nachbar M, Ghandour S, Pisaturo O, Pachoud M, Kapsch R-P and Thorwarth D 2020a Experimental determination of magnetic field correction factors for ionization chambers in parallel and perpendicular orientations *Phys. Med. Biol.* 65 245044 DOI: 10.1088/1361-6560/abca06
- Pojtinger S, Nachbar M, Kapsch R-P and Thorwarth D 2020b Influence of beam quality on reference dosimetry correction factors in magnetic resonance guided radiation therapy *Phys. Imaging Radiat. Oncol.* 16 95–8 DOI: 10.1016/j.phro.2020.10.005
- Pollard J M, Wen Z, Sadagopan R, Wang J and Ibbott G S 2017 The future of image-guided radiotherapy will be MR guided *Br. J. Radiol.* 90 DOI: 10.1259/bjr.20160667
- de Pooter J A, Billas I, de Prez L A, Duane S, Kapsch R-P, Karger C, van Asselen B and Wolthaus J W H 2020 Reference dosimetry in MRI-linacs: evaluation of available protocols and data to establish a code of practice *Phys. Med. Biol.* DOI: 10.1088/1361-6560/ab9efe
- de Pooter J A, de Prez L A and Bouchard H 2015 Application of an adapted Fano

cavity test for Monte Carlo simulations in the presence of B-fields *Phys. Med. Biol.* 60 9313–27 DOI: 10.1088/0031-9155/60/24/9313

Pouliot J, Bani-Hashemi A, Josephine Chen, Svatos M, Ghelmansarai F, Mitschke M, Aubin M, Xia P, Morin O, Bucci K, Roach M, Hernandez P, Zheng Z, Hristov D and Verhey L 2005 Low-dose megavoltage cone-beam CT for radiation therapy *Int. J. Radiat. Oncol. Biol. Phys.* 61 552–60 DOI: 10.1016/j.ijrobp.2004.10.011

de Prez L, Woodings S, de Pooter J, van Asselen B, Wolthaus J, Jansen B and Raaymakers B 2019 Direct measurement of ion chamber correction factors,  $k_Q$  and  $k_B$ , in a 7 MV MRI-linac *Phys. Med. Biol.* 64 105025 DOI: 10.1088/1361-6560/ab1511

Raaijmakers A J E, Raaymakers B W and Lagendijk J J W 2005 Integrating a MRI scanner with a 6 MV radiotherapy accelerator: dose increase at tissue–air interfaces in a lateral magnetic field due to returning electrons *Phys. Med. Biol.* 50 1363–76 DOI: 10.1088/0031-9155/50/7/002

Raaymakers B W, Jürgenliemk-Schulz I M, Bol G H, Glitzner M, Kotte A N T J, van Asselen B, de Boer J C J, Bluemink J J, Hackett S L, Moerland M A, Woodings S J, Wolthaus J W H, van Zijp H M, Philippens M E P, Tijssen R, Kok J G M, de Groot-van Breugel E N, Kiekebosch I, Meijers L T C, Nomden C N, Sikkes G G, Doornaert P A H, Eppinga W S C, Kasperts N, Kerkmeijer L G W, Tersteeg J H A, Brown K J, Pais B, Woodhead P and Lagendijk J J W 2017 First patients treated with a 1.5 T MRI-Linac: clinical proof of concept of a high-precision, high-field MRI guided radiotherapy treatment *Phys. Med. Biol.* 62 41–50 DOI: 10.1088/1361-6560/aa9517

Raaymakers B W, Lagendijk J J W, Overweg J, Kok J G M, Raaijmakers A J E, Kerkhof E M, van der Put R W, Meijnsing I, Crijns S P M, Benedosso F, van Vulpen M, de Graaff C H W, Allen J and Brown K J 2009 Integrating a 1.5 T MRI scanner with a 6 MV accelerator: proof of concept *Phys. Med. Biol.* 54 229–37 DOI: 10.1088/0031-9155/54/12/N01

Raaymakers B W, Raaijmakers A J E E, Kotte A N T J T J, Jette D and Lagendijk J J W W 2004 Integrating a MRI scanner with a 6 MV radiotherapy accelerator: dose deposition in a transverse magnetic field *Phys. Med. Biol.* 49 4109–18 DOI: 10.1088/0031-9155/49/17/019

- Regulla D F and Deffner U 1982 Dosimetry by ESR spectroscopy of alanine *Int. J. Appl. Radiat. Isot.* 33 1101–14 DOI: 10.1016/0020-708X(82)90238-1
- Reynolds M, Fallone B G and Rathee S 2013 Dose response of selected ion chambers in applied homogeneous transverse and longitudinal magnetic fields. *Med. Phys.* 40 042102 DOI: 10.1118/1.4794496
- Reynolds M, Rathee S and Fallone B G 2017 Technical Note: Ion chamber angular dependence in a magnetic field *Med. Phys.* 44 4322–8 DOI: 10.1002/mp.12405
- Richter S, Pojtinger S, Mönnich D, Dohm O S and Thorwarth D 2017 Influence of a transverse magnetic field on the dose deposited by a 6 MV linear accelerator *Curr. Dir. Biomed. Eng.* 3 DOI: 10.1515/cdbme-2017-0058
- Rietzel E, Rosenthal S J, Gierga D P, Willett C G and Chen G T Y 2004 Moving targets: Detection and tracking of internal organ motion for treatment planning and patient set-up *Radiotherapy and Oncology* vol 73 DOI: 10.1016/S0167-8140(04)80018-5
- Rogers D W O 2006 Fifty years of Monte Carlo simulations for medical physics *Phys. Med. Biol* 51 287–301 DOI: 10.1088/0031-9155/51/13/R17
- Ross C K 2009 Comments on ‘Ionization chamber volume determination and quality assurance using micro-CT imaging’ *Phys. Med. Biol.* 54 23–7 DOI: 10.1088/0031-9155/54/6/L01
- Salvat F, Fernández-Vera J and Sempau J 2009 *PENELOPE-2008: A Code System for Monte Carlo Simulation of Electron and Photon Transport* (Paris: Organisation for Economic Co-Operation and Development - Nuclear Energy Agency) ISBN: 978-92-64-99066-1
- Scofield J H 1973 *Theoretical photoionization cross sections from 1 to 1500 keV.* (U.S. Atomic Energy Commission) DOI: 10.2172/4545040
- Seltzer S M and Berger M J 1986 Bremsstrahlung energy spectra from electrons with kinetic energy 1 keV-10 GeV incident on screened nuclei and orbital electrons of neutral atoms with  $Z = 1-100$  *At. Data Nucl. Data Tables* 35 345–418 DOI: 10.1016/0092-640X(86)90014-8
- Seltzer S M and Berger M J 1985 Bremsstrahlung spectra from electron interactions



- with screened atomic nuclei and orbital electrons *Nucl. Inst. Methods Phys. Res. B* 12 95–134 DOI: 10.1016/0168-583X(85)90707-4
- Seltzer S M, Fernández-Varea J M, Andreo P, Bergstorm Jr. P M, Burns D T, Krajcar Bronic I, Ross C K and Salvat F 2014 ICRU Report 90: Key Data for Ionizing-Radiation Dosimetry: Measurement Standards and Applications *J. ICRU* 14 1–118 DOI: 10.1093/jicru/ndw029
- Sempau J and Andreo P 2006 Configuration of the electron transport algorithm of PENELOPE to simulate ion chambers *Phys. Med. Biol.* 51 3533–48 DOI: 10.1088/0031-9155/51/14/017
- Shortt K R 1989 The temperature dependence of  $G(\text{Fe}^{3+})$  for the Fricke dosimeter *Phys. Med. Biol.* 34 1923–6 DOI: 10.1088/0031-9155/34/12/014
- Simiele E and DeWerd L 2018 On the accuracy and efficiency of condensed history transport in magnetic fields in GEANT4. *Phys. Med. Biol.* 63 235012 DOI: 10.1088/1361-6560/aaedc9
- Smit K, van Asselen B, Kok J G M, Aalbers A H L, Lagendijk J J W and Raaymakers B W 2013 Towards reference dosimetry for the MR-linac: magnetic field correction of the ionization chamber reading *Phys. Med. Biol.* 58 5945–57 DOI: 10.1088/0031-9155/58/17/5945
- Smyth V G 1986 Interface effects in the Monte Carlo simulation of electron tracks *Med. Phys.* 13 196–200 DOI: 10.1118/1.595896
- Snyder J E, St-Aubin J, Yaddanapudi S, Boczowski A, Dunkerley D A P, Graves S A and Hyer D E 2020 Commissioning of a 1.5T Elekta Unity MR-linac: A single institution experience *J. Appl. Clin. Med. Phys.* 21 160–72 DOI: 10.1002/acm2.12902
- Spindeldreier C K, Schrenk O, Bakenecker A, Kawrakow I, Burigo L, Karger C P, Greilich S and Pfaffenberger A 2017 Radiation dosimetry in magnetic fields with Farmer-type ionization chambers: Determination of magnetic field correction factors for different magnetic field strengths and field orientations *Phys. Med. Biol.* 62 6708–28 DOI: 10.1088/1361-6560/aa7ae4
- Sternheimer R M 1967 Density effect for the ionization loss of charged particles. II *Phys. Rev.* 164 349–51 DOI: 10.1103/PhysRev.164.349

- Sternheimer R M 1966 Density effect for the ionization loss of charged particles  
*Phys. Rev.* 145 247–50 DOI: 10.1103/PhysRev.145.247
- Sterpin E, Sorriaux J, Souris K, Vynckier S and Bouchard H 2014 A Fano cavity test for Monte Carlo proton transport algorithms *Med. Phys.* 41 DOI: 10.1118/1.4835475
- Thorwarth D 2015 Functional imaging for radiotherapy treatment planning: Current status and future directions - A review *Br. J. Radiol.* 88 DOI: 10.1259/bjr.20150056
- Thorwarth D, Ege M, Nachbar M, Mönnich D, Gani C, Zips D and Boeke S 2020 Quantitative magnetic resonance imaging on hybrid magnetic resonance linear accelerators: Perspective on technical and clinical validation *Phys. Imaging Radiat. Oncol.* 16 69–73 DOI: 10.1016/j.phro.2020.09.007
- Trachsel M A, Pojtinger S, Meier M, Schrader M, Kapsch R-P and Kottler C 2020 Chemical radiation dosimetry in magnetic fields: characterization of a Fricke-type chemical detector in 6 MV photon beams and magnetic fields up to 1.42 T *Phys. Med. Biol.* 65 065005 DOI: 10.1088/1361-6560/ab7360
- Troost E G C, Thorwarth D and Oyen W J G 2015 Imaging-based treatment adaptation in radiation oncology *J. Nucl. Med.* 56 1922–9 DOI: 10.2967/jnumed.115.162529
- Vassiliev O N 2017 *Monte Carlo Methods for Radiation Transport* (Cham: Springer International Publishing) DOI: 10.1007/978-3-319-44141-2
- Voss N, Ziegenhein P, Vermond L, Hoozemans J, Mencer O, Oelfke U, Luk W and Gaydadjiev G 2019 Towards real time radiotherapy simulation *Proceedings of the International Conference on Application-Specific Systems, Architectures and Processors* vol 2019-July (Institute of Electrical and Electronics Engineers Inc.) pp 173–80 DOI: 10.1109/ASAP.2019.000-6
- Wentzel G 1926 Zwei Bemerkungen über die Zerstreung korpuskularer Strahlen als Beugungserscheinung *Zeitschrift für Phys.* 40 590–3 DOI: 10.1007/BF01390457
- Whelan B, Liney G P, Dowling J A, Rai R, Holloway L, McGarvie L, Feain I, Barton M, Berry M, Wilkins R and Keall P 2017 An MRI-compatible patient rotation system - design, construction, and first organ deformation results *Med. Phys.* 44 581–8

DOI: 10.1002/mp.12065

Woodings S J, van Asselen B, van Soest T L, de Prez L A, Legendijk J J W, Raaymakers B W and Wolthaus J W H 2019 Technical Note: Consistency of PTW 30013 and FC 65-G ion chamber magnetic field correction factors *Med. Phys.* 46 mp.13623 DOI: 10.1002/mp.13623

Yi C Y, Hah S H and Yeom M S 2006 Monte Carlo calculation of the ionization chamber response to  $^{60}\text{Co}$  beam using PENELOPE *Med. Phys.* 33 1213–21 DOI: 10.1118/1.2188822

## **Appendix: Publications**

The following publications are part of this cumulative thesis and were published under CC BY-NC-ND 3.0 or 4.0.

## OPEN ACCESS

## NOTE



## Ionization chamber correction factors for MR-linacs

RECEIVED  
10 January 2018

REVISED  
2 May 2018

ACCEPTED FOR PUBLICATION  
15 May 2018

PUBLISHED  
7 June 2018

Stefan Pojtinger<sup>1,2</sup>, Oliver Steffen Dohm<sup>2</sup>, Ralf-Peter Kapsch<sup>1</sup> and Daniela Thorwarth<sup>2</sup><sup>1</sup> Physikalisch-Technische Bundesanstalt, Braunschweig, Germany<sup>2</sup> Section for Biomedical Physics, Department of Radiation Oncology, University Hospital Tübingen, Tübingen, GermanyE-mail: [Stefan.Pojtinger@ptb.de](mailto:Stefan.Pojtinger@ptb.de), [Oliver.Dohm@med.uni-tuebingen.de](mailto:Oliver.Dohm@med.uni-tuebingen.de), [Ralf-Peter.Kapsch@ptb.de](mailto:Ralf-Peter.Kapsch@ptb.de) and [Daniela.Thorwarth@med.uni-tuebingen.de](mailto:Daniela.Thorwarth@med.uni-tuebingen.de)**Keywords:** MR-guided radiotherapy, reference dosimetry, Monte Carlo, EGSnrc, MR-linac, ionization chamber

Original content from this work may be used under the terms of the [Creative Commons Attribution 3.0 licence](https://creativecommons.org/licenses/by/3.0/).

Any further distribution of this work must maintain attribution to the author(s) and the title of the work, journal citation and DOI.

**Abstract**

Previously, readings of air-filled ionization chambers have been described as being influenced by magnetic fields. To use these chambers for dosimetry in magnetic resonance guided radiotherapy (MRgRT), this effect must be taken into account by introducing a correction factor  $k_B$ .

The purpose of this study is to systematically investigate  $k_B$  for a typical reference setup for commercially available ionization chambers with different magnetic field strengths.

The Monte Carlo simulation tool EGSnrc was used to simulate eight commercially available ionization chambers in magnetic fields whose magnetic flux density was in the range of 0–2.5 T. To validate the simulation, the influence of the magnetic field was experimentally determined for a PTW30013 Farmer-type chamber for magnetic flux densities between 0 and 1.425 T.

Changes in the detector response of up to 8% depending on the magnetic flux density, on the chamber geometry and on the chamber orientation were obtained. In the experimental setup, a maximum deviation of less than 2% was observed when comparing measured values with simulated values. Dedicated values for two MR-linac systems (ViewRay MRIdian, ViewRay Inc, Cleveland, United States, 0.35 T/6 MV and Elekta Unity, Elekta AB, Stockholm, Sweden, 1.5 T/7 MV) were determined for future use in reference dosimetry.

Simulated values for thimble-type chambers are in good agreement with experiments as well as with the results of previous publications.

After further experimental validation, the results can be considered for definition of standard protocols for purposes of reference dosimetry in MRgRT.

**Introduction**

MR-linac devices that combine magnetic resonance imaging (MRI) and a linear accelerator (linac) are currently being developed with the aim of integrating the advantages of MRI into linac-based radiotherapy (RT) and enabling online adaptive MRI-guided RT (MRgRT) (Raaijmakers *et al* 2009, Fallone 2014, Keall *et al* 2014). The potential advantages of MRgRT over conventional image-guided radiotherapy when using (for example) cone beam computed tomography (CBCT) devices are its high soft tissue contrast (McPartlin *et al* 2016), its functional imaging capabilities and the absence of radiation exposure to the patient. A recent study has already concluded that the MR-linac technology is viable for clinical trials at large comprehensive cancer centers (Sanderson *et al* 2017). Despite the benefits from a medical point of view, some basic dosimetric problems persist in MRgRT.

In the presence of magnetic fields (as they occur in the MRI component of an MR-linac), the trajectories of charged particles are influenced by the Lorentz force.

This effect changes the dose deposition by secondary electrons in high-energy photon beams, especially if combinations of media such as air and water are involved. In this case, the mean free path length of secondary electrons is longer in air than in water (Raaijmakers *et al* 2005). This effect has a direct impact on reference dosimetry, where air-filled ionization chambers inside water phantoms are commonly used. The impact of an external magnetic field on dose measurements using ionization chambers was investigated previously in several studies (Meijsing *et al* 2009, Reynolds *et al* 2013, Smit *et al* 2013, O'Brien 2016, Malkov and Rogers 2017, Spindeldreier

*et al* 2017). All groups observed a change in the response of the ionization chamber that can be taken into account by a correction factor  $k_B$ .

This work systematically investigates the responses of eight commercially available ionization chambers in setups that are not created for experimental validation, but that are based on the general recommendations for reference dosimetry as recommended in current dosimetry protocols such as TRS 398 (Andreo *et al* 2006) and DIN 6800-2 (Deutsches Institut für Normung 2008). We assume that an optimal setup includes a water phantom with a minimum size of  $30 \times 30 \times 20 \text{ cm}^3$ , a photon beam with a field size of  $10 \times 10 \text{ cm}^2$  at the phantom surface and a magnetic field that is constant over the whole phantom. We validated our results in an experiment in which we set the experimental conditions to be as close as possible to the optimal setup, which is also suitable for measurement in MR-linac systems (ViewRay MRIdian, ViewRay Inc, Cleveland, United States, 0.35 T/ 6 MV and Elekta Unity, Elekta AB, Stockholm, Sweden, 1.5 T/7 MV).

## Materials and methods

### Simulation software and parameters

Calculations for this study were performed using EGSnrc (Kawrakow *et al* 2017), with the following parameters: ESTEPE = 0.01, EM ESTEPE = 0.02, ECUT = 0.521, PCUT = 0.001.

All simulations were performed with the ‘egs\_chamber’ user code published by Wulff *et al* (2008b).

Variance reduction was applied in the form of photon cross-section enhancement (XCSE) and intermediate phase-space scoring (IPSS) as described earlier by Wulff *et al* (2008b). The simulated chambers were surrounded by a cube for IPSS. Inside the cube, XCSE was used with a XCSE factor of 512.

Magnetic fields were included in the ‘egs\_chamber’ user code using the new, enhanced algorithm for electron transport in electromagnetic fields (EEMF) that was recently published by Malkov and Rogers (2016).

### Orientation

Multiple setups of hybrid MR-linacs with different orientations of the magnetic field with respect to the radiation beam have been proposed recently (Raaymakers *et al* 2009, Fallone 2014, Keall *et al* 2014). The first clinically available MRgRT systems (Dempsey *et al* 2006, Raaymakers *et al* 2009) were constructed with an orthogonal orientation of the photon beam and the magnetic field.

Generally, for accurate dose measurements, the axis of a thimble-type chamber should be perpendicular to the beam, whereas the axis of a plane-parallel chamber should be parallel to the beam. Consequently, there is only one possible orientation with respect to the magnetic field direction for a plane-parallel chamber and one free angle of orientation for a thimble-type chamber. In this work, the angle between the magnetic field axis and the chamber axis is denoted by  $\alpha$  (see figure 1).

For measurement, a setup that is easy to establish is preferable (i.e. one where the magnetic field is parallel ( $\alpha = 0$  or  $180^\circ$ ) or orthogonal ( $\alpha = 90$  or  $270^\circ$ ) to the chamber axis). For our work, we decided to use orientations of  $180^\circ$  and  $90^\circ$ . Recent publications have shown that these orientations should not be affected by any dead volume effects for magnetic flux densities of 0.35 and 1.5 T (Malkov and Rogers 2017, Spindeldreier *et al* 2017).

### Accelerator and beam models

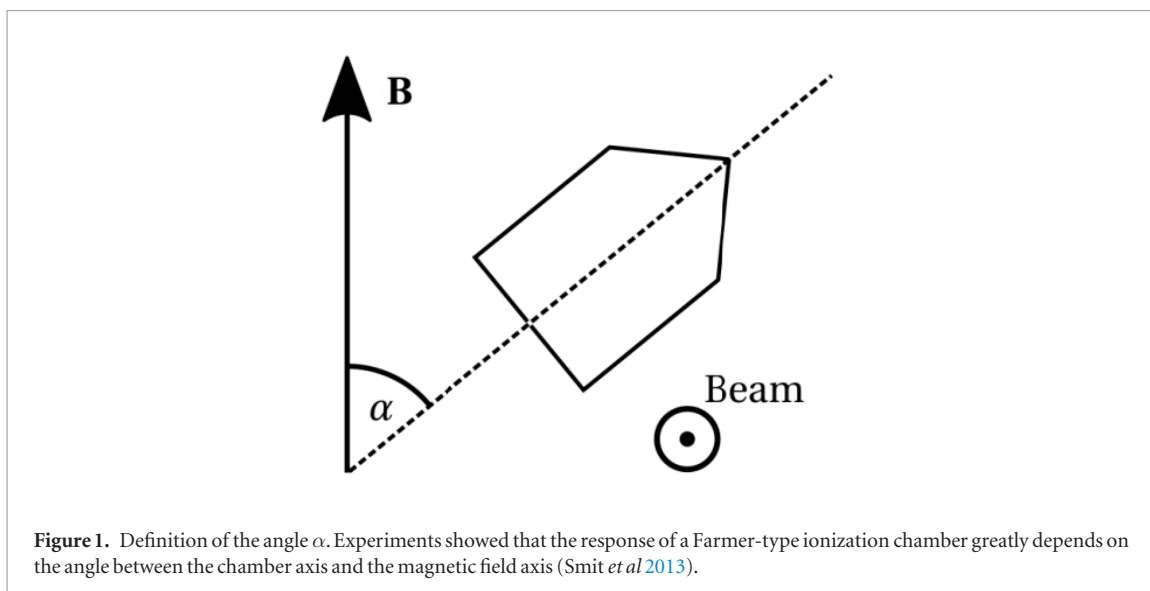
To model the accelerator, we used a full Monte Carlo simulation of a commercial Elekta 6 MV FFF linac created in BEAMnrc, as well as a published photon spectrum of the Elekta Unity MR-linac (Ahmad *et al* 2016). Such energy distributions can also be used as an input for egs\_chamber.

Two different approaches were considered. In the first approach, the full BEAMnrc model of the Elekta 6 MV FFF accelerator was directly coupled via a shared library to the egs\_chamber user code, as described by Tonkopi *et al* (2005). This method allows efficient calculations to be made on high-performance computer clusters without generating excessively large data files. For the second approach, only a rectangular  $10 \times 10 \text{ cm}^2$  photon beam was modeled instead of the full accelerator. For this, photons were randomly drawn from the 7 MV spectrum.

### Simulated ionization chambers

A list of all simulated ionization chambers together with some characteristic data is given in table 1.

Except for the PTW 30013 ionization chamber, all chamber geometries and material information have been used in previous publications (Ubrich *et al* 2008, Wulff *et al* 2008a, Zink and Wulff 2008). Simulation of the PTW 30013 ionization chamber was based on plans provided by PTW as well as on a microCT scan carried out to clarify the chamber’s geometry using a the cone-beam CT system of a small animal image-guided radiotherapy system (SAIGRT, OncoRay, Dresden, Germany) (Tillner *et al* 2016).

**Table 1.** List of the simulated ionization chambers.

Name	Manufacturer	Type	Sensitive volume [mm <sup>3</sup> ]
Roos	PTW	Plane-parallel	0.39
NACP-02	Scanditronix	Plane-parallel	0.16
Adv. Markus	PTW	Plane-parallel	0.02
Markus	PTW	Plane-parallel	0.057
PTW30015	PTW	Rigid	1
PTW30016	PTW	Rigid	0.3
NE2571	Phoenix dosimetry	Farmer	0.69
PTW30013	PTW	Farmer	0.6

### Determination of correction factors

The effects of the magnetic field on ionization chamber readings are twofold. On the one hand, the dose profile of a photon beam is influenced by the magnetic field at the lateral edges (lateral dose shift) and the depth dose decreases even if the ionization chamber is not part of the experimental setup. For small fields, this phenomenon may considerably influence the dose deposited in the measurement volume. On the other hand, the response of the ionization chamber is altered by the magnetic field presence. A correction factor for a specific ionization chamber should only include the latter effect; however, as a basic principle, a combination of the two effects is always observed in simulations as well as in measurements. In order to take this into account, we simulated the change of the dose at the reference point in a cylinder with a radius of 1 cm and a height of 0.2 cm  $\left(\frac{D_w}{D_{w,B}}\right)$ . Later, the total change of dose inside the ionization chambers in the presence of a B-field  $\left(\frac{D_{ch}}{D_{ch,B}}\right)$  was divided by the relative change of dose caused by the lateral and depth shift of the dose profile to calculate the actual correction factor  $k_B$  (O'Brien 2016):

$$k_B = \frac{D_{ch}}{D_{ch,B}} \times \frac{D_{w,B}}{D_w}.$$

For the calculation of correction factors by Monte-Carlo simulation, reference points of all chambers were placed at a depth of 10 cm inside a  $30 \times 30 \times 20$  cm<sup>3</sup> water phantom. The source-detector distance was 143.5 cm for the Elekta Unity and 90 cm for the MRIdian. The photons striking the phantom were sampled from the 7 MV spectrum for the Elekta Unity simulation and from the 6 MV FFF full accelerator simulation for the MRIdian.

All errors reported are for a 95% confidence interval and were calculated based on the variance of the Monte Carlo simulation.

### Experimental validation of the simulation method

For experimental validation of the simulation results, measurements were performed in a water phantom using a 6 MV linear accelerator (Elekta Precise Treatment System, Elekta AB, Stockholm, Sweden) in combination with an electromagnet (Bruker ER07, Ettlingen, Germany). The PTW 30013 ionization chamber was mounted at a 10 cm water equivalent depth inside a  $21 \times 7 \times 21$  cm<sup>3</sup> water phantom. The phantom was placed between

the pole shoes of the magnet with a maximum magnetic flux density of 1.45 T at an SSD of 110 cm. The monitor chamber was calibrated in this setup and 100 MU were applied in the following measurements using a  $5 \times 10 \text{ cm}^2$  photon field.

The measurements were performed on three consecutive days. The phantom was permanently positioned between the pole shoes, but the ionization chamber was inserted and repositioned every day (i.e. for each measurement). The chamber orientations chosen— $\alpha = 90^\circ$  and  $\alpha = 270^\circ$ —were realized by switching the magnetic field direction.

The magnetic flux density was monitored using a Hall effect sensor that was placed directly on one of the pole shoes and was adjusted with an accuracy of  $\pm 1 \text{ mT}$ .

Errors (95% confidence interval) were calculated from the standard error of the mean and from an additional absolute uncertainty of  $\pm 0.3\%$  accounting for fluctuations observed in the signal of the linac monitor chamber.

For benchmarking our simulation method, this experimental setup including the PTW 30013 ionization chamber was modeled in EGSnrc. A flattening filter was added to the 6 MV full accelerator simulation to align it with the experimental conditions. This simulation setup was also used for an additional calculation that was aiming for reproducing previously published results for an ionization chamber of type NE2571 placed inside a PMMA phantom (Smit *et al* 2013).

In order to be able to directly compare the simulations with experimental results, the change of the detector signal  $\left(\frac{D_{\text{ch}}}{D_{\text{ch,B}}}\right)$  instead of the correction factor  $k_B$  was calculated, because this can be obtained directly by measurement without the need for additional calculations or theoretical assumptions regarding the lateral and depth shift of the dose profile.

## Results

The correction factors for the Elekta Unity MR-linac (7 MV) are given in table 2 for both chamber orientations. For this magnetic flux density, the highest correction was calculated for the plane-parallel Roos chamber, where the calculated dose increased by 7.9(2)%. The highest impact on the thimble-type chambers for the 1.5 T MR-linac system was calculated for the PTW 30013, where the simulated signal increased by 4.9(2)% for a perpendicular orientation. In a parallel orientation, only small corrections were found for thimble-type chambers, where the change of signal never surpassed 0.8(2)% (PTW 30015).

Table 2 also shows correction factors for the ViewRay 6 MV system. While the correction factors are similar for thimble-type ionization chambers, there are some differences for the Roos and NACP-02 plane-parallel chambers, where the response is influenced less at this magnetic flux density.

In figure 2, the influence of the magnetic field on the detector response is shown for magnetic flux densities ranging from 0 to 2.5 T.

Magnetic flux densities higher than 2 T can result in an inverse effect in which the response of the ionization chamber decreases instead of increasing. This effect was most dominant for the PTW 30015 in perpendicular orientation, where the scored dose decreased by 3.3(1)% at 2.5 T.

Overall, the maximum effect of a magnetic field on radiation dose measurements with ionization chambers was observed at a magnetic flux density of approximately 1 T. For higher and lower magnetic flux densities, the effect decreases similarly. All simulated thimble-type chambers showed a similar change in response, while there were larger differences for plane-parallel chambers.

The results of the benchmark experiment are presented in figure 3. In this experiment, the highest absolute standard error of the mean was  $\pm 0.34\%$  at 1.425 T for  $\alpha = 90^\circ$ . By comparison, the lowest absolute standard error of the mean was calculated for the same orientation, but at 0.875 T, where it was  $\pm 0.05\%$ .

For direct comparison of the simulation results with the benchmark experiment, the root-mean-square deviation (RMSD) between the measurement and the simulation was calculated. Overall, a good agreement between the measurement and the simulation was observed, as illustrated by the total RMSD of 0.44%.

## Discussion

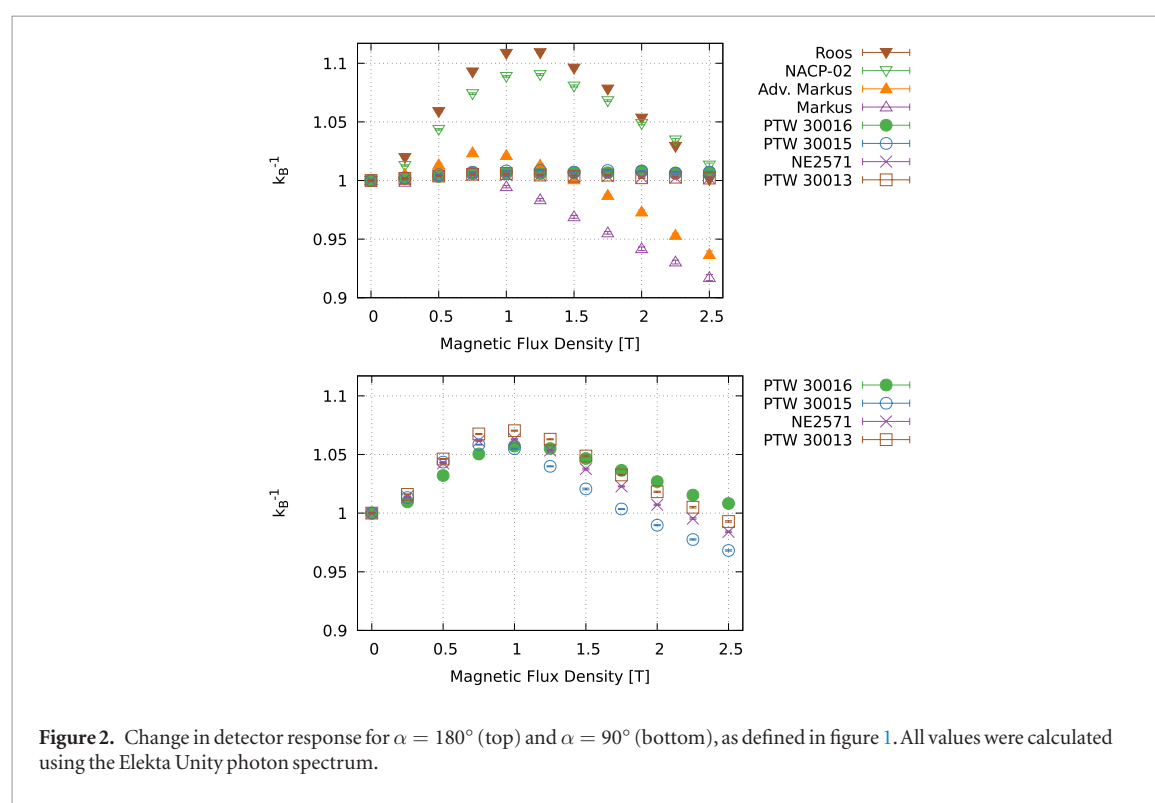
In the study presented in this paper, a systematic MC simulation of correction factors for ionization chambers used for reference dosimetry was performed in a representative experimental setting for a variety of chambers and a wide range of magnetic flux densities.

We utilized the Monte Carlo package EGSnrc because it has a long history of optimization for ionization chamber simulations (Rogers 2006) and because it is considered to be a kind of ‘gold standard’ in medical physics.



**Table 2.** Correction factors  $k_B$  for 0.35 T (6 MV FFF accelerator model) and 1.5 T (tabulated spectrum of Elekta Unity).

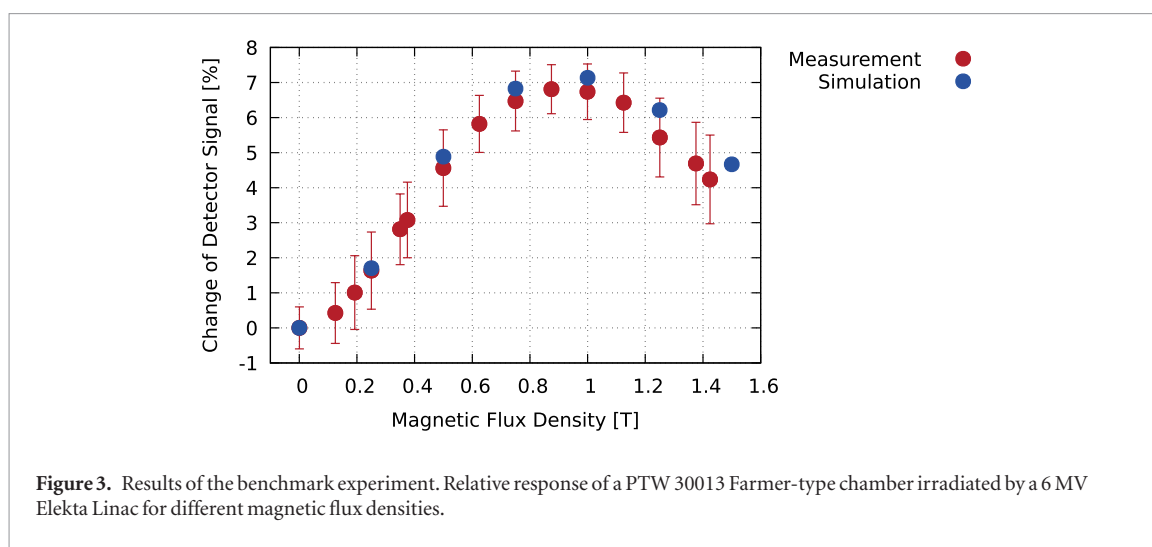
	Orientation $\alpha$	0.35 T (6 MV)	1.5 T (7 MV)
Roos	—	0.9689(10)	0.9272(12)
NACP-02	—	0.9765(13)	0.9372(14)
Adv. Markus	—	0.9903(14)	0.9720(15)
Markus	—	0.9920(14)	0.9809(15)
PTW30016	180°	0.9977(18)	0.9931(17)
PTW30015	180°	0.9980(14)	0.9929(16)
NE2571	180°	0.9995(12)	0.9963(16)
PTW30013	180°	0.9976(16)	0.9963(16)
PTW30016	90°	0.9770(18)	0.9554(14)
PTW30015	90°	0.9694(14)	0.9798(14)
NE2571	90°	0.9700(12)	0.9638(14)
PTW30013	90°	0.9684(16)	0.9535(14)



We also included plane parallel ionization chambers because, in the future, they may become suitable for reference dosimetry, as seen in DIN 6800-2 (Deutsches Institut für Normung 2008).

When thimble-type chambers were oriented in such a way that they were perpendicular to the magnetic field, they showed a change in response comparable to that of plane-parallel chambers. By contrast, only a small impact of the magnetic field was observed when the magnetic field was parallel to the chamber's axis.

At a magnetic flux density of approximately 1 T, the maximum effect of the magnetic field on the response of all the ionization chamber types investigated was observed. The peak of this effect at 1 T might potentially be explained by the trajectories of the secondary electrons. We hypothesize that, at this magnetic flux density, the trajectories may be bent to form a path that aligns with the dilatation of the sensitive volume; thus, for this situation, the probability of presence for an electron is greatest inside the sensitive volume. Hence, the maximum deposited dose is reached at this magnetic flux density as well. For higher magnetic flux densities, the trajectories are bent even more and the secondary electrons leave the chamber again, thus leading to a decrease in the deposited dose. This effect has only a minor influence on thimble-type chambers in parallel orientations, as the



broadening of the sensitive volume does not match the direction in which the electrons are bent. These effects have been illustrated by Meijnsing *et al* (2009).

Our simulations do not include any modification of chamber models to account for recently proposed dead volume effects (Spindeldreier *et al* 2017), but correction factors are presented for a setup where these effects are negligible. This assumption is confirmed by the calculated results.

Our simulated Elekta 7 MV correction factors for the PTW30013 and NE2571 ionization chambers are comparable to published values (O'Brien 2016). For parallel orientations, the results match in a 3-sigma error interval. There are differences for the orthogonal orientation, where we calculated corrections that differ by 1% and 2.5% for the NE 2571 and the PTW 30013 Farmer ionization chambers from the values given by O'Brien *et al* (2016).

Our simulated correction factors for the PTW 30013 in an Elekta Unity setup are very close to recently published results (Spindeldreier *et al* 2017), despite we used a MR-linac spectrum instead of an 6 MV spectrum as well as we did not adjust for any dead volume effects.

Corrections given for the ViewRay System can also be compared for the PTW30013 with the results published by Spindeldreier *et al* (2017); and confirm these in a single error interval.

In the benchmark experiment, we observed considerable fluctuations between the day-to-day measurements, especially for high magnetic flux densities. Currently, the reason for this is unknown. For better benchmarking, more measurements must be considered.

Within the estimated confidence intervals, the simulations fit the results of the benchmark experiment, but differences appear with increasing magnetic flux density. This may be caused by a small misalignment of the magnetic field axis and the ionization chamber axis. It has been shown that a tilt of the magnetic field by only  $3^\circ$  can decrease the measured dose by roughly 1% at 1.5 T, while the influence is negligible for magnetic flux densities below 0.6 T (Malkov and Rogers 2016).

In view of this, MR-linac systems that apply strong magnetic fields must ensure a highly accurate adjustment of the magnetic field axis and the beam direction.

At 1 T, the discrepancy is most likely also caused by dead volume effects that are prominent for this magnetic flux density (Malkov and Rogers 2017, Spindeldreier *et al* 2017).

We considered magnetic flux densities up to 2.5 T in order to provide input for future development of new generations of MR-linacs, where higher magnetic flux densities strengths may be relevant.

In this context, the results show that lower magnetic flux densities are not equivalent to a lower impact on ionization chambers. This is because the effect of the magnetic field on ionization chamber readings is at its maximum at approximately 1 T and decreases for both lower and higher magnetic flux densities.

In addition to the results presented here, we also simulated the setup used by Smit *et al* (2013) and were able to corroborate their correction factor of 0.953(10) for an ionization chamber of type NE2571 placed inside a PMMA phantom with our simulation experiment (PMMA,  $\alpha = 270^\circ$ ), resulting in a correction factor of 0.9529(26).

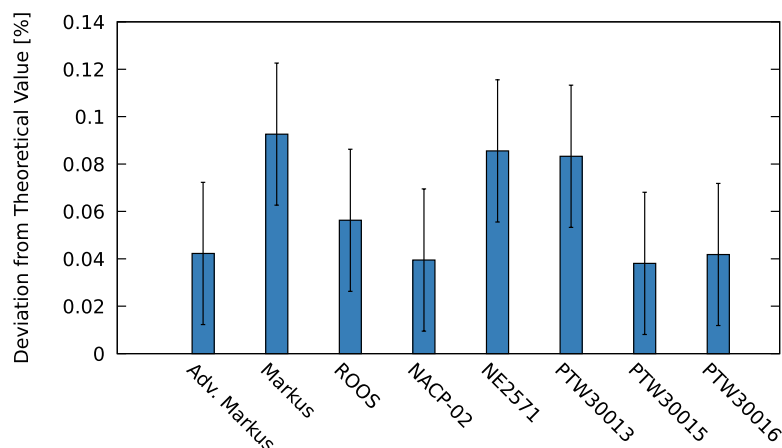


**Figure 4.** Results of the Fano cavity tests for all simulated ionization chamber geometries. For each ionization chamber, the mean dose scored in the sensitive volume under Fano conditions was compared to the corresponding theoretical value.

## Conclusion

EGSnrc Monte Carlo simulations based on the new, enhanced algorithm for electron transport in EEMF confirm previous results for ionization chamber corrections in external magnetic fields. Correction factors for eight chambers were simulated for current MR-linac systems, and can thus now be used for reference dosimetry and further validation.

## Acknowledgments

We acknowledge the support of Markus Meier and Markus Schrader (PTB, Braunschweig, Germany), who greatly assisted in the benchmark experiment. We thank Jörg Wulff for providing ionization-chamber geometries and material information collected for earlier publications. Also, we thank Katharina Spindeldreier (DKFZ, Heidelberg, Germany) as well as David Shipley (NPL, Teddington, United Kingdom) for giving helpful input on the matter of Fano cavity tests. Furthermore, we acknowledge support from the state of Baden–Württemberg through bwHPC and from the German Research Foundation (DFG) through grant no INST 39/963-1 FUGG. This work was partially funded by EURAMET through EMPIR grant 15HLT08 MRgRT.

## Appendix

### Fano cavity test

The implementation of complex ionization chamber geometries in EGSnrc can lead to errors resulting from faulty geometry definitions. A deficient geometry definition may result in inaccurate particle transport across geometry borders; a Fano cavity test is an adequate tool for verification of the implementation of geometries. The Fano cavity test was adapted as it is presented in previous publications (Sempau and Andreo 2006, de Pooter *et al* 2015, Malkov and Rogers 2016). All material cross sections were changed to these of water. The volumetric mass density inside the sensitive volume was set to a value that was a thousand times less than the volumetric mass density that was used for other parts of the simulation geometry. For Fano test simulations the ionization chambers' geometries were embedded in a  $10 \times 10 \times 10 \text{ cm}^3$  water phantom. Photon transport was disabled and electrons were sampled isotropic, uniform per unit mass throughout the whole simulation geometry with an initial energy of 1.25 MeV. A detailed description for the calculation of a theoretical value for the absorbed dose in the sensitive volume for this scenario can be found in literature (Malkov and Rogers 2016). The mean doses were scored in the sensitive volumes of all ionization chambers and compared to the corresponding theoretical values. All ionization chamber geometries passed this test with a deviation of less than 0.1% from the theoretical value, the results are presented in figure 4.

## References

- Ahmad S B, Sarfehnia A, Paudel M R, Kim A, Hissoiny S, Sahgal A and Keller B 2016 Evaluation of a commercial MRI Linac based Monte Carlo dose calculation algorithm with GEANT4 *Med. Phys.* **43** 894–907
- Andreo P, Burns D T, Hohlfield K, Huq M S, Kanai T, Laitano F, Smyth V and Vynckier S 2006 *Absorbed Dose Determination in External Beam Radiotherapy: An International Code of Practice for Dosimetry based on Standards of Absorbed Dose to Water* IAEA TRS 398
- de Pooter J A, de Prez L A and Bouchard H 2015 Application of an adapted Fano cavity test for Monte Carlo simulations in the presence of B-fields *Phys. Med. Biol.* **60** 9313–27
- Dempsey J, Dionne B, Fitzsimmons J, Haghigat A, Li J, Low D, Mutic S, Palta J, Romeijn H and Sjoden G 2006 WE-E-Vala-06: a real-time MRI guided external beam radiotherapy delivery system *Med. Phys.* **33** 2254
- Deutsches Institut für Normung 2008 Dosismessverfahren nach der sondenmethode für photonen-und elektronenstrahlung—teil 2: dosimetrie hochenergetischer photonen-und elektronenstrahlung mit ionisationskammern *DIN 6800-2, 2008-03*
- Fallone B G 2014 The rotating biplanar linac-magnetic resonance imaging system *Semin. Radiat. Oncol.* **24** 200–2
- Kawrakow I, Mainegra-Hing E, Rogers D W O, Tessier F and Walters B R B 2017 The EGSnrc code system: Monte Carlo simulation of electron and photon transport *NRCC Report PIRS-701 Technical Report* National Research Council, Canada
- Keall P J, Barton M and Crozier S 2014 The Australian magnetic resonance imaging-linac program *Semin. Radiat. Oncol.* **24** 203–6
- Malkov V N and Rogers D W O 2016 Charged particle transport in magnetic fields in EGSnrc *Med. Phys.* **43** 4447–58
- Malkov V N and Rogers D W O 2017 Sensitive volume effects on Monte Carlo calculated ion chamber response in magnetic fields *Med. Phys.* **44** 4854–58
- McPartlin A J et al 2016 MRI-guided prostate adaptive radiotherapy—a systematic review *Radiother. Oncol.* **119** 371–80
- Meijsing I, Raaymakers B W, Raaijmakers A J E, Kok J G M, Hogeweg L, Liu B and Lagendijk J J W 2009 Dosimetry for the MRI accelerator: the impact of a magnetic field on the response of a Farmer NE2571 ionization chamber *Phys. Med. Biol.* **54** 2993–3002
- O'Brien D J, Roberts D A, Ibbott G S and Sawakuchi G O 2016 Reference dosimetry in magnetic fields: formalism and ionization chamber correction factors *Med. Phys.* **43** 4915–27
- Raaijmakers A J E, Raaymakers B W and Lagendijk J J W 2005 Integrating a MRI scanner with a 6 MV radiotherapy accelerator: dose increase at tissue-air interfaces in a lateral magnetic field due to returning electrons *Phys. Med. Biol.* **50** 1363–76
- Raaymakers B W et al 2009 Integrating a 1.5 T MRI scanner with a 6 MV accelerator: proof of concept *Phys. Med. Biol.* **54** 229–37
- Reynolds M, Fallone B G and Rathee S 2013 Dose response of selected ion chambers in applied homogeneous transverse and longitudinal magnetic fields *Med. Phys.* **40** 42102
- Rogers D W O 2006 Fifty years of Monte Carlo simulations for medical physics *Phys. Med. Biol.* **51** 287–301
- Sanderson B, McWilliam A, Faivre-Finn C, Kirkby N F, Jena R, Mee T and Choudhury A 2017 Economic viability of MR-linac research using the Malthus programme to predict the recruitment of patients to MR-linac research trials in prostate and lung cancer *Radiother. Oncol.* **122** 159–62
- Sempau J and Andreo P 2006 Configuration of the electron transport algorithm of PENELOPE to simulate ion chambers *Phys. Med. Biol.* **51** 3533–48
- Smit K, van Asselen B, Kok J G M, Aalbers A H L, Lagendijk J J W and Raaymakers B W 2013 Towards reference dosimetry for the MR-linac: magnetic field correction of the ionization chamber reading *Phys. Med. Biol.* **58** 5945–57
- Spindeldreier C K, Schrenk O, Bakenecker A, Kawrakow I, Burigo L, Karger C P, Greulich S and Pfaffenberger A 2017 Radiation dosimetry in magnetic fields with Farmer-type ionization chambers: determination of magnetic field correction factors for different magnetic field strengths and field orientations *Phys. Med. Biol.* **62** 6708–28
- Tillner F et al 2016 Precise image-guided irradiation of small animals: a flexible non-profit platform *Phys. Med. Biol.* **61** 3084–108
- Tonkopi E, McEwen M R, Walters B R B and Kawrakow I 2005 Influence of ion chamber response on in-air profile measurements in megavoltage photon beams *Med. Phys.* **32** 2918–27
- Ubrich F, Wulff J, Kranzer R and Zink K 2008 Thimble ionization chambers in medium-energy x-ray beams and the role of constructive details of the central electrode: Monte Carlo simulations and measurements *Phys. Med. Biol.* **53** 4893–906
- Wulff J, Heverhagen J T and Zink K 2008a Monte-Carlo-based perturbation and beam quality correction factors for thimble ionization chambers in high-energy photon beams *Phys. Med. Biol.* **53** 2823–36
- Wulff J, Zink K and Kawrakow I 2008b Efficiency improvements for ion chamber calculations in high energy photon beams *Med. Phys.* **35** 1328–36
- Zink K and Wulff J 2008 Monte Carlo calculations of beam quality correction factors kQ for electron dosimetry with a parallel-plate roos chamber *Phys. Med. Biol.* **53** 1595–607

## OPEN ACCESS

## PAPER

RECEIVED  
20 March 2019REVISED  
3 June 2019ACCEPTED FOR PUBLICATION  
10 June 2019PUBLISHED  
4 July 2019

Original content from this work may be used under the terms of the [Creative Commons Attribution 3.0 licence](https://creativecommons.org/licenses/by/3.0/).

Any further distribution of this work must maintain attribution to the author(s) and the title of the work, journal citation and DOI.



# A finite element method for the determination of the relative response of ionization chambers in MR-linacs: simulation and experimental validation up to 1.5 T

Stefan Pojtinger<sup>1,3,4</sup>, Ralf-Peter Kapsch<sup>1</sup>, Oliver Steffen Dohm<sup>2</sup> and Daniela Thorwarth<sup>3</sup><sup>1</sup> Physikalisch-Technische Bundesanstalt, Braunschweig, Germany<sup>2</sup> University Hospital Tübingen, Medical Physics, Tübingen, Germany<sup>3</sup> University Hospital Tübingen, Biomedical Physics, Tübingen, Germany<sup>4</sup> Author to whom correspondence should be addressed.**E-mail:** [Stefan.Pojtinger@ptb.de](mailto:Stefan.Pojtinger@ptb.de), [Ralf-Peter.Kapsch@ptb.de](mailto:Ralf-Peter.Kapsch@ptb.de), [Oliver.Dohm@med.uni-tuebingen.de](mailto:Oliver.Dohm@med.uni-tuebingen.de) and [Daniela.Thorwarth@med.uni-tuebingen.de](mailto:Daniela.Thorwarth@med.uni-tuebingen.de)**Keywords:** Monte Carlo, dosimetry, MR-linac, finite element simulation, EGSnrc, COMSOL, ionization chamber

## Abstract

In magnetic resonance (MR) guided radiotherapy, the magnetic field-dependent change in the dose response of ionization chambers is typically included by means of a correction factor  $k_{\vec{B},M,Q}$ . This factor can be determined experimentally or calculated by means of Monte Carlo (MC) simulations. To date, a small number of experimental values for  $k_{\vec{B},M,Q}$  at magnetic flux densities above 1.2 T have been available to benchmark these simulations. Furthermore, MC simulations of the dose response of ionization chambers in magnetic fields (where such simulations are based on manufacturer blueprints) have been shown to converge with results that deviate considerably from experimental values for orientations where the magnetic field is perpendicular to the axis of the ionization chamber and the influence of the magnetic field is largest.

In this work,  $k_{\vec{B},M,Q}$  was simulated for a PTW 30013 Farmer ionization chamber using an approach based on finite element simulations. First, the electrical field inside the ionization chamber was simulated using finite element methods. The collecting volume of the ionization was not defined in terms of the physical dimensions of the detector but in terms of the simulated electrical field lines inside the chamber. Then, an MC simulation of the dose response of a Farmer type chamber (PTW 30013) was performed using EGSnrc with a dedicated package to consider the effect of the magnetic field. In the second part,  $k_{\vec{B},M,Q}$  was determined experimentally for two different PTW 30013 ionization chambers for a range of magnetic flux densities between  $B = 0$  and 1.5 T, covering the range of commercially available MR-linacs.

In the perpendicular orientation, the maximum difference between the simulated values for  $k_{\vec{B},M,Q}$  and the experimental values for  $k_{\vec{B},M,Q}$  was 0.31 (30)% and the minimum difference was 0.02 (24)%. For the PTW 30013 ionization chambers, the experimental values for  $k_{\vec{B},M,Q}$  were 0.9679 (1) and 0.9681 (1) for a magnetic flux density of 1.5 T. The value resulting from the simulation was 0.967 (3).

The comparison of the correction factors simulated using this new approach with the experimental values determined in this study shows excellent agreement for all magnetic flux densities up to 1.5 T. Integrating the explicit simulation of the collection volume inside the ionization chambers into the MC simulation model significantly improves simulations of the chamber response in magnetic fields. The results presented suggest that intra-type variations for  $k_{\vec{B},M,Q}$  may be neglectable for ionization chambers of the PTW 30013 type.

## Introduction

Recently developed commercial MR-linac devices (Raaymakers *et al* 2009, Mutic and Dempsey 2014) are now available for research purposes and for patient treatment at many institutions. Protocols for reference dosimetry have been developed for these devices since their introduction. The key point about dosimetry in MR-linacs is the change of response of the ionization chambers due to the influence of the magnetic field (Meijsing *et al* 2009) existing permanently in MR-linacs with magnetic flux density up to 1.5 T. Therefore, the change in the response caused by the magnetic field must be corrected; several formalisms have been proposed for this purpose (O'Brien *et al* 2016, van Asselen *et al* 2018). Several publications have addressed this problem for a wide range of detectors using Monte Carlo (MC) simulations (Meijsing *et al* 2009, Malkov and Rogers 2016, O'Brien *et al* 2016, Spindeldreier *et al* 2017). However, significant differences were found between calculated and measured detector responses in magnetic fields, especially for magnetic flux densities above 1 T. Van Asselen *et al* (2018) reviewed simulation results and compared it to experimental values; for a standard Farmer type chamber in specific orientations a discrepancy of more than 1% was found.

Malkov and Rogers (2017) and Spindeldreier *et al* (2017) have hypothesized that the discrepancy between the experimental results and the MC results can be explained as being due to regions of reduced local response near the guard ring of the detector; this is not considered in conventional MC simulations. This leads back to the question of whether the collecting volume of an ionization chamber (i.e. the volume from which ions are collected) coincides with the sensitive volume defined by the chamber geometry. Ross (2009) describes an approach wherein the collecting volume is different from the geometrically defined sensitive volume due to inhomogeneities in the electric field inside the ionization chamber. Ross suggests that the collecting volume can be calculated by running finite element (FEM) simulations of the electric field inside the ionization chamber and reducing the sensitive volume by the volume where the electric field lines that emerge from the ionization chamber's wall reach the guard ring instead of the electrode. This approach was recently implemented by Looe *et al* (2018) and led to an agreement between the measurements and the simulations of about 0.5% for a small volume ionization chamber that was positioned parallel to the radiation beam and perpendicular to the magnetic field up to 1.4 T. However, it has been shown that, for this orientation, the influence of the magnetic field is small (Looe *et al* 2018); in addition, the magnetic flux density inside current MR-linacs surpasses 1.4 T (Raaymakers *et al* 2009).

This work aims to improve the current situation by presenting new experimental results for a conventional ionization chamber up to a magnetic flux density of 1.5 T; these results are based on measurements in a well-defined experimental setup. The usage of FEM-based adjustments of MC detector simulations in magnetic fields is tested in the orientation where the ionization chamber is perpendicular to both the magnetic field and the beam direction and therefore the electron trajectories are deflected towards the stem or tip of the ionization chamber by means of the Lorentz force (figure 1). This orientation has been shown to be problematic in previous publications (Malkov and Rogers 2017, Spindeldreier *et al* 2017, van Asselen *et al* 2018) and differs from that tested in the previous publication by Looe *et al* (2018).

For the MC detector simulation, we utilized the EGSnrc software package. EGSnrc includes dedicated user-codes for the simulation of the response of ionization chambers and was optimized for this purpose for many years (Rogers 2006).

It has been found previously that the correction to the response of the chamber is substantially larger when the chamber axis is oriented perpendicular to the magnetic field compared to the case of a parallel orientation (van Asselen *et al* 2018). A parallel orientation is therefore beneficial for clinical practice and often preferred. Nevertheless, it is important to find the reason for the discrepancy between Monte Carlo calculations and experiments in perpendicular orientation, to guarantee reliable Monte Carlo results for ionization chamber simulations in magnetic fields in general.

## Material and methods

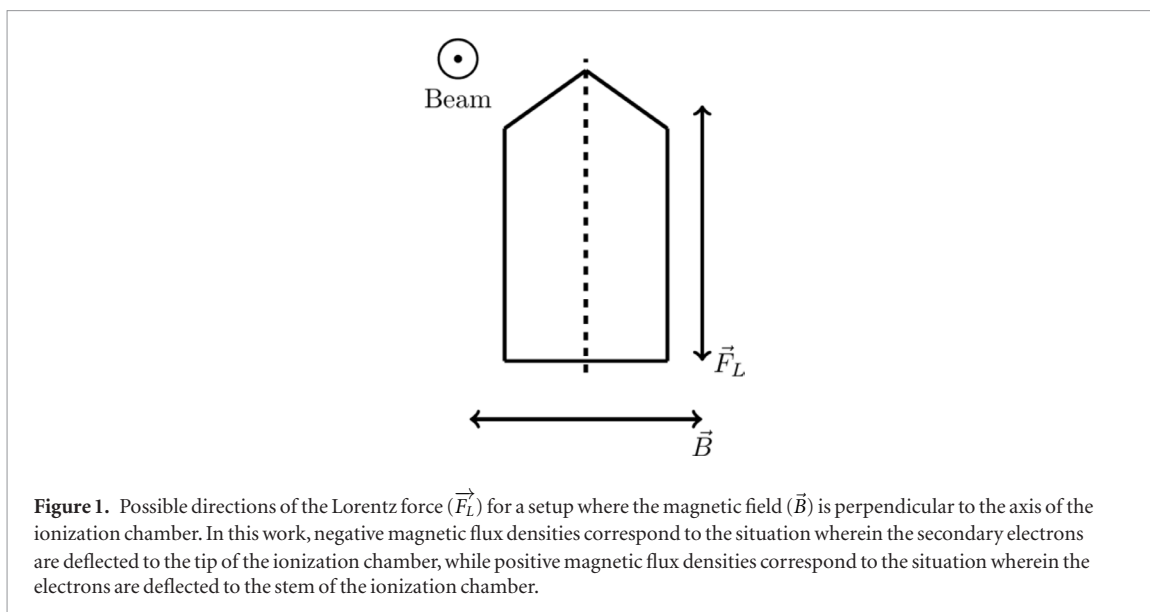
### Formalism

In this paper, we follow the notation of van Asselen *et al* (2018). In the formalism below, the magnetic field correction factor  $k_{\vec{B},Q}$  is defined as:

$$k_{\vec{B},Q} = c_{\vec{B}} k_{\vec{B},M,Q}. \quad (1)$$

Here,  $c_{\vec{B}}$  represents the ratio of absorbed doses to water at the point of measurement with and without a magnetic field and  $k_{\vec{B},M,Q}$  is the ratio of detector responses without and with a magnetic flux density  $\vec{B}$ .

All experimental and simulated results are presented as  $k_{\vec{B},M,Q}$ , since this is the most direct way to compare simulations and experiments.



### Orientation

For simulations and experiments in this work, the Farmer type ionization chambers were set up in such a way that all pairwise orientations between the magnetic field vector, the ionization chamber axis and the beam direction were perpendicular. The secondary electrons are deflected by the Lorentz Force ( $\vec{F}_L$ ) either to the ionization chamber's tip or its stem (figure 1).

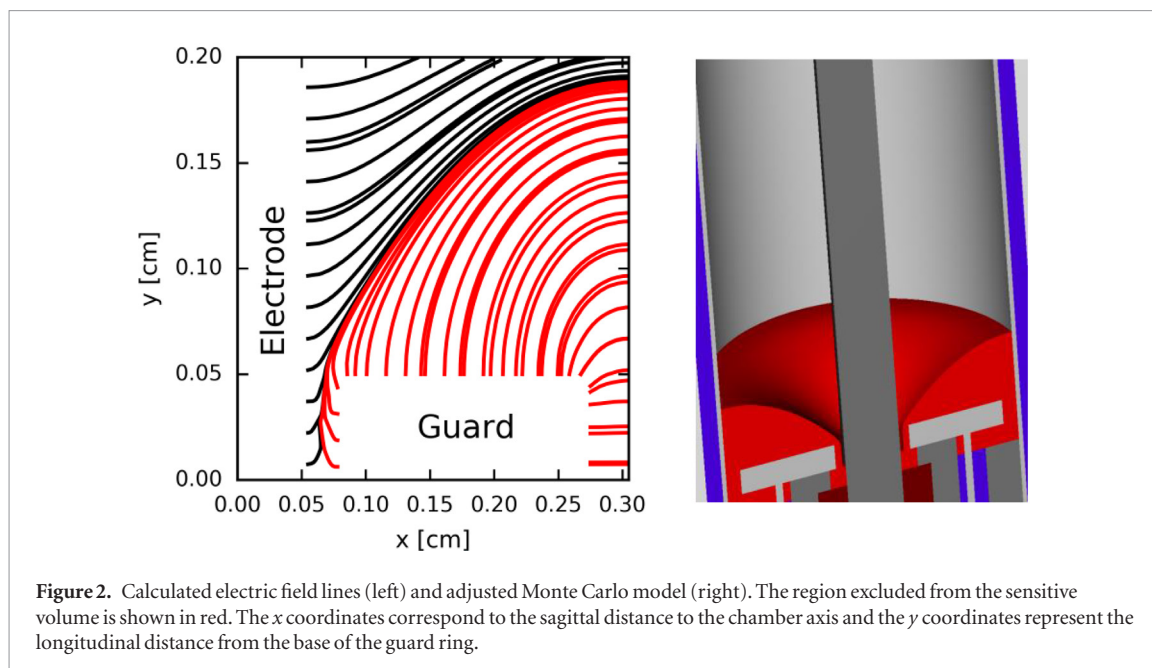
In the following, all negative magnetic flux densities correspond to a situation in which the electrons are deflected to the tip of the ionization chamber; for a positive sign of the magnetic flux density, the electrons are deflected towards the stem of the ionization chamber.

### Experiments

All experiments were carried out using the Metrological Electron Accelerator Facility (MELAF) (Schüller *et al* 2019) at PTB, the national metrology institute of Germany, in Braunschweig. A large electromagnet (Bruker ER073W) with a 6 cm gap between its pole shoes was placed in front of an Elekta Precise accelerator (151605). A  $6 \times 20 \times 20 \text{ cm}^3$  water phantom (constructed by PTB) was positioned between the pole shoes of the magnet at a source-to-surface distance (SSD) of 110 cm. Ionization chambers were mounted within this phantom at a well-defined reference point and irradiated by a horizontal photon beam with a nominal accelerating voltage of 6 mV, which was collimated to  $4 \times 10 \text{ cm}^2$  at the isocenter (source to axis distance 100 cm) to avoid backscattering effects from the pole shoes. Each measurement was repeated three times for each detector (S/N 006762 and 009193) on different days, including a full repositioning in the water phantom. A chamber voltage of 250 V was applied to the Farmer ionization chambers.

For the measurement of the relative response under different magnetic flux densities, a transmission monitor chamber was mounted onto the shadow tray of the accelerator head (Kapsch and Krauss 2009). The distance between the source and the transmission monitor chamber was 67.5 cm. Measurements had shown that the magnetic flux density of the magnetic fringe field at the position of the transmission monitor chamber does not surpass 1 mT and is therefore assumed to have a neglectable influence on the response of the transmission monitor chamber. This was checked by positioning an ionization chamber 3 m behind the electromagnet and comparing the signal of this ionization chamber (which is unaffected by the fringe field) with the signal of the transmission monitor chamber both with and without the magnetic field. No significant influence of the fringe field on the response of the monitor chamber was found in this measurement.

Ionization chambers under test were preirradiated with at least 1000 MU before the start of each measurement, while the stability of the ratio of the chamber signal to the monitor chamber was monitored online to avoid any settling effects (Ken Shortt *et al* 2005). After this, the beam was maintained in an active state, and the electrical charges collected over a 150 s period by the monitor chamber and the ionization chamber under test were measured simultaneously using Keithley 6517 (Keithley Instruments, Solon, USA) electrometers. Then, the magnetic flux density was altered remotely from the control room while the beam was maintained in an active state. This included an adjustment of the accelerator's steering magnets to compensate for the small deflection of the electron beam inside the accelerator due to the magnetic fringe field. The magnetic flux density was measured throughout the entire experiment by a hall sensor placed between the electromagnet pole shoes (DTM 151 Digital Teslameter, Group 3 Technology, Auckland, New Zealand). The measurements were repeated in steps of 0.15 T



for both possible magnetic field directions and for an additional point at 0.35 T, which corresponds to the magnetic flux density of the ViewRay MRIdian MR-linac (ViewRay Technologies, Cleveland, USA). Later, the relative response was calculated as the ratio of the charges collected by the detector to the charge collected by the monitor chamber, normalized to the corresponding ratio at 0 T. Given uncertainties include only the Type A uncertainty component (JCGM 2008).

### Simulations

For the simulation of the electric field inside a PTW 30013 ionization chamber, COMSOL Multiphysics version 5.3, a finite element simulation program, was used. The ionization chamber was modeled in COMSOL according to the manufacturer's engineering drawings; Maxwell equations were solved for a ground potential on the guard ring and the electrode and for 250 V on the graphited wall of the ionization chamber (figure 2). A script was written to extract the last field line leading from the chamber wall to the guard instead of to the central electrode, and to calculate a dead volume of no response based on this line. This volume was used in combination with the EGSnrc Monte Carlo framework (Kawrakow *et al* 2013). A detailed model of the ionization chamber was created for EGSnrc, including the dead volume calculated beforehand by means of finite element simulations (figure 2). The cross sections and physics parameters in EGSnrc were chosen in accordance with ICRU90 (ICRU 2014) and earlier simulation studies (Pojtinger *et al* 2018). This was achieved by utilizing the Mcdf-xcom photon cross sections and enabling atomic relaxation. The energy cut-off was set to 0.521 MeV for electrons and 0.01 MeV for photons. For the simulation of the external magnetic field, the most recent magnetic field macro (Malkov and Rogers 2016) was used. The `egs_chamber` usercode (Wulff *et al* 2008) was utilized for all simulations. This usercode was developed especially for ion chamber simulations and provides advanced variance reduction methods as intermediate phase space-storage and photon cross section enhancement (XCSE). XCSE was activated as suggested in Wulff *et al* (2008). To this end, a 1 cm cylindrical water shell was modeled around the ionization chamber; for each medium inside the shell cross section enhancement was activated with an enhancement factor of 64. For simulation of the photon beam, a full accelerator head model was created in BEAMnrc and coupled to the `egs_chamber` usercode. The uncertainty given below for simulation results is the variance of the Monte Carlo simulation using a coverage factor of  $k = 2$  to approximate an 95% coverage interval (JCGM 2008).

### Results

The experimental results can be found in figure 3 and table 1. The experimental standard deviation  $s$  was calculated based on the three measurements taken for each detector. The maximum experimental standard deviation over all magnetic flux densities  $s_{\max}$  is shown in table 1.

The PTW 30013 Farmer chamber showed an increased response when the electrons were deflected to the tip ( $B < 0$  T) as well as when the electrons were deflected to the stem ( $B > 0$  T) of the ionization chamber; however, when the magnetic flux density was increased to more than 1 T, the response decreased. When the experimental results for the two different chambers were compared, the results for the relative response in magnetic fields



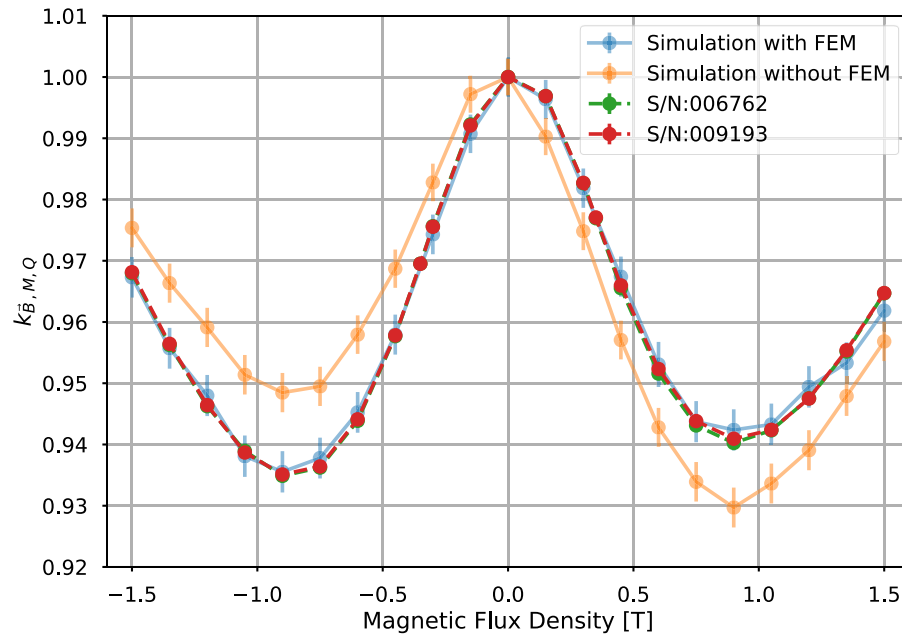


**Figure 3.** Comparison of the experimental values of  $k_{\bar{B},M,Q}$  for a PTW 30013 Farmer ionization chamber and the FEM-adjusted Monte Carlo simulation. For comparison, the figure also includes the results of a simulation without the FEM adjustments.

**Table 1.** Experimental values for  $k_{\bar{B},M,Q}$ .

	$k_{\bar{B},M,Q}$				$s_{\max}$ [%]
	-1.5 T	-0.35 T	0.35 T	1.5 T	
PTW 30013—006762	0.9679(1)	0.9695(1)	0.9769(1)	0.9647(1)	0.11
PTW 30013—009193	0.9681(1)	0.9695(1)	0.9771(1)	0.9647(1)	0.16

matched within 0.04%. The small differences also highlight the excellent reproducibility of the experimental method.

The FEM calculations resulted in a dead volume of  $0.04 \text{ cm}^3$ , which equals 7% of the nominal sensitive volume. Figure 3 shows the experimental results obtained for the PTW 30013 ionization chamber compared to the results of the FEM-adjusted MC simulation, as well as the result of a simulation without FEM adjustments in which the sensitive volume coincides with the physical dimensions of the chamber cavity. To compare the results, the mean of the squared deviations between the values of  $k_{\bar{B},M,Q}$  resulting from the experimental measurements and the simulations was calculated. For the FEM-adjusted simulation, the mean squared deviation is 0.21 (34)%, while a value of 1.03(32)% was found for the simulation without FEM adjustments. The maximum difference between the simulation and the experiment is 0.31(30)% at  $B = 1.5 \text{ T}$  and the minimum difference is 0.02(24)% at  $B = -0.45 \text{ T}$ .

## Discussion

The introduction of FEM adjustments to the Monte Carlo simulations has significantly improved the consistency of the calculated values with the experimental results. For Farmer type ionization chambers in perpendicular orientations, the deviation between the simulated and experimentally obtained dose responses in magnetic fields was reduced to less than 0.31(30)% for all values of the magnetic flux density, which is a significant improvement over the results without FEM adjustments, where deviations range up to 1.44(32)% at  $B = 0.9 \text{ T}$ . The advantage of the approach presented here over previous publications (Malkov and Rogers 2017, Spindeldreier *et al* 2017) is that the adjustment of the collecting volume takes into account the actual form of the dead volume. Previous publications modeled the dead volume as cylinders with the radius of the geometrical volume of the ionization chamber and placed the dead volume near the guard. However, the actual geometry of the dead volume more closely resembles a torus and disappears near the collecting electrode. Because of these differences, the calculated volume of the dead volume in this manuscript cannot be compared directly to the volumes presented in previous publications (Malkov and Rogers 2017, Spindeldreier *et al* 2017).

Spindeldreier *et al* (2017) determined the sensitive volume in a semi-empirical way. MC simulations they performed included cylindrically shaped dead volumes of different sizes. The size of the actual dead volume was

**Table 2.** Comparison of the values for  $k_{\vec{B},M,Q}$  presented in this work and the value from a Elekta Unity setup published by van Asselen *et al* (2018). Note that the uncertainty of the value of van Asselen *et al* was multiplied by a value of 2 to make it comparable to the uncertainties given in this work that are presented for  $k = 2$ .

	This work			van Asselen <i>et al</i>
	PTW30013 S/N 6762	PTW 30013 S/N 9193	Monte Carlo	
$k_{\vec{B},M,Q}(B = -1.5 \text{ T})$	0.9679(1)	0.9681(1)	0.967(3)	0.967(4)

adjusted to bring the simulation results in accordance with experimental results up to 1.1 T. This approach simplified the geometrical shape of the dead volume. In addition, calculating correction factors for 1.5 T based on this method is an extrapolation, which may explain the discrepancies to experimental results.

Another advantage of the FEM-based method presented in this work is that the determination of the dead volume is independent of any measurement; MC calculations based on the method presented in this work can therefore be used to independently validate any measurement and vice versa.

This method may be further improved by implementing modelling of inhomogeneous electromagnetic fields to the Monte Carlo algorithm itself because, currently, the method assumes that one part of the volume has no response at all and another part has a fully collected charge without considering regions where the response is only reduced to a smaller value.

The results of this work agree within the uncertainties with the experimental data obtained in an Elekta Unity MR linac (van Asselen *et al* 2018). An overview of all values obtained for the PTW 30013 ionization chamber is given in table 2 together with the results of measurements performed using an Elekta Unity system published in van Asselen *et al* (2018). All the results match within the uncertainties given in table 2. This may seem surprising at first glance (the manufacturer describes the beam in the Elekta Unity MR linac as ‘7 MV FFF’), in the experimental setup presented in this work, all experiments were performed using a conventional linac with a flattening filter and a nominal acceleration voltage of 6 MV. Additional differences exist between the experimental setup in this work and the experimental setup in the work of van Asselen *et al* (2018) regarding the field size ( $4 \times 10 \text{ cm}^2$  instead of  $10 \times 10 \text{ cm}^2$ ) and the SSD (110 cm instead of 133.5 cm). This indicates that the change in the response of a given ionization chamber due to the influence of a magnetic field, and therefore the correction factor  $k_{\vec{B},M,Q}$ , is largely independent of these changes. To confirm this, further work is required.

The good agreement between the experimental results on the one hand and the low intra-type variability on the other allows for the possibility that a value for  $k_{\vec{B},M,Q}$  can be taken from literature for a PTW 30013 ionization chamber. However, this must be confirmed in future work that includes more than two ionization chambers.

Without FEM adjustments, the deflected electron trajectories lead to an increased response if the electrons are deflected to the stem of the ionization chamber ( $B > 0 \text{ T}$ ), compared to when the electrons are deflected to the tip of the ionization chamber ( $B < 0 \text{ T}$ ), as seen in the asymmetry of the green curve in figure 3. This is due to the fact that the secondary electrons are deflected to a partial volume (around the guard) that is larger than the partial volume they would have been directed to if deflected towards the tip. Therefore, they are less likely to leave the sensitive volume if they are deflected to the stem instead of the tip.

It may be surprising that a change of only 7% in the nominal sensitive volume results in a change in the influence of the magnetic field of more than 1%. The reason for this is that, if the secondary electrons are deflected to the stem of the ionization chamber by the magnetic field, a larger dose will be deployed into the area around the guard, even though this area is insensitive to dose scoring, thus canceling out most of the overall effect. Furthermore, the dead volume leads to an additional increase in the response when the electrons are deflected to the tip. This is because the dose given off by secondary electrons passing the dead volume is also neglected when no magnetic field is present. However, if the magnetic field directs these electrons from the dead volume towards the tip of the ionization chamber, these electrons can again give off a dose, thus increasing the response.

## Conclusion

This work shows that Monte Carlo simulations of Farmer type ionization chambers in magnetic fields converge with the experimental results for magnetic flux densities up to 1.5 T if the FEM adjustments to the sensitive volume presented here are applied. This is an improvement to previous publications (Malkov and Rogers 2016, O’Brien and Sawakuchi 2017, Spindeldreier *et al* 2017), thus allowing the conclusion to be drawn that FEM-based determination of the sensitive volume presented here drastically improves Monte Carlo simulations of ionization chamber responses in magnetic fields.

Experimental values for  $k_{\vec{B},M,Q}$  were determined for magnetic flux densities up to 1.5 T; these values can be used to define dosimetry protocols for MR-guided radiotherapy or in clinical routine dosimetry. Developers of Monte Carlo algorithms can use this data to develop or verify new Monte Carlo methods for this specific scenario.

## Acknowledgments

We acknowledge the technical support of Markus Meier, Markus Schrader and Larissa Meyer (PTB, Braunschweig, Germany), who greatly assisted the experimental work. We would like to thank Daniela Poppinga and Rafael Kranzer (PTW, Freiburg, Germany) for their constructive discussion and for providing us with detailed information on the detectors. Furthermore, we acknowledge the support provided by the state of Baden-Württemberg through bwHPC and by the German Research Foundation (DFG) through Grant No. INST 39/963-1 FUGG. This work was funded by EURAMET through EMPIR Grant No. 15HLT08 MRgRT.

## ORCID iDs

Stefan Pojtinger  <https://orcid.org/0000-0001-6397-4572>

## References

- ICRU 2014 *Key Data for Ionizing-Radiation Dosimetry: Measurement Standards and Applications (ICRU Report 90, Journal of the ICRU)* vol 14 (Oxford, UK: Oxford University Press) pp 1–118
- JCGM 100: 2008 2008 *Evaluation of Measurement Data: Guide to the Expression of Uncertainty in Measurement* (Sèvres: International Bureau of Weights and Measures) (<http://doi.org/10.1373/clinchem.2003.030528>)
- Kapsch R P and Krauss A 2009 On the performance of monitor chambers to measure the output of medical linear accelerators for high-precision dosimetric investigations *IFMBE Proc.* vol 25 pp 85–8 ([https://doi.org/10.1007/978-3-642-03474-9\\_25](https://doi.org/10.1007/978-3-642-03474-9_25))
- Kawrakow I, Mainegra-Hing E, Rogers D W O, Tessier F and Walters B R B 2013 The EGSnrc code system: Monte Carlo Simulation of electron and photon transport *NCR Report PIRS-701* National Research Council of Canada, Ottawa
- Ken Shortt F, Ross C and Seuntjens J 2005 Pre-irradiation effects on ionization chambers used in radiation therapy *Phys. Med. Biol.* **50** 121
- Looe H K, Delfs B, Poppinga D, Harder D and Poppe B 2018 2D convolution kernels of ionization chambers used for photon-beam dosimetry in magnetic fields: the advantage of small over large chamber dimensions *Phys. Med. Biol.* **63** 075013
- Malkov V N and Rogers D W O 2016 Charged particle transport in magnetic fields in EGSnrc *Med. Phys.* **43** 4447–58
- Malkov V N and Rogers D W O 2017 Sensitive volume effects on Monte Carlo calculated ion chamber response in magnetic fields *Med. Phys.* **44** 4854–8
- Meijsing I, Raaymakers B W, Raaijmakers A J E, Kok J G M, Hogeweg L, Liu B and Lagendijk J J W 2009 Dosimetry for the MRI accelerator: the impact of a magnetic field on the response of a Farmer NE2571 ionization chamber *Phys. Med. Biol.* **54** 2993–3002
- Mutic S and Dempsey J F 2014 The ViewRay system: magnetic resonance-guided and controlled radiotherapy *Semin. Radiat. Oncol.* **24** 196–9
- O'Brien D J, Roberts D A, Ibbott G S and Sawakuchi G O 2016 Reference dosimetry in magnetic fields: formalism and ionization chamber correction factors *Med. Phys.* **43** 4915–27
- O'Brien D J and Sawakuchi G O 2017 Monte Carlo study of the chamber-phantom air gap effect in a magnetic field *Med. Phys.* **44** 3830–8
- Pojtinger S, Dohm O S, Kapsch R-P and Thorwarth D 2018 Ionization chamber correction factors for MR-linacs *Phys. Med. Biol.* **63** 11NT03
- Raaymakers B W et al 2009 Integrating a 1.5 T MRI scanner with a 6 MV accelerator: proof of concept *Phys. Med. Biol.* **54** 229–37
- Rogers D W O 2006 Fifty years of Monte Carlo simulations for medical physics *Phys. Med. Biol.* **51** 287–301
- Ross C K 2009 Comments on 'Ionization chamber volume determination and quality assurance using micro-CT imaging' *Phys. Med. Biol.* **54** 23–7
- Schüller A, Pojtinger S, Meier M, Makowski C and Kapsch R P 2019 The Metrological Electron Accelerator Facility (MELAF) for research in dosimetry for radiotherapy *IFMBE Proc.* vol 68 pp 589–93 ([https://doi.org/10.1007/978-981-10-9023-3\\_109](https://doi.org/10.1007/978-981-10-9023-3_109))
- Spindeldreier C K, Schrenk O, Bakenecker A, Kawrakow I, Burigo L, Karger C P, Greilich S and Pfaffenberger A 2017 Radiation dosimetry in magnetic fields with Farmer-type ionization chambers: determination of magnetic field correction factors for different magnetic field strengths and field orientations *Phys. Med. Biol.* **62** 6708–28
- Van Asselen B, Woodings S J, Hackett S L, van Soest T L, Kok J G M, Raaymakers B W and Wolthaus J W H 2018 A formalism for reference dosimetry in photon beams in the presence of a magnetic field *Phys. Med. Biol.* **63** 125008
- Wulff J, Zink K and Kawrakow I 2008 Efficiency improvements for ion chamber calculations in high energy photon beams *Med. Phys.* **35** 1328–36

## OPEN ACCESS



## PAPER

# Chemical radiation dosimetry in magnetic fields: characterization of a Fricke-type chemical detector in 6 MV photon beams and magnetic fields up to 1.42 T

Maria A Trachsel<sup>1</sup>, Stefan Pajtinger<sup>2,3</sup>, Markus Meier<sup>2</sup>, Markus Schrader<sup>2</sup>, Ralf-Peter Kapsch<sup>2</sup> and Christian Kottler<sup>1</sup>

<sup>1</sup> Federal Office of Metrology METAS, Bern-Wabern, Switzerland

<sup>2</sup> Physikalisch-Technische Bundesanstalt, Braunschweig, Germany

<sup>3</sup> University Hospital Tübingen, Biomedical Physics, Tübingen, Germany

E-mail: [maria.trachsel@metas.ch](mailto:maria.trachsel@metas.ch)

**Keywords:** MR-guided radiotherapy, Fricke dosimetry, reference dosimetry, MR-linac, magnetic field, chemical dosimetry

RECEIVED  
10 November 2019

REVISED  
16 January 2020

ACCEPTED FOR PUBLICATION  
6 February 2020

PUBLISHED  
18 March 2020

Original content from this work may be used under the terms of the [Creative Commons Attribution 3.0 licence](https://creativecommons.org/licenses/by/4.0/).

Any further distribution of this work must maintain attribution to the author(s) and the title of the work, journal citation and DOI.



## Abstract

In magnetic resonance guided radiotherapy (MRgRT) radiation dose measurements need to be performed in the presence of a magnetic field. In this study, the influence of magnetic fields on the readings of a Fricke detector, a chemical dosimeter, have been investigated in 6 MV photon beams. This type of detector has been chosen, as the Federal Office of Metrology (METAS, Switzerland) has great experience with Fricke dosimetry and since it is not expected that this detector is greatly affected by the presence of a magnetic field.

Magnetic fields with field strengths between 0 T and 1.42 T were applied during the detector irradiation. In a  $5 \times 10 \text{ cm}^2$  irradiation field, the Fricke readings are affected less than 0.9% by the applied magnetic fields. Taking the altered dose distribution due to the magnetic field ( $c_B$ ) into account, the magnetic field correction factors ( $k_{B,Q}$ ) for the Fricke detector at 0.35 T and 1.42 T are determined to be 0.9948 and 0.9980, respectively. These small corrections hardly exceed the measurement uncertainties. Hence, we could prove that the Fricke detector is not significantly influenced by the presence of a magnetic field.

The Fricke detector was also tested for the feasibility of measuring output factors in the presence of magnetic fields. For irradiation field sizes larger than the detector ( $>2 \times 2 \text{ cm}^2$ ), comparable results were obtained as for other detectors. The output factors decrease when a magnetic field is applied. This effect is more pronounced for larger magnetic field strengths and smaller irradiation fields due to shifts of the depth dose curves and asymmetry of lateral dose profiles.

## 1. Introduction

In MR-guided radiotherapy (MRgRT) the magnetic resonance (MR)-imaging technique is combined with high-energy photon irradiation to improve the irradiation as the contours of tumors, organs and healthy tissue can be adapted on daily basis or even online and therefore exposure of healthy tissue can be reduced (Legendijk *et al* 2014, Schmidt and Payne 2015). The magnetic field changes the dose distribution since the Lorentz force deflects the path of the secondary electrons generated by the photon beam. This leads to shifts in the position of the maximum dose ( $d_{max}$ ) in depth dose curves, to an asymmetry in lateral dose profiles and at tissue-air boundaries an electron return effect (ERE) occurs (Raaijmakers *et al* 2004, Raaijmakers *et al* 2007, 2008, Agnew *et al* 2017, Looe *et al* 2017, O'Brien *et al* 2017, Richter *et al* 2017, Wegener *et al* 2019). As the magnetic field cannot easily be switched off, the measurement of the radiation dose needs to be performed in the presence of the magnetic field. Therefore, the response of the detector is affected by the magnetic field and it needs to be corrected. For ionization chamber type detectors, as commonly used in reference dosimetry, it was shown that appropriate correction can be achieved by introducing a chamber specific correction factor  $k_{B,Q}$ . This correction factor depends on the photon beam quality ( $Q$ ), the magnetic field strength ( $B$ ) and the mutual orientation of the

detector and the magnetic field strength (Meijsing *et al* 2009, Reynolds *et al* 2013, Smit *et al* 2013, Spindeldreier *et al* 2017, van Asselen *et al* 2018).

Van Asselen *et al* (2018) proposed a formalism which separates the correction due to the effect of the magnetic field on the dose distribution and the correction due to the effect on the detector response: first, a dose conversion factor  $c_B$  is defined as the ratio of the absorbed dose to water in a magnetic field ( $D_{W,Q}^B$ ) to the absorbed dose to water in the absence of the magnetic field ( $D_{W,Q}$ ) at the point of measurement. Second, a conversion factor  $k_{B,M,Q}$  is defined as the ratio of the reading in the absence of the magnetic field ( $M_Q$ ) to the reading in the magnetic field ( $M_Q^B$ ). In consequence, the magnetic field correction factor  $k_{B,Q}$  can be expressed as:

$$k_{B,Q} = c_B \cdot k_{B,M,Q} = \frac{D_{W,Q}^B}{D_{W,Q}} \cdot \frac{M_Q}{M_Q^B} \quad (1)$$

which is essentially the ratio of chamber responses in a beam of beam quality  $Q$  without and with magnetic field. The  $c_B$  conversion factors are typically close to 1.0; deviations of 0.75% for 1.42 T in a 6 MV photon beam (Delfs *et al* 2018) or 0.5% for 1.5 T in a 7 MV beam (O'Brien *et al* 2016) have been reported. The  $c_B$  factors are obtained by Monte Carlo simulations since it is difficult to separate experimentally the change of absorbed dose from the change of detector response in magnetic fields. For an experimental determination of the  $c_B$  factors, a detector that is not affected by the presence of a magnetic field would be needed.

A water calorimeter at the Dutch metrology institute (VSL) is currently the only primary standard to measure the absorbed dose to water in magnetic fields ( $D_W^B$ ) that is directly linked to the international system of units (SI) (de Prez *et al* 2019a). Recently, de Prez *et al* (2019b) reported first  $k_{B,Q}$  factors for PTW 30013 and IBA FC65-G ionization chambers that are based on this primary standard. Several  $k_{B,Q}$  and  $k_{B,M,Q}$  factors were reported that were determined by Monte Carlo calculations or by measurements of detector reading with and without a magnetic field (O'Brien *et al* 2016, Malkov and Rogers 2018, Pojtinger *et al* 2018, van Asselen *et al* 2018, Pojtinger *et al* 2019).

In this work, we have characterized the Fricke detector, a chemical dosimetry method, for its application in MRgRT. The Fricke detector is closely water equivalent and its response is independent of the irradiation energy for equivalent photon energies  $>2$  MeV. Further, its response does not depend on dose rates up to  $10^6$  Gy  $s^{-1}$  (Fricke and Hart 1966, Pettersson and Hettinger 1967, Frankenberg 1969, Shalek and Smith 1969, Klassen *et al* 1999, Moussous *et al* 2011). The Fricke dosimetry method can be used as a primary standard for MeV electrons (Feist 1982, McEwen *et al* 2014) and the Federal Office of Metrology (METAS, Switzerland) has great experience with this application (Stucki *et al* 2003a, 2003b, Stucki and Vörös 2007, Vörös and Stucki 2007, Vörös *et al* 2012). Furthermore, Fricke detectors have been used as secondary standards for several different applications in photon and electron beams as well as in x-rays (Nahum and Greening 1978, Kuszpet *et al* 1982, Feist and Muller 1989, Palm and Mattsson 2002, Austerlitz *et al* 2006, Moussous *et al* 2011, deAlmeida *et al* 2014, Moussous and Medjadj 2016).

The Fricke dosimeter contains ferrous iron ( $Fe^{2+}$ ) that will be oxidized to ferric iron ( $Fe^{3+}$ ) upon irradiation. The increase of the  $Fe^{3+}$  concentration is proportionally to the absorbed dose and it is not expected that the chemical reactions are greatly influenced by the magnetic field, making this detector potentially an ideal candidate for MRgRT applications. Here, we have measured the  $k_{B,M,Q}$  correction factors of the Fricke detector for different magnetic field strengths between 0 T and 1.42 T in a 6 MV photon beam. Additionally, we have tested the feasibility of the Fricke dosimeter for the measurements of output factors.

## 2. Methods and experimental setup

### 2.1. Detector preparation

The Fricke detector consists of a perfluoroalkoxy alkane (PFA) sample cup from AHF Analysetechnik filled to the top with Fricke solution (see figure 1). PFA was used as it is resistant against almost all chemical products, and because of its low surface tension, almost nothing adheres to this material. Therefore, the interaction of the Fricke solution with the vessel wall is small, lowering the self-oxidation processes of the Fricke solution. The sample cup has a diameter of 11.85 mm, a height of 36 mm and a wall thickness of approximately 0.21 mm. The sample cup is mounted on a holder during the irradiation as shown in figure 1(b).

For the preparation of the Fricke solution, 112 ml concentrated sulfuric acid (96%, suprapur) was diluted in a 5 l volumetric flask to  $0.4$  mol  $l^{-1}$  using ultrapure water from a Milli-Q Advantage A10 system. The concentration of the solution was verified by titration of  $1$  mol  $l^{-1}$  NaOH. To eliminate non-linearity effects in the dose response curve, two drops of  $H_2O_2$  (4%, suprapur) were added and neutralized with  $KMnO_4$  solution (1%, pro analysis) as described in Davies and Law (1963). The Fricke solution was then prepared with  $1$  mmol  $l^{-1}$  ammonium iron(II) sulfate ( $(NH_4)Fe(II)(SO_4)_2 \cdot 6H_2O$  (pro analysis),  $1$  mmol  $l^{-1}$  NaCl (suprapur) and  $0.4$  mol  $l^{-1}$  sulfuric acid.

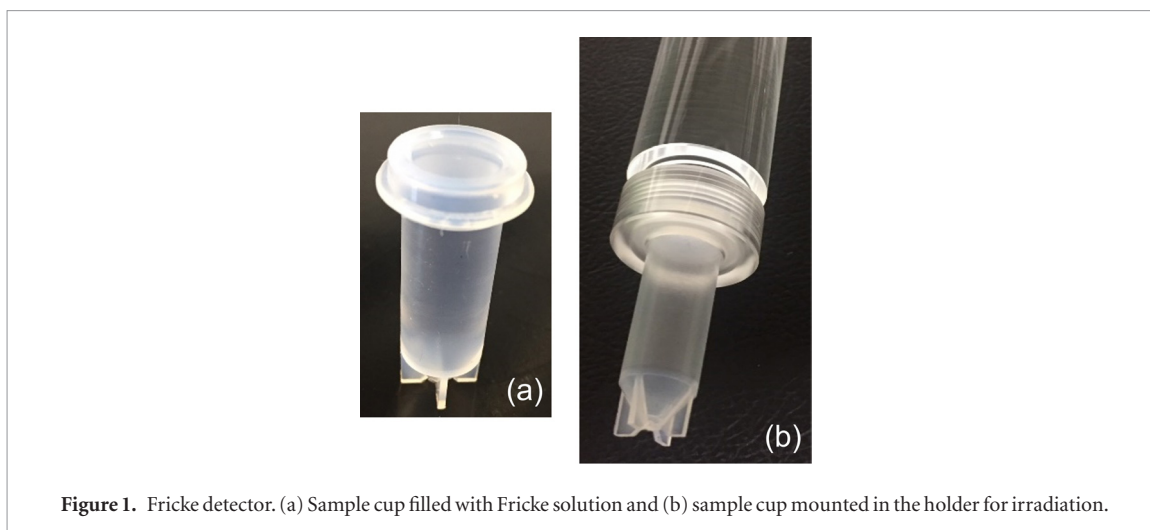


**Figure 1.** Fricke detector. (a) Sample cup filled with Fricke solution and (b) sample cup mounted in the holder for irradiation.

The Fricke solution was prepared freshly on the first measurement day and was used during the next 1–2 weeks. The solution was stored in PFA bottles (1 l) that were covered with aluminum foil to protect the solution from light and to lower the self-oxidation processes (ISO 51026 2015). The Fricke solution was transferred to two sample cups shortly before the photon irradiation (see section 2.3) using a PFA wash bottle that was filled each day with the stored solution. It was taken care that no air bubbles were inside the sample cup. One of the two sample cups was irradiated; the other one was kept near the UV-spectrophotometer at 20 °C and was used as control.

## 2.2. Detector readout

Details about the working principle of the Fricke detector can be found in e.g. Fricke and Hart (1966). Here, only the details are discussed, that are relevant for this study. The absorbed dose to the Fricke solution ( $D_F$ ) was determined as described in ISO 51026 (2015) using the following equation:

$$D_F = \frac{\Delta A}{\rho \cdot l \cdot \varepsilon \cdot G} \quad (2)$$

where  $\Delta A$  is the absorbance change of the Fricke solution upon irradiation,  $\rho$  is the density of the Fricke solution,  $l$  is the path length through the photometric cell,  $\varepsilon$  is the molar extinction coefficient of  $\text{Fe}^{3+}$  and  $G$  is the radiation chemical yield.  $\Delta A$  was determined with a Cary 6000i UV-spectrophotometer (Varian) at a wavelength of 304 nm, with a spectral bandwidth of 1.5 nm. The determined absorbance values are an average over 2 min. The used quartz photometric cell had a path length of  $0.9986 \pm 0.0005$  cm, as calibrated by METAS. The molar extinction coefficient ( $\varepsilon$ ) and the radiation chemical yield ( $G$ ) are given in the ICRU Report 90 (2014) as a combined value of  $\varepsilon \cdot G = 3.525 \text{ cm}^2 \text{ J}^{-1}$ . However, as only relative measurements were performed where detector readings in an applied magnetic field were compared to readings without a magnetic field, the absolute value of  $\rho \cdot l \cdot \varepsilon \cdot G$  is not needed since it is the same for all measurements.

The temperature in the photometric cell was held constant at the reference temperature of 25 °C using a thermostat (Lauda Eco 420). The temperature during each irradiation was recorded and all  $\Delta A$  values were corrected to the reference temperature of 25 °C ( $= \Delta A_{25^\circ\text{C}}$ ) using the correction given by DIN 6800-3 (1980), which we have experimentally verified.

To obtain the absorbed dose to water ( $D_W$ ), correction factors have to be applied to  $D_F$ , as described e.g. in deAlmeida *et al* (2014). These corrections include a dose conversion from the Fricke solution to water and a correction for the vessel wall. Since they are not influenced by the magnetic field and since only relative measurements were performed, these corrections were not applied in this study.

The photometric cells were filled with a Pasteur pipette and emptied with a suction tube. Before each absorbance measurement, the photometric cell was rinsed with solution at least 2 times. For each sample, a new Pasteur pipette was used which has been cleaned with chrome sulfuric acid and ultrapure water. To compensate absorbance effects of the sulfuric acid and the photometric cells in the probe and reference beams of the spectrophotometer, a solution with the same composition as the Fricke solution but without any iron (basic solution) was filled into both photometric cells and the absorbance was measured at the beginning of each measurement day. This absorbance value was stored in the spectrophotometer application and subtracted from all subsequent measurements. By measuring the absorbance of the basic solution periodically during the day, the absorbance drift of the spectrometer was determined. However, no correction for this drift was applied as the absorbance of the unirradiated sample and of the irradiated sample were measured only 10 min apart and the drift was negligible. The

absorbance measurements were performed typically 5–10 min but never longer than 1.5 h after the irradiation in order to keep the self-oxidation of the solution as low as possible.

### 2.3. Irradiation setup

The irradiation was performed at the experimental facilities of the German metrology institute Physikalisch-Technische Bundesanstalt (PTB) in Brunswick. Recently, the irradiation setup was described by Schüller *et al* (2019). The irradiations were performed in a 6 MV photon beam of a linear accelerator (Elekta Precise Treatment System) using a dose rate of 2–3 Gy min<sup>-1</sup> and a pulse repetition frequency of 400 Hz. A magnetic field was generated between the pole shoes of a constant-current driven electromagnet (Bruker ER0173W), which was homogeneous within 1  $\mu$ T over 1 cm<sup>3</sup> region up to 1.42 T (Delfs *et al* 2018). The photon beam (directed in  $z$ ) and the magnetic field (directed in  $x$ ) crossed orthogonally in the water phantom, as shown in figure 2. The freshly prepared Fricke detectors (see section 2.1) were placed at 10 cm water equivalent depth inside a water phantom with dimensions 7 cm ( $x$ )  $\times$  21 cm ( $y$ )  $\times$  21 cm ( $z$ ).

Dose response curves (see section 3.1) were recorded in the presence of magnetic field strengths ( $B$ ) of 0 T, 0.6 T and 1.2 T by irradiating the Fricke detectors in a 6 MV photon beam ( $5 \times 10$  cm<sup>2</sup>) with approximately 1070 monitor units (MU) ( $\approx 6$  Gy), 7100 MU ( $\approx 40$  Gy), and 17 800 MU ( $\approx 100$  Gy). For the determination of  $k_{B,M,Q}$  and the output factors (see sections 3.2 and 3.3), the Fricke detectors were irradiated with approximately 7100 MU using different magnetic field strengths (0 T–1.42 T) and different radiation field sizes ( $3 \times 3$  cm<sup>2</sup>– $5 \times 10$  cm<sup>2</sup>). The same number of monitor units were used for irradiation with the magnetic field switched on as for the irradiations without magnetic field. The independence of the internal monitor readings from the magnetic field has been confirmed within 0.15% (Delfs *et al* 2018). For the determination of the absorbed dose to water ( $D_W$  and  $D_W^B$ ), the monitor of the accelerator was calibrated at  $B = 0$  T in a photon-beam size of  $5 \times 10$  cm<sup>2</sup>, using an ionization chamber (IBA FC65-G or PTW 30013) with the appropriate correction factors for temperature, pressure, saturation and beam quality (Andreo *et al* 2006; DIN6800-2, 2008). Afterwards, the monitor readings at  $B = 0$  T in a photon-beam size of  $5 \times 10$  cm<sup>2</sup> were checked periodically each morning, noon and evening by comparing the monitor units with  $D_W$  measured with the ionization chamber. A linear correction for the drift of the monitor readings was assumed.

For each setting, 3–4 Fricke detectors were irradiated and evaluated. Since the delivered absorbed dose to water changed slightly from irradiation to irradiation, the detector readings (see section 2.2) were normalized with the average value of  $D_W$  so that the mean value of the detector readings for each setting could be determined.

## 3. Results

### 3.1. Linearity of the response

In figure 3(a) the Fricke readings ( $\Delta A_{25^\circ\text{C}}$ ) versus the absorbed dose to water ( $D_W$ ) for a 6 MV photon beam applying magnetic field strengths of 0 T, 0.6 T and 1.2 T are shown. The points correspond to the average value of 3–4 measurements. The experimental standard deviation of each  $\Delta A_{25^\circ\text{C}}$  is approximately 0.3%. All dose response curves are linear with a slope ( $\Delta A_{25^\circ\text{C}}/D_W$ ) of about 0.00356 Gy<sup>-1</sup>, with a correlation coefficient of 1.00000. In figure 3(b) the deviation of the measured  $\Delta A_{25^\circ\text{C}}$  values from the fitted slope are shown. The deviation is smaller than 0.4% for all data points, hardly exceeding the measurement uncertainties.

### 3.2. $k_{B,M,Q}$ factors

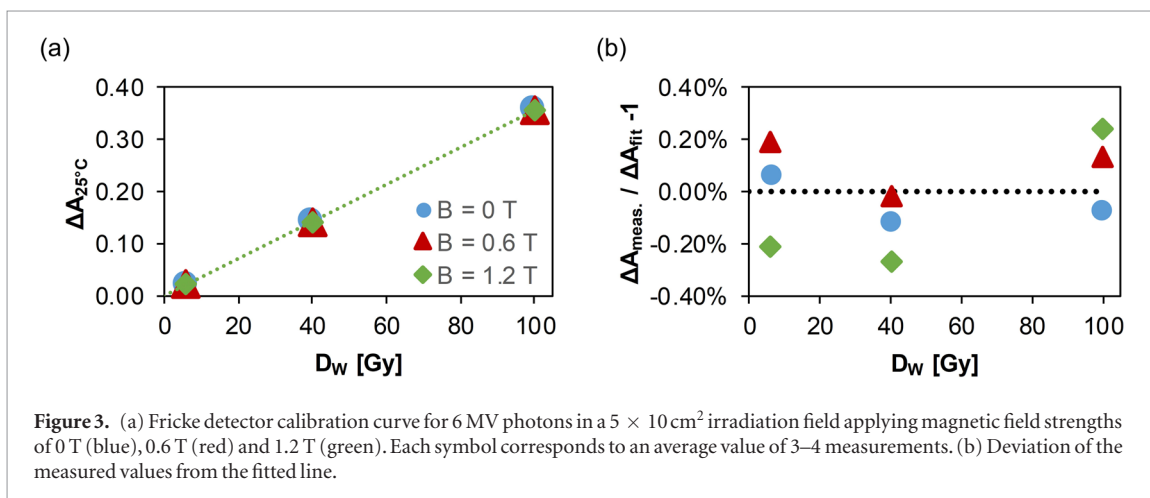
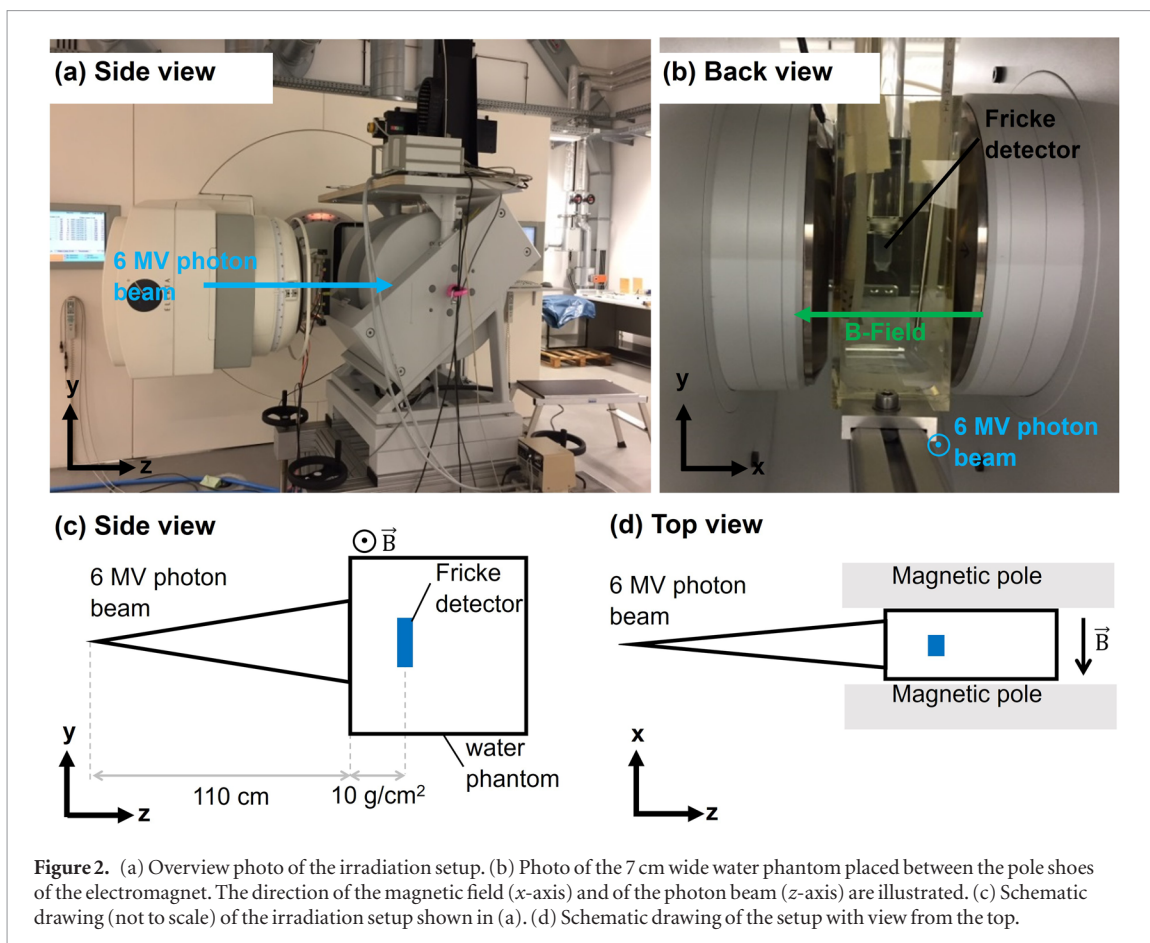
Following the notation of van Asselen *et al* (2018),  $k_{B,M,Q}$  is defined as the ratio of the detector readings without a magnetic field ( $M_Q$ ) to the readings in the magnetic field ( $M_Q^B$ ), see equation (1). For the Fricke detector, the readings correspond to the absorbance change ( $\Delta A$ ) upon irradiation. As described in section 2.2, the influence of the irradiation and readout temperatures on the Fricke readings were corrected.

$$k_{B,M,Q} = \frac{M_Q}{M_Q^B} = \frac{\Delta A_{25^\circ\text{C}}}{\Delta A_{25^\circ\text{C}}^B}. \quad (3)$$

Figure 4 shows the determined  $k_{B,M,Q}$  factors for the Fricke detector measured in a  $5 \times 10$  cm<sup>2</sup> 6 MV photon beam. The measurements for  $B = 0.6$  T and 1.2 T have been repeated several months later to verify the reproducibility of the results, which is discussed in section 4.1. The error bars correspond to the relative combined standard uncertainty ( $k = 1$ ), see table 1.

### 3.3. Output factors

The output factor is defined as the ratio of the dose at the position  $P$  in a phantom for a field size  $A$ , to the dose at the same position  $P$  in a  $10 \times 10$  cm<sup>2</sup> reference field (Podgorsak 2005). The largest possible field in our experimental setup was only  $5 \times 10$  cm<sup>2</sup> due to the limited spacing between the magnet poles. Hence, the output factors for the Fricke detector are normalized to this field size. Typically, the output factors are shown as a function of equivalent



square fields with the assumption that the output for rectangular fields is equal to the output for the equivalent square field. The rectangular fields with sides  $a$  and  $b$  were recalculated to a square field with sides  $a_{eq}$  using Day's rule (Podgorsak 2005).

Figure 5 shows the output factors for the Fricke detector in the presence of different magnetic fields. Note that for the  $4 \times 10 \text{ cm}^2$ ,  $3 \times 10 \text{ cm}^2$  and  $2 \times 10 \text{ cm}^2$  fields only  $B = 0 \text{ T}$  and  $B = 1.42 \text{ T}$  were applied, whereas for the other fields also  $B = 0.35 \text{ T}$ ,  $B = 0.6 \text{ T}$  and  $B = 1.2 \text{ T}$  were applied. Only small changes of the output factors due to the magnetic fields are observed for fields  $> 2 \times 2 \text{ cm}^2$  ( $< 1\%$ ), see figure 6. Here, all output factors are smaller in the presence of a magnetic field compared to the measurements without an applied magnetic field.

## 4. Discussion

### 4.1. Reproducibility and dose response linearity of the Fricke detector

The experimental standard deviation of  $\Delta A_{25^\circ\text{C}}$  for measurements without an applied magnetic field in a  $5 \times 10 \text{ cm}^2$  irradiation beam is approximately 0.3% in the range of absorbed dose to water between 6 Gy to 100 Gy,



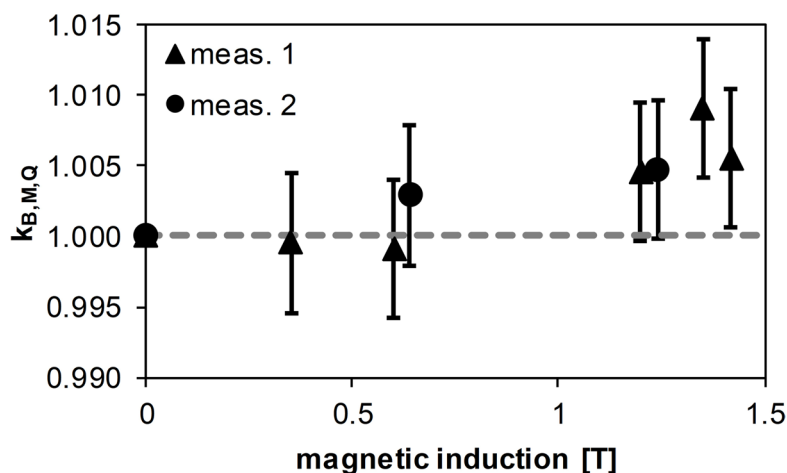


**Figure 4.**  $k_{B,M,Q}$  factors measured in a 6 MV photon beam ( $5 \times 10 \text{ cm}^2$ ) by applying different magnetic field strengths. Two sets of measurements are shown which were recorded several months apart. The magnetic induction of measurement set 2 (●) are offset from set 1 (▲) to show the data more clearly. The error bars correspond to the relative combined standard uncertainty ( $k = 1$ ), see table 1.

**Table 1.** Relative standard uncertainties  $u(X_i)/X_i$  for the calculation of  $k_{B,M,Q}$  ( $= \Delta A_{25^\circ\text{C}}/\Delta A_{25^\circ\text{C}}^B$ ).

Quantity $X_i$	$u(X_i)/X_i$
Fricke readings without magnetic field	
Monitor calibration	0.317%
Stability of monitor calibration over a day	0.058%
Stability of spectrophotometer over 10 min <sup>a</sup>	0.013%
Repeatability of absorbance <sup>a</sup>	0.070%
Solution temperature during detector readout	0.014%
Change of temperature during irradiation	0.015%
Positioning of detector (depth in water)	0.039%
Fricke readings with magnetic field	
Monitor calibration	0.317%
Stability of monitor calibration over a day	0.058%
Independence of monitor from B-field <sup>b</sup>	0.150%
Stability of spectrophotometer over 10 min <sup>a</sup>	0.013%
Repeatability of absorbance <sup>a</sup>	0.070%
Solution temperature during detector readout	0.014%
Change of temperature during irradiation	0.015%
Positioning of detector (depth in water)	0.039%
Relative combined standard uncertainty	0.494%
Expanded relative uncertainty	0.977%

<sup>a</sup> The relative uncertainty was determined for typically measured  $\Delta A_{25^\circ\text{C}}$  values.

<sup>b</sup> See Delfs *et al* (2018).

see table 2, which is in the same magnitude as reported by Moussous *et al* (2011) for their measurements between 5 Gy and 25 Gy. In table 2 also the experimental standard deviation of  $\Delta A_{25^\circ\text{C}}$  measured in the presence of different magnetic field strengths are shown. They are with up to 0.5% slightly higher than for  $B = 0$  T. The different magnetic field strengths were not always applied in the same sequence and dependent on that sequence slightly different  $\Delta A_{25^\circ\text{C}}$  values were measured. The largest changes were observed when  $B = 1.42$  T was applied directly after  $B = 0$  T. It seemed that the monitor of the accelerator, which was used as reference, was slightly influenced by the magnetic field dependent on the sequence of the applied magnetic field strengths.

Measurements of  $k_{B,M,Q}$  factors were performed several months apart. They agree within 0.5%, see the two measurement sets in figure 4.

Figure 3 demonstrates that the Fricke detector has a linear dose response between 6 Gy and 100 Gy. The linearity is not affected by the presence of a magnetic field. The measured dose response curves with a slope of approximately  $0.00356 \text{ Gy}^{-1}$  are comparable with the results Moussous *et al* (2011) obtained for 6 MV photon beams ( $0.0036 \text{ Gy}^{-1}$ ), although they used glass-walled bottle-shaped ampoules while we used PFA sample cups.

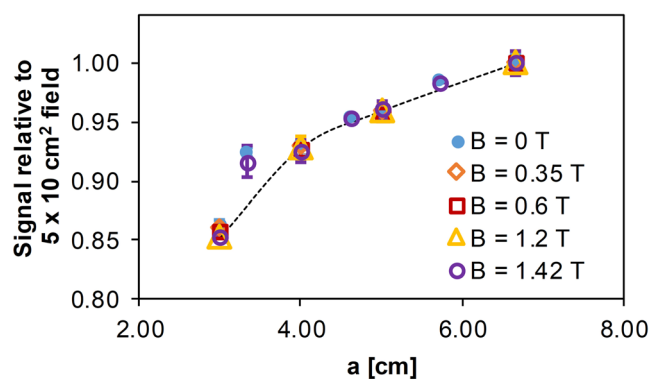


Figure 5. Output factors measured with the Fricke detector in the presence of different magnetic field strengths.

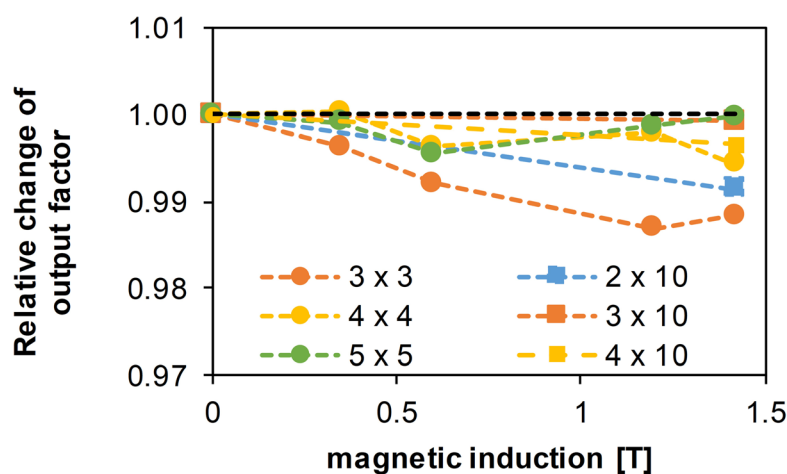


Figure 6. Dependence of the output factors (signal relative to the  $5 \times 10 \text{ cm}^2$  field) on the magnetic field strengths for irradiation field sizes  $> 2 \times 2 \text{ cm}^2$ .

Table 2. Reproducibility of the Fricke detectors for measurements without an applied magnetic field and for  $D_W = 39.89 \text{ Gy}$  applying different magnetic field strengths ( $B$ ).

Dose [Gy]	Mean <sup>a</sup>	SD <sup>b</sup>
6.03	0.021 52	0.20%
40.08	0.142 74	0.32%
99.92	0.355 99	0.33%
B-field [T]	Mean <sup>a</sup>	SD <sup>b</sup>
0	0.141 80	0.34%
0.35	0.141 86	0.15%
0.6	0.141 92	0.49%
1.2	0.141 16	0.35%
1.42	0.141 02	0.49%

<sup>a</sup> Mean value of 3–4 readings of  $\Delta A_{25 \text{ }^\circ\text{C}}$ .

<sup>b</sup> Experimental standard deviation of  $\Delta A_{25 \text{ }^\circ\text{C}}$ .

For both measurements, it was assumed that the detectors are water equivalent and no corrections for the different materials were applied to convert  $D_F$  into  $D_W$ .

Although only relative measurements were performed in this study where Fricke readings with and without the presence of a magnetic field were compared, the plausibility of our Fricke measurements for  $B = 0 \text{ T}$  was verified by determining  $\varepsilon \cdot G$  and comparing it to the literature. The slope of the dose response curve for  $B = 0 \text{ T}$  was converted to  $\varepsilon \cdot G$ , see equation (2), using the density of the Fricke solution  $\rho$  and the path length through the photometric cell  $l$ . A value of  $\varepsilon \cdot G = 3.491 \text{ cm}^2 \text{ J}^{-1}$  is obtained, which is 1% lower than the value recommended in the ICRU report 90 (2014) for 6–15 MeV electron beams. According to this reference,  $\varepsilon \cdot G$  decreases for smaller beam energies, e.g.  $\varepsilon \cdot G$  is 0.7% smaller for  $^{60}\text{Co}$  beams. As the corrections to convert  $D_F$  into  $D_W$  were

**Table 3.**  $k_{B,M,Q}$  and  $k_{B,Q}$  factors measured with the Fricke detector in a  $5 \times 10 \text{ cm}^2$  photon beam (6 MV).

B-field [T]	$k_{B,M,Q}$	$k_{B,Q}$
0.35	0.9995	0.9948
0.6	0.9991	
1.2	1.0045	
1.35	1.0091	
1.42	1.0055	0.9980

not applied in this study, a deviation from the recommended value is expected. For pyrex glass vials, a material which has approximately the same density as the used PFA, a correction of 0.62% for 6 MV beams is predicted (Ma *et al* 1993). Hence, the predicted correction is close to the observed deviation of 1%. Note that for the determination of  $k_{B,M,Q}$  and output factors, the ratio of two Fricke readings is calculated and therefore possible deviations cancel out.

#### 4.2. $k_{B,M,Q}$ and $k_{B,Q}$ factors

Table 3 summarizes the  $k_{B,M,Q}$  factors measured in a  $5 \times 10 \text{ cm}^2$  6 MV photon beam (see also figure 4). The change induced by the magnetic field on the Fricke readings slightly increases with the magnetic field strength, but it is smaller than 0.95% for all measurements. This increase is expected, as the altered dose distribution, which is corrected with the dose conversion factor  $c_B$ , is more influence by larger magnetic field strengths (Delfs *et al* 2018).  $c_B$  factors for 0.35 T and 1.42 T, calculated for the same setup as used in this work, were published to be 0.47% and 0.75%, respectively (Delfs *et al* 2018). As shown in equation (1),  $k_{B,Q}$  is obtained by multiplying  $c_B$  with  $k_{B,M,Q}$ . The  $k_{B,Q}$  factors for the Fricke detector are listed in table 3. The correction due to the magnetic field is 0.52% and 0.20% for 0.35 T and 1.42 T, respectively. The measurement uncertainty of the  $k_{B,M,Q}$  factors are in the same magnitude, see table 1. Hence, no significant change of the Fricke response due to the magnetic field could be observed.

#### 4.3. Influence of magnetic field on Fricke output factors

Moussous and Medjadj (2016) have shown that output factors measured with Fricke detectors for field sizes between  $5 \times 5 \text{ cm}^2$  and  $20 \times 20 \text{ cm}^2$  in a  $^{60}\text{Co}$  beam agree within 0.5% with ionization chamber measurements (WDIC70#141), when no magnetic field is applied. Here, we have measured output factors in the presence of magnetic field strengths between 0 T and 1.42 T using Fricke detectors. As shown in figure 6, the output factors decrease slightly in the presence of a magnetic field for irradiation beam sizes  $>2 \times 2 \text{ cm}^2$ . This was expected since we have measured all output factors at the same position although the presence of magnetic fields shift the depth dose profiles. Additionally, the applied magnetic field leads to a skew of the lateral beam profiles. Both effects will decrease the local dose at the measured position. It is expected that for smaller irradiation field sizes, larger changes in the output factors will occur since the asymmetry of the lateral dose profiles will be more pronounced (O'Brien *et al* 2017). This was indeed observed with the Fricke detectors. As shown in figure 6, the changes for the  $3 \times 3 \text{ cm}^2$  field are larger than for the  $5 \times 5 \text{ cm}^2$  field.

The agreement of the Fricke output factors at 0 T with microDiamond (PTW 60019), diode (PTW 600012) or Semiflex 3D (PTW 31021) measurements is within 0.7% for field sizes  $\geq 4 \times 4 \text{ cm}^2$ . By comparing the Fricke results for 1.42 T with the microDiamond, diode and Semiflex 3D results for 1.5 T, the same findings as for 0 T were observed.

## 5. Conclusions

The linearity of the Fricke response curves between 6 Gy and 100 Gy is not influenced by an applied magnetic field during the irradiation with a 6 MV photon beam. The slope of these response curves are with about  $0.00356 \text{ Gy}^{-1}$  comparable with previously published values (Moussous *et al* 2011, ICRU 2014, ISO 2015). The difference of approximately 1% is explainable with the fact that no correction for the conversion from  $D_F$  to  $D_W$  was applied in this work. For measurements of  $k_{B,M,Q}$  and the output factors, this correction was not needed as they are the same for all measurements and therefore cancel out for these relative measurements.

The experimental standard deviation is approximately 0.3% for measurements without an applied magnetic field and increases slightly to 0.5% in the presence of a magnetic field. Measurements performed several months apart, agree within 0.5% with each other.

By irradiating Fricke detectors with 7100 MU in magnetic fields with different field strengths (0–1.42 T),  $k_{B,M,Q}$  factors were determined. The Fricke readings change less than 0.95% for all applied magnetic field strengths in the  $5 \times 10 \text{ cm}^2$  irradiation field. Using the published  $c_B$  dose conversion factors for 0.35 T and 1.42 T (Delfs *et al* 2018), the magnetic field correction factors  $k_{B,Q}$  of 0.9948 and 0.9980 were obtained for the Fricke

detector. Since the corrections are in the same magnitude as the measurement uncertainty, it can be assumed that the detectors are not significantly influenced by the presence of a magnetic field.

Output factors were determined with the Fricke detector at a water depth of 5 cm. The measured output factors agree within 0.7% with microDiamond, diode and Semeflex 3D results for irradiation field sizes  $\geq 4 \times 4 \text{ cm}^2$ . The measurements in the presence of different magnetic field strengths showed that the output factors decrease with the applied magnetic field strengths. This decrease is more pronounced for smaller field sizes, due to shifts of the depth dose curves and asymmetry of lateral dose profiles.

## Acknowledgments

This work was funded by EURAMET through EMPIR Grant No. 15HLT08 MRgRT.

## ORCID iDs

Maria A Trachsel  <https://orcid.org/0000-0002-8754-673X>

Stefan Pojtinger  <https://orcid.org/0000-0001-6397-4572>

## References

- Agnew J, O'Grady F, Young R, Duane S and Budgell G J 2017 Quantification of static magnetic field effects on radiotherapy ionization chambers *Phys. Med. Biol.* **62** 1731–43
- Andreo P, Burns D T, Hohlfeld K, Huq M S, Kanai T, Laitano F, Smyth V and Vynckier S 2006 *Absorbed Dose Determination in External Beam Radiotherapy: an International Code of Practice for Dosimetry based on Standards of Absorbed Dose to Water (IAEA TRS 398)* (Vienna: IAEA)
- Austerlitz C, Souza V and Villar A 2006 The use of Fricke dosimetry for low energy x-rays *Braz. Arch. Biol. Technol.* **49** 25–30
- Davies J V and Law J 1963 Practical aspects of ferrous sulphate dosimetry *Phys. Med. Biol.* **8** 91–6
- de Prez L, de Pooter J, Jansen B, Woodings S, Wolthaus J, Asselen B, van Soest T, Kok J and Raaymakers B 2019a Commissioning of a water calorimeter as a primary standard for absorbed dose to water in magnetic fields *Phys. Med. Biol.* **64** 035013
- de Prez L, Woodings S, de Pooter J, van Asselen B, Wolthaus J, Jansen B and Raaymakers B 2019b Direct measurement of ion chamber correction factors,  $k_Q$  and  $k_B$ , in a 7 MV MRI-linac *Phys. Med. Biol.* **64** 105025
- deAlmeida C E, Ochoa R, Lima M C, David M G, Pires E J, Peixoto J G, Salata C and Bernal M A 2014 A feasibility study of Fricke dosimetry as an absorbed dose to water standard for  $^{192}\text{Ir}$  HDR sources *PLoS One* **9** e115155
- Delfs B, Schoenfeld A A, Poppinga D, Kapsch R-P, Jiang P, Harder D, Poppe B and Looe H K 2018 Magnetic fields are causing small, but significant changes of the radiochromic EBT3 film response to 6 MV photons *Phys. Med. Biol.* **63** 035028
- DIN 6800-2 2008 *Procedures of Dosimetry for Probe Type Detectors for Photon and Electron Radiation: Part 2. Ionization Chamber Dosimetry of High Energy Photon and Electron Radiation* (Berlin: Beuth)
- DIN 6800-3 1980 *Dosismessverfahren in der radiologischen Technik—Eisensulfatdosimetrie* (Berlin: Beuth)
- Feist H 1982 Determination of the absorbed dose to water for high-energy photons and electrons by total absorption of electrons in ferrous sulphate solution *Phys. Med. Biol.* **27** 1435–47
- Feist H and Muller U 1989 Measurement of the total stopping power of 5.3 MeV electrons in polystyrene by means of electron beam absorption in ferrous sulphate solution *Phys. Med. Biol.* **34** 1863–9
- Frankenberg D 1969 A ferrous sulphate dosimeter independent of photon energy in the range from 25 keV up to 50 MeV *Phys. Med. Biol.* **14** 597–605
- Fricke H and Hart E J 1966 Chemical dosimetry *Radiation Dosimetry* **2** 167–239
- ICRU 2014 Key data for ionizing-radiation dosimetry: measurement standards and applications (ICRU Report 90) *J. ICRU* **14** 1–118
- ISO 2015 *Practice for Using the Fricke dosimetry System* (Geneva: ISO/ASTM 51026)
- Klassen N V, Shortt K R, Seuntjens J and Ross C K 1999 Fricke dosimetry: the difference between  $G(\text{Fe}^{3+})$  for  $^{60}\text{Co}$  gamma-rays and high-energy x-rays *Phys. Med. Biol.* **44** 1609–14
- Kuszpet M E, Feist H, Collin W and Reich H 1982 Determination of  $C_\lambda$  and  $C_E$  conversion factors and stopping power ratios using calibrated ferrous sulphate dosimeters *Phys. Med. Biol.* **27** 1419–33
- Legendijk J J W, Raaymakers B W, Van den Berg C A T, Moerland M A, Philippens M E and van Vulpen M 2014 MR guidance in radiotherapy *Phys. Med. Biol.* **59** R349–69
- Looe H K, Delfs B, Poppinga D, Harder D and Poppe B 2017 Magnetic field influences on the lateral dose response functions of photon-beam detectors: MC study of wall-less water-filled detectors with various densities *Phys. Med. Biol.* **62** 5131–48
- Ma C-M, Rogers D W O, Shortt K R, Ross C K, Nahum A E and Bielajew A F 1993 Wall-correction and absorbed dose conversion factors for Fricke dosimetry: Monte Carlo calculations and measurements *Med. Phys.* **20** 283–92
- Malkov V N and Rogers D W O 2018 Monte Carlo study of ionization chamber magnetic field correction factors as a function of angle and beam quality *Med. Phys.* **45** 908–25
- McEwen M, Gamal I, Mainegra-Hing E and Cojocaru C 2014 *Report PIRS-1980: Determination of the Radiation Chemical Yield (G) for the Fricke Chemical Dosimetry System in Photon and Electron Beams* (Canada: National Research Council Canada) (<https://doi.org/10.4224/23002718>)
- Meijsing I, Raaymakers B W, Raaijmakers A J E, Kok J G M, Hogeweg L, Liu B and Legendijk J J W 2009 Dosimetry for the MRI accelerator: the impact of a magnetic field on the response of a Farmer NE2571 ionization chamber *Phys. Med. Biol.* **54** 2993–3002
- Moussous O, Khoudri S and Benguerba M 2011 Characterization of a Fricke dosimeter at high energy photon and electron beams used in radiotherapy *Australas. Phys. Eng. Sci. Med.* **34** 523–8
- Moussous O and Medjadji T 2016 A standard Fricke dosimeter compared to an ionization chamber used for dosimetric characterization of  $^{60}\text{Co}$  photon beam *Pol. J. Med. Phys. Eng.* **22** 19–24
- Nahum A E and Greening J R 1978 A detailed re-evaluation of  $C_\lambda$  and  $C_E$  with application to ferrous sulphate G-values *Phys. Med. Biol.* **23** 894–908

- O'Brien D J, Dolan J, Pencea S, Schupp N and Sawakuchi G O 2018 Relative dosimetry with an MR-linac: response of ion chambers, diamond, and diode detectors for off-axis, depth dose, and output factor measurements *Med. Phys.* **45** 884–97
- O'Brien D J, Roberts D A, Ibbott G S and Sawakuchi G O 2016 Reference dosimetry in magnetic fields: formalism and ionization chamber correction factors *Med. Phys.* **43** 4915–27
- Palm Å and Mattsson O 2002 Experimental determination of beam quality conversion factors in clinical photon beams using ferrous sulphate (Fricke) dosimetry *Med. Phys.* **29** 2756–62
- Pettersson C and Hettinger G 1967 Dosimetry of high-energy electron radiation based on the ferrous sulphate dosimeter *Acta Radiol. Ther.* **6** 160–76
- Podgorsak E B 2005 *Radiation Oncology Physics: a Handbook for Teachers and Students* (Vienna: IAEA)
- Pojtinger S, Dohm O S, Kapsch R-P and Thorwarth D 2018 Ionization chamber correction factors for MR-linacs *Phys. Med. Biol.* **63** 11NT03
- Pojtinger S, Kapsch R-P, Dohm O S and Thorwarth D 2019 A finite element method for the determination of the relative response of ionization chambers in MR-linacs: simulation and experimental validation up to 1.5 T *Phys. Med. Biol.* **64** 135011
- Raaijmakers A J E, Raaymakers B W and Legendijk J J W 2007 Experimental verification of magnetic field dose effects for the MRI-accelerator *Phys. Med. Biol.* **52** 4283–91
- Raaijmakers A J E, Raaymakers B W and Legendijk J J W 2008 Magnetic-field-induced dose effects in MR-guided radiotherapy systems: dependence on the magnetic field strength *Phys. Med. Biol.* **53** 909–23
- Raaymakers B W, Raaijmakers A J E, Kotte A N T J, Jette D and Legendijk J J W 2004 Integrating a MRI scanner with a 6 MV radiotherapy accelerator: dose deposition in a transverse magnetic field *Phys. Med. Biol.* **49** 4109–18
- Reynolds M, Fallone B G and Rathee S 2013 Dose response of selected ion chambers in applied homogeneous transverse and longitudinal magnetic fields *Med. Phys.* **40** 042102
- Richter S, Pojtinger S, Mönnich D, Dohm O S and Thorwarth D 2017 Influence of a transverse magnetic field on the dose deposited by a 6 MV linear accelerator *Curr. Dir. Biomed. Eng.* **3** 218–85
- Schmidt M A and Payne G S 2015 Radiotherapy planning using MRI *Phys. Med. Biol.* **60** R323–61
- Schüller A, Pojtinger S, Meier M, Makowski C and Kapsch R-P 2019 The metrological electron accelerator facility (MELAF) for research in dosimetry for radiotherapy *IFMBE Proc.* **68** 589–93
- Shalek R J and Smith C E 1969 Chemical dosimetry for the measurement of high-energy photons and electrons *Ann. New York Acad. Sci.* **161** 44–62
- Smit K, van Asselen B, Kok J G M, Aalbers A H L, Legendijk J J W and Raaymakers B W 2013 Towards reference dosimetry for the MR-linac: magnetic field correction of the ionization chamber reading *Phys. Med. Biol.* **58** 5945–57
- Spindeldreier C K, Schrenk O, Bakenecker A, Kawrakow I, Burigo L, Karger C P, Greilich S and Pfaffenberger A 2017 Radiation dosimetry in magnetic fields with Farmer-type ionization chambers: determination of magnetic field correction factors for different magnetic field strengths and field orientations *Phys. Med. Biol.* **62** 6708–28
- Stucki G, Münch W and Quintel H 2003a The METAS absorbed dose to water calibration service for high energy photon and electron beam radiotherapy *Proc. Int. Symp. Vienna, 2002, IAEA-CN-96-8* pp 103–13
- Stucki G, Schafer R, Brunschwig O and Quintel H 2003b *The METAS Electron Beam Primary Standard Chemical Dosimeter* (Melbourne: Workshop on Recent Advances in Absorbed Dose Standards)
- Stucki G and Vörös S 2007 Experimental  $k_{Q,Q_0}$  electron beam quality correction factors for the types NACP02 and PTW34001 plane-parallel chambers *Absorbed Dose and Air Kerma Primary Standards ADAKPS 2007 Workshop (Paris, 9–11 May 2007)*
- van Asselen B, Woodings S J, Hackett S L, van Soest T L, Kok J G M, Raaymakers B W and Wolthaus J W H 2018 A formalism for reference dosimetry in photon beams in the presence of a magnetic field *Phys. Med. Biol.* **63** 125008
- Vörös S, Anton M and Boillat B 2012 Relative response of alanine dosimeters for high-energy electrons determined using a Fricke primary standard *Phys. Med. Biol.* **57** 1413–32
- Vörös S and Stucki G 2007 Simulation Monte Carlo pour la réalisation d'un étalon primaire de la dose absorbée dans l'eau pour des faisceaux d'électrons *Radioprotection* **42** 565–75
- Wegener S, Weick S and Sauer O A 2019 Influence of a transverse magnetic field on the response of different detectors in a high energy photon beam near the surface *Z. Med. Phys.* **29** 22–30



## PAPER

## OPEN ACCESS


RECEIVED  
12 June 2020REVISED  
9 November 2020ACCEPTED FOR PUBLICATION  
12 November 2020PUBLISHED  
15 December 2020

Original content from this work may be used under the terms of the [Creative Commons Attribution 4.0 licence](https://creativecommons.org/licenses/by/4.0/).

Any further distribution of this work must maintain attribution to the author(s) and the title of the work, journal citation and DOI.



# Experimental determination of magnetic field correction factors for ionization chambers in parallel and perpendicular orientations

Stefan Pojtinger<sup>1,2</sup> , Marcel Nachbar<sup>2</sup>, Sarah Ghandour<sup>3</sup>, Olivier Pisaturo<sup>3</sup>, Marc Pachoud<sup>3</sup>, Ralf-Peter Kapsch<sup>1</sup> and Daniela Thorwarth<sup>2</sup>

<sup>1</sup> Physikalisch-Technische Bundesanstalt, Braunschweig, Germany

<sup>2</sup> University Hospital Tübingen, Biomedical Physics, Tübingen, Germany

<sup>3</sup> Hôpital Riviera-Chablais, Rennaz, Switzerland

E-mail: [Stefan.Pojtinger@ptb.de](mailto:Stefan.Pojtinger@ptb.de)

**Keywords:** MR-linac, dosimetry, alanine dosimetry, ionization chambers, magnetic field correction factors

## Abstract

Magnetic field correction factors are needed for absolute dosimetry in magnetic resonance (MR)-linacs. Currently experimental data for magnetic field correction factors, especially for small volume ionization chambers, are largely lacking. The purpose of this work is to establish, independent methods for the experimental determination of magnetic field correction factors  $k_{\vec{B},Q}$  in an orientation in which the ionization chamber is parallel to the magnetic field. The aim is to confirm previous experiments on the determination of Farmer type ionization chamber correction factors and to gather information about the usability of small-volume ionization chambers for absolute dosimetry in MR-linacs. The first approach to determine  $k_{\vec{B},Q}$  is based on a cross-calibration of measurements using a conventional linac with an electromagnet and an MR-linac. The absolute influence of the magnetic field in perpendicular orientation is quantified with the help of the conventional linac and the electromagnet. The correction factors for the parallel orientation are then derived by combining these measurements with relative measurements in the MR-linac. The second technique utilizes alanine electron paramagnetic resonance dosimetry. The alanine system as well as several ionization chambers were directly calibrated with the German primary standard for absorbed dose to water. Magnetic field correction factors for the ionization chambers were determined by a cross-calibration with the alanine in an MR-linac. Important quantities like  $k_{\vec{B},Q}$  for Farmer type ionization chambers in parallel orientation and the change of the dose to water due the magnetic field ( $c_{\vec{B}}$ ) have been confirmed. In addition, magnetic field correction factors have been determined for small volume ionization chambers in parallel orientation. The electromagnet-based measurements of  $k_{\vec{B},Q}$  for 7 MV/1.5 T MR-linacs and parallel ionization chamber orientations resulted in 0.9926(22), 0.9935(31) and 0.9841(27) for the PTW 30013, the PTW 31010 and the PTW 31021, respectively. The measurements based on the second technique resulted in values for  $k_{\vec{B},Q}$  of 0.9901(72), 0.9955(72), and 0.9885(71). Both methods show excellent accuracy and reproducibility and are therefore suitable for the determination of magnetic field correction factors. Small-volume ionization chambers showed a variation in the resulting values for  $k_{\vec{B},Q}$  and should be cross-calibrated instead of using tabulated values for correction factors.

## 1. Introduction

MR-linacs, which combine magnetic resonance (MR) imaging with medical linear accelerators (linacs) are increasingly available for patient treatment in hospitals. From the start of this technical development, a major challenge has been the establishment of a reliable experimental method for the measurement of the absorbed dose to water in an MR-linac environment. This is because the response of ionization chambers, which are routinely used to calibrate the linac output, is known to be influenced by magnetic fields (Meijsing

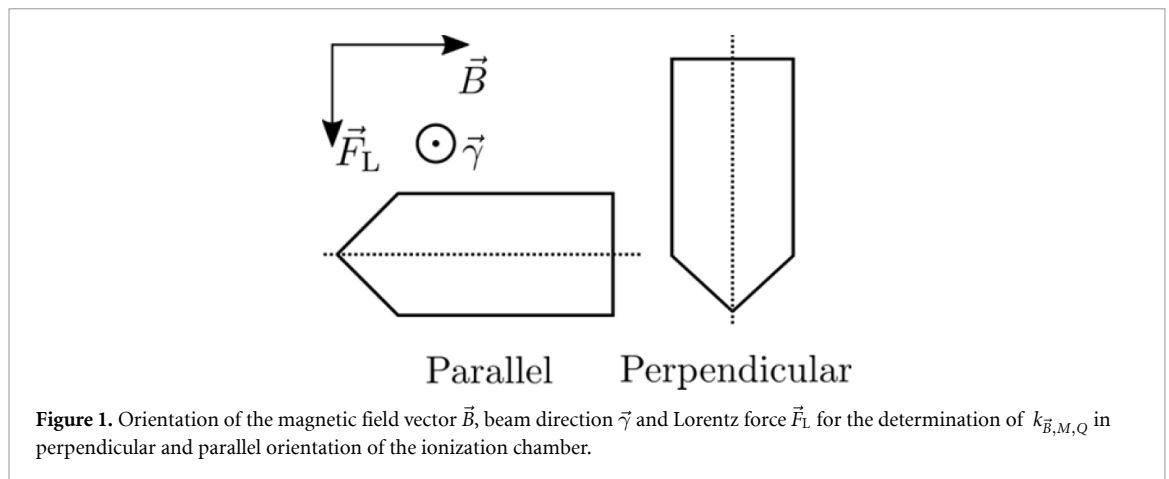


**Figure 1.** Orientation of the magnetic field vector  $\vec{B}$ , beam direction  $\vec{\gamma}$  and Lorentz force  $\vec{F}_L$  for the determination of  $k_{\vec{B},M,Q}$  in perpendicular and parallel orientation of the ionization chamber.

*et al* 2009). Therefore, magnetic field correction factors have been determined in experiments as well as in Monte Carlo simulations for many ionization chambers (Meijsing *et al* 2009, Smit *et al* 2013, O'Brien *et al* 2016, Spindeldreier *et al* 2017, Pojtinger *et al* 2018, 2019, Malkov and Rogers 2018, van Asselen *et al* 2018, de Prez *et al* 2019).

For all MR-linacs, which are commercially available today, the direction of the photon beam is always perpendicular to the magnetic field vector of the  $B_0$  field. As thimble type ionization chambers should be positioned so that the ionization chamber axis is perpendicular to the direction of the photon beam, there are two practically relevant orientations for the positioning of an ionization chamber. One orientation is the orientation in which the ionization chamber axis is perpendicular to the magnetic field, and the other orientation is the one in which the ionization chamber axis is parallel to the magnetic field (figure 1). For the perpendicular orientation, the magnetic field corrections also depend on the orientation of the ionization chamber's tip (Pojtinger *et al* 2019).

In clinical practice, it is commonly assumed that the parallel orientation is preferable, as it has been shown that the influence of the magnetic field on the response of Farmer-type ionization chambers is smaller compared to the perpendicular orientation (van Asselen *et al* 2018, de Prez *et al* 2019). Currently, reliable, experimentally determined correction factors for parallel orientations are only available for Farmer-type ionization chambers. Anyway, it must be mentioned, that some authors have presented results for other types of ionization chambers at international conferences (e.g. Gohil *et al* 2018). The corrections that can be found in the literature were determined by two different methods. One method compared ionization chamber measurements in the same MR-linac with and without a magnetic field (van Asselen *et al* 2018). The second method was based on a direct calibration of the ionization chamber in the MR-linac traceable to a water calorimetry measurement (de Prez *et al* 2019).

In this work, we present two different experimental methods for the determination of magnetic field correction factors for ionization chambers in parallel orientation. One method utilizes a 1.5 T electromagnet to determine the effect of the magnetic field on the ionization chamber in perpendicular orientation using a conventional linac. In a second step, the same ionization chamber is irradiated inside an MR-linac in perpendicular as well as in parallel orientation. This is done to quantify the signal change caused by repositioning the ionization chamber from the perpendicular to the parallel orientation in an MR-linac. Combining the results of both measurements, a magnetic field correction factor can be calculated for the parallel orientation.

The second method presented here is to determine the magnetic field correction for ionization chambers in parallel orientation by cross-calibration directly in the MR-linac with alanine measurements evaluated by electron paramagnetic resonance (EPR) dosimetry. A similar method was presented at an international conference before (Billas *et al* 2017).

The aim of this work is to determine magnetic field correction factors for different ionization chambers positioned in parallel orientation with respect to the magnetic field using those two experimental techniques.

## 2. Material and methods

### 2.1. Formalism

One way to express magnetic field correction factors was previously presented by van Asselen *et al* (2018).

**Table 1.** Ionization chambers used in perpendicular orientation for the experimental determination of the relative response in magnetic fields.

Ionization chamber	Type	S/N	Sensitive volume	
			Radius (mm)	Length (mm)
PTW 30013	Farmer	006762, 009193	3.05	23
PTW 31010	Semiflex	0948, 03289	2.75	6.5
PTW 31021	Semiflex 3D	141576, 141577	2.4	4.8

A magnetic field correction factor  $k_{\vec{B},Q}$  was defined, that can be applied for a specific magnetic flux density  $\vec{B}$  and a specific beam quality  $Q$  to correct the response of an ionization chamber for the influence of the magnetic field.  $k_{\vec{B},Q}$  can be expressed as

$$k_{\vec{B},Q} = c_{\vec{B}} k_{\vec{B},M,Q} \quad (1)$$

where  $c_{\vec{B}}$  describes the change of absorbed dose to water by the magnetic field in a certain set of reference conditions:

$$c_{\vec{B}} = \frac{D_{w,Q}^{\vec{B}}}{D_{w,Q}}. \quad (2)$$

$k_{\vec{B},M,Q}$  is the ratio of the readings of an ionization chamber in the same reference conditions with and without the influence of a magnetic field:

$$k_{\vec{B},M,Q} = \frac{M_Q}{M_Q^{\vec{B}}}. \quad (3)$$

The advantage of this formulation is that  $k_{\vec{B},M,Q}$  can be easily measured and simulated by comparing ionization chamber measurements or simulations with and without the influence of a magnetic field. In contrast, the experimental determination of  $c_{\vec{B}}$  is more challenging. Currently the common approach to determining  $c_{\vec{B}}$  is by Monte Carlo simulations (O'Brien *et al* 2016, Delfs *et al* 2018, Malkov and Rogers 2018, van Asselen *et al* 2018, Billas *et al* 2020). At MR-linacs, the only way to measure  $c_{\vec{B}}$  is by turning off the magnetic field. For economic reasons, this is not practicable in clinical environments.

## 2.2. Electromagnet measurements in perpendicular orientation

The ionization chambers used for this part of the experiments are listed in table 1. In this experiment, the perpendicular orientation is defined as the orientation in which the Lorentz force deflects the secondary electrons towards the tip of the ionization chamber (figure 1).

For irradiation, two medical linacs (Precise Treatment System (151605 and 151617), Elekta AB, Stockholm, Sweden) have been used; the nominal accelerating voltage was set to 4, 6 and 8 MV. An in-house monitor chamber (Kapsch and Krauss 2009) was mounted on the shadow tray of the linac to monitor the accelerator's output. A large electromagnet (ER073W, Bruker, Billerica, USA) was placed in front of the accelerator. A Hall sensor was positioned on one of the pole shoes to monitor the magnetic flux density using a digital teslameter (DTM 151, Group3 Technology Limited, Auckland, New Zealand). A  $6 \times 20 \times 20 \text{ cm}^3$  water phantom was placed in the 6 cm gap between the pole shoes of the magnet. The source-to-surface distance (SSD) was 110 cm. The photon beam was collimated to  $4 \times 10 \text{ cm}^2$  at the isocentre. The reference point of the ionization chambers was placed at a 10 cm water-equivalent depth. All measurements were repeated on three different days including a full repositioning of the detector.

The charge collected by the ionization chambers ( $Q_{\text{probe}}$ ) and the charge collected by the transmission monitor chamber ( $Q_{\text{mon}}$ ) were measured simultaneously using electrometers (Keithley 6517, Keithley Instruments, Solon, USA). The detectors were pre-irradiated with at least 1000 MU before each measurement; the charge was collected for 150 s. Measurements were conducted for a magnetic flux density of  $B = 1.5 \text{ T}$ . This procedure was already used in our previous work (Pojtinger *et al* 2019), where it had been shown to be in agreement with Monte Carlo simulations.

The charge collected by the ionization chamber was normalized to the charge collected by the transmission monitor chamber. Then,  $k_{\vec{B},M,Q}$  in perpendicular orientation was calculated by dividing this ratio measured at 0 T by the ratio at 1.5 T. In this work, the resulting quantity is called  $k_{\perp,Q}$ :

$$k_{\perp,Q} = \left( \frac{Q_{\text{probe}}}{Q_{\text{mon}}} \right)_{B=0 \text{ T}} / \left( \frac{Q_{\text{probe}}}{Q_{\text{mon}}} \right)_{B=1.5 \text{ T}}. \quad (4)$$

$k_{\perp,Q}$  was measured for the beam qualities 4 MV, 6 MV and 8 MV ( $k_{\perp,Q=4 \text{ MV}}$ ,  $k_{\perp,Q=6 \text{ MV}}$  and  $k_{\perp,Q=8 \text{ MV}}$ ). These results were used to demonstrate that  $k_{\perp,Q}$  increases linearly with the photon beam quality specifier



**Table 2.** Ionization chambers used for the experimental determination of the influence of changing the detector's orientation in an MR-linac setup. The dimensions of the ionization chamber's sensitive volumes are summarized in table 1.

Ionization chamber	Type	S/N
PTW 30013	Farmer	006762, 010389
PTW 31010	Semiflex	03289, 007525
PTW 31021	Semiflex 3D	141576, 142175

TPR<sub>20,10</sub>, as it is defined in Andreo *et al* (2006). Then,  $k_{\perp, Q=7 \text{ MV}}$  was calculated by linear interpolation between  $k_{\perp, Q=6 \text{ MV}}$  and  $k_{\perp, Q=8 \text{ MV}}$ :

$$k_{\perp, Q=7 \text{ MV}} = \frac{k_{\perp, Q=8 \text{ MV}} - k_{\perp, Q=6 \text{ MV}}}{\text{TPR}_{20,10}(8 \text{ MV}) - \text{TPR}_{20,10}(6 \text{ MV})} \cdot (\text{TPR}_{20,10}(7 \text{ MV}) - \text{TPR}_{20,10}(6 \text{ MV})) + k_{\perp, Q=6 \text{ MV}} \quad (5)$$

The values for TPR<sub>20,10</sub>, for the conventional linacs have already been published in Krauss and Kapsch (2014). For the MR-linac, TPR<sub>20,10</sub> was presented by de Prez *et al* (2019).

### 2.3. Ionization chamber measurements at the MR-linac

In the second part of the experiments, the ionization chambers were irradiated using a 1.5 T MR-linac (Unity, Elekta AB, Stockholm, Sweden) in perpendicular as well as parallel orientation (see figure 1). Not all the ionization chambers listed in table 1 were available for the experiments at the MR-linac. Therefore, other ionization chambers of the same type have been included with the MR-linac measurements, to investigate intra-type variabilities. The list of ionization chambers that were used for this part of the experiment can be found in table 2.

The ionization chambers were positioned inside an MR-compatible water phantom (Beamscan MR, PTW, Freiburg, Germany). The phantom was placed at SSD = 113.15 cm and the gantry angle was set to 90°. The photon beam was collimated to 10 × 10 cm<sup>2</sup> at the isocentre, what corresponds to a 7.89 × 7.89 cm<sup>2</sup> square field at the SSD. The reference point of the ionization chamber was positioned at a 10 cm water-equivalent depth. Each ionization chamber was irradiated seven times with 200 MU. The collected charge was measured using an electrometer (Unidos Webline (S/N 2161), PTW, Freiburg, Germany). The series of measurements with each ionization chamber was repeated five times, including a full repositioning of the detector in the parallel as well as in the perpendicular orientation.

For the quantification of the influence of the rotation of the chamber axis around the beam direction, the relative change of the chamber response  $c_{\text{rot}}$  has been determined as the ratio of the measured charges in perpendicular ( $Q_{\perp}$ ) and parallel orientation ( $Q_{\parallel}$ ):

$$c_{\text{rot}} = \left( \frac{Q_{\perp}}{Q_{\parallel}} \right)_{B=1.5 \text{ T}} \quad (6)$$

All charges have been corrected for the influence of water temperature and atmospheric pressure.

Then, the total influence of the magnetic field on the measurement in parallel orientation can be calculated as:

$$k_{\parallel} = c_{\text{rot}} \cdot k_{\perp, Q=7 \text{ MV}} \quad (7)$$

### 2.4. Magnetic field correction factors based on alanine measurements

Alanine pellets were irradiated at the 1.5 T MR-linac (Unity, Elekta AB, Sweden) using the same procedure as for the ionization chambers. For this, the alanine pellets were placed inside an inhouse manufactured holder. This holder was made of polymethyl methacrylate and had the shape of the Farmer-type ionization chamber PTW 30013. A stack of eight alanine pellets can be inserted into the tip of this holder (figure 2). The holder was built in such a way that the centre of the fourth pellet sits at the same position as the reference point of a PTW 30013 Farmer ionization chamber, i.e. 13 mm from the tip on the chamber axis. For irradiation, the holder was placed in parallel orientation with respect to the magnetic field (figure 1).

Again, the measurements were repeated five times, including a full repositioning of the alanine holder.

The procedure for evaluating the applied dose on the alanine pellets was previously described in detail elsewhere (Anton 2005, 2006).

To determine the dose distribution perpendicular to the beam axis, the beam profile across the detector length was determined from the readings of the eight alanine pellets contained in the holder in a first step. This was done for all five measurements. After that, the average beam profile was fitted with a cubic

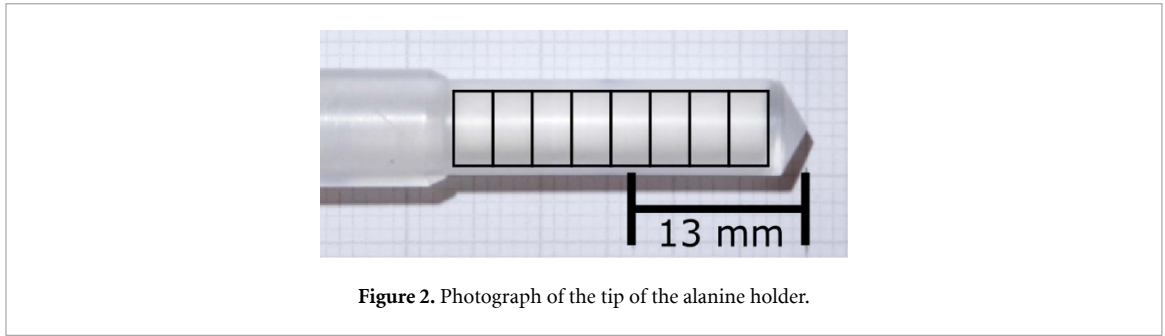


Figure 2. Photograph of the tip of the alanine holder.

Table 3. Ionization chambers used for the experimental determination of the magnetic field correction in parallel orientation. The dimensions of the ionization chamber's sensitive volumes can be found in table 1.

Ionization chamber	Type	S/N
PTW 30013	Farmer	006762
PTW 31010	Semiflex	03289
PTW 31021	Semiflex 3D	141576

polynomial by polynomial regression (see figure 5). The maximum of this function was used to approximate the absorbed dose to water in the centre of the beam and was noted as  $D_{\text{alanine}}$ .

For all ionization chambers in table 3, a cobalt-60 calibration factor ( $N$ ) was determined traceable to the German primary standard of absorbed dose to water at the National Metrology Institute (PTB, Germany). In addition, corrections for the polarity effect ( $k_p$ ) and ion recombination ( $k_s$ ) were determined experimentally at the MR-linac. Values for the beam quality correction factor ( $k_Q$ ) have been taken from Andreo *et al* (2020).

The influence of the magnetic field on the depth dose distribution in water ( $c_{\vec{B}}$ ) was calculated using the Monte Carlo system EGSnrc (Kawrakow *et al* 2019). For this, a full accelerator head model of the Elekta Unity was modeled in BEAMnrc (Rogers *et al* 2018). A detailed description and benchmark of the accelerator head model can be found in Friedel *et al* (2019). The accelerator head model was compiled as a shared library and coupled to the EGSnrc usercode egs\_chamber (Wulff *et al* 2008). Simulation parameters were set in accordance with earlier simulations (Pojtinger *et al* 2018, 2019). The dose was scored for a water cylinder placed at a 10 cm depth inside a  $30 \times 30 \times 30 \text{ cm}^3$  water phantom. The radius of the water cylinder was set to 1 mm and the thickness was set to 0.2 mm. The irradiation conditions were set in accordance to the MR-linac measurements.

A correction for the volume averaging effect ( $k_V$ ) was calculated as described in IAEA TRS-483 (IAEA 2017), by folding the beam profile resulting from the alanine measurements with the ionization chamber's cross-sectional area.

The influence of a magnetic field on measurements using alanine was recently investigated by Billas *et al* (2020). To compensate for this effects, Billas *et al* (2020) introduced an alanine quality correction factor  $k_{\text{al},\vec{B},Q}$ . For this work,  $k_{\text{al},\vec{B},Q}$  was determined experimentally, what will be discussed later.

With the correction for the temperature and pressure ( $k_p$ ), the dose to water measured with an ionization chamber ( $D_{\text{IC}}$ ) can be calculated from the reading of an ionization chamber ( $M_{\text{probe}}$ ) as:

$$D_{\text{IC}} = N k_Q k_p \left( M_{\text{probe}} k_p k_s k_V c_{\vec{B}} k_{\vec{B},M,Q} \right)_{B=1.5 \text{ T}} \quad (8)$$

The quantities that are written inside brackets have been determined directly in the measurement situation, at  $B = 1.5 \text{ T}$ . If the dose to water is measured with an ionization chamber as well as with alanine for the same irradiation conditions,  $D_{\text{IC}}$  can be replaced by  $D_{\text{alanine}}$ :

$$D_{\text{alanine}} = N k_Q \left( k_{\text{al},\vec{B},Q} M_{\text{probe}} k_p k_p k_s k_V c_{\vec{B}} k_{\vec{B},M,Q} \right)_{B=1.5 \text{ T}} \quad (9)$$

This equation can be solved for  $k_{\vec{B},M,Q}$ . Hence, it can be used for the determination of  $k_{\vec{B},M,Q}$  based on an alanine measurement. To make it clear that this equation is based on an alanine measurement, in the context of this equation is noted as  $k_{\text{alanine}}$ :

$$k_{\text{alanine}} = \frac{D_{\vec{B},\text{alanine}}}{N k_Q k_p} \left( \frac{k_{\text{al},\vec{B},Q}}{M_{\text{probe}} k_p k_s k_V c_{\vec{B}}} \right)_{B=1.5 \text{ T}} \quad (10)$$

**Table 4.** Resulting uncertainties based on the uncertainty budget for the determination of  $k_{\text{alanine}}$ .

Quantity $X_i$	$u(X_i) / X_i$
Measurement ionization chamber	0.19%
Calculation of absolute dose IC	0.72%
Calculation of absolute dose alanine	0.31%
Relative combined standard uncertainty	0.80%

### 2.5. Magnetic field correction factors for alanine

To investigate the influence of the magnetic field on the alanine measurements,  $k_{\text{al},\vec{B},Q}$  was directly measured at the 1.5 T MR-linac (Unity, Elekta AB, Sweden) located at the Hôpital Riviera-Chablais (Blonay, Switzerland). At this site it was possible to perform measurements while the magnetic field of the MR-linac was turned off.

Alanine pellets were placed in the alanine holder that was described before and were irradiated for approximately 4700 MU. For this, the alanine holder was positioned in the isocentre of the MR-linac in 10 cm water-equivalent depth, inside of a dedicated water phantom built by the National Physical Laboratory (NPL, Teddington, England). This was repeated three times on two different days, including a full repositioning of the alanine holder. After ramping the magnetic field, the measurements were repeated.

In Billas *et al* (2020) the authors quantify the alanine quality correction factor for the presence of a magnetic field as:

$$k_{\text{al},\vec{B},Q} = \frac{D_{w,Q}^{\vec{B}}}{D_{w,Q}} \cdot \frac{M_{\text{al},Q}}{M_{\text{al},Q}^{\vec{B}}} = c_{\vec{B}} \cdot \frac{M_{\text{al},Q}}{M_{\text{al},Q}^{\vec{B}}}. \quad (11)$$

In this,  $M_{\text{al},Q}$  is the alanine EPR signal for the alanine pellets irradiated without the influence of a magnetic field and  $M_{\text{al},Q}^{\vec{B}}$  for the pellets irradiated under the influence of a magnetic field.  $k_{\text{al},\vec{B},Q}$  was calculated based on the described measurements.

### 2.6. Calculation of uncertainties

Uncertainties given for  $k_{\perp,Q}$  and  $c_{\text{rot}}$  have been estimated by the standard error of the mean (SEM) (JCGM 2008). The uncertainty for  $k_{\parallel}$  results from the propagation of the uncertainty of  $k_{\perp,Q=7\text{ MV}}$  and  $c_{\text{rot}}$ . All these values result from relative measurements that were repeated five times.

The uncertainty for  $k_{\text{alanine}}$  was calculated based on a full uncertainty budget. The uncertainties for  $N$ ,  $k_p$ ,  $k_Q$  and  $k_s$  are given in table 7. The uncertainty for  $c_{\vec{B}}$  includes the Monte Carlo variance as well as an additional uncertainty of 0.2%, considering the possibility of systematic Monte Carlo uncertainties (Wulff *et al* 2010). Uncertainties for temperature and atmospheric pressure measurements were calculated based on information given by the manufacturer of the measuring instruments. Additional uncertainties were included for positioning, the electrometer as well as the dose values obtained by alanine dosimetry.

The uncertainty budget for the absorbed dose to water based on an individual alanine measurement was described in detail in the literature (Anton 2006). In this work, the determination of the uncertainty for  $D_{\text{alanine}}$  was divided into two intermediate steps. In a first step, the uncertainty of the mean dose measured at each pellet position was calculated by propagation of the uncertainty, based on the five individual measurements. In a second step, the uncertainty for  $D_{\text{alanine}}$  was calculated by applying propagation of the uncertainty to the polynomial regression that was applied to the mean dose values. A brief overview of the uncertainty budget is given in table 4.

For the calculation of the uncertainty of alanine correction factor  $k_{\text{al},\vec{B},Q}$  propagation of uncertainty was applied to the uncertainty of  $c_{\vec{B}}$  and the alanine EPR signal described by Anton (2006).

## 3. Results

### 3.1. Magnetic field correction factors for parallel orientations

Figure 3 shows the results of the linear regression for  $k_{\perp,Q}$  over  $\text{TPR}_{20,10}$ . All linear regressions resulted in a coefficient of determination of  $R^2 > 0.99$ .

The results for  $k_{\perp,Q=7\text{ MV}}$  are shown in table 5.

The Farmer ionization chamber PTW 30013, which has the largest volume among the investigated thimble-type chambers, showed a 2.9% increase in response in the magnetic field. Comparing the different chambers of the same type, the two PTW 30013 ionization chambers show a very small variability in  $k_{\perp,Q=7\text{ MV}}$ , which is below 0.1%.

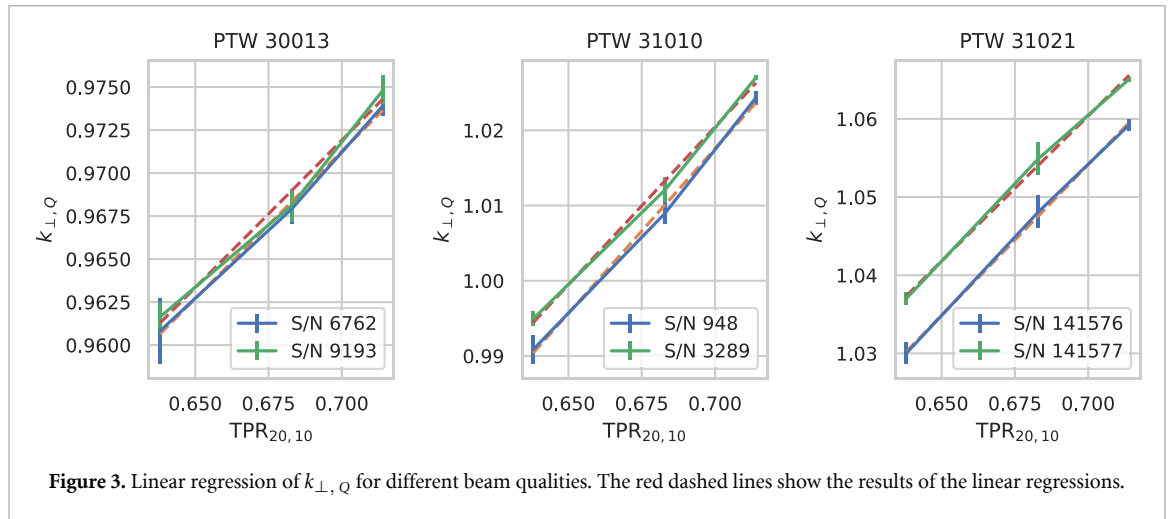


Figure 3. Linear regression of  $k_{\perp,Q}$  for different beam qualities. The red dashed lines show the results of the linear regressions.

Table 5. Experimental values for  $k_{\perp,Q=7\text{MV}}$  and  $k_{\vec{B},Q}$  for the measurements in perpendicular orientation (figure 1).

Detector	S/N	$k_{\perp,Q=7\text{MV}}$	$k_{\perp,Q=7\text{MV}} c_{\vec{B}} = k_{\vec{B},Q}$
PTW 30013	006762	0.97140(95)	0.9652(22)
PTW 30013	009193	0.9720(11)	0.9658(22)
PTW 31010	0948	1.0179(22)	1.0114(30)
PTW 31010	03289	1.0208(22)	1.0142(30)
PTW 31021	141576	1.0546(18)	1.0478(28)
PTW 31021	141577	1.0608(17)	1.0540(27)

Table 6. Experimental values for  $c_{\text{rot}}$  and  $k_{\parallel}$ .

Detector	S/N	$c_{\text{rot}}$	$k_{\parallel}$	$k_{\parallel} c_{\vec{B}} = k_{\vec{B},Q}$
PTW 30013	006762	1.02840(38)	0.9990(10)	0.9926(22)
PTW 30013	010389	1.02889(57)		
PTW 31010	03289	0.97952(90)	0.9999(23)	0.9935(31)
PTW 31010	007525	0.97661(66)		
PTW 31021	141576	0.93914(61)	0.9904(18)	0.9841(27)
PTW 31021	142175	0.94076(75)		

A mean reduction of the response amounting to 1.9% was observed for the smaller PTW 31010 ionization chamber. This is only a minor effect compared to the increase seen for the PTW 30013. Furthermore, the variability in  $k_{\perp,Q=7\text{MV}}$  is about 0.3% for this orientation.

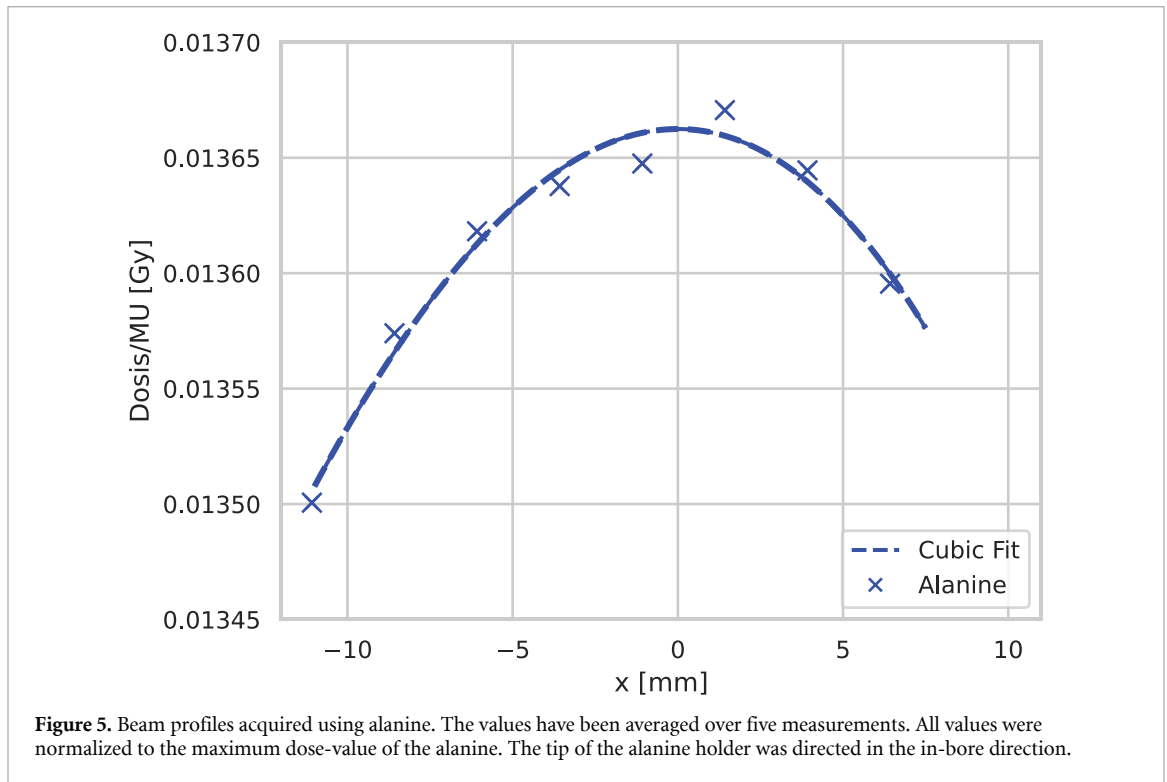
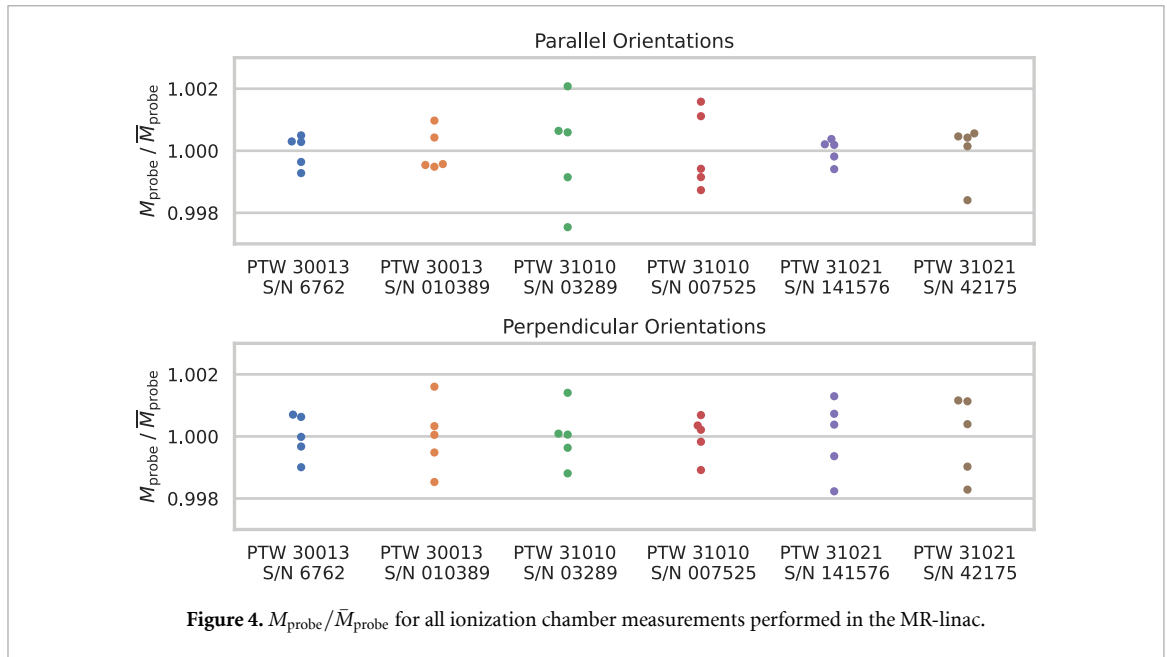
The smallest ionization chamber (PTW 31021) followed this trend with a further decrease of the response by more than 5.8%.  $k_{\perp,Q}$  differed by more than 0.6% for the two ionization chambers under investigation, for all beam qualities between 4 MV and 8 MV (see figure 3).

### 3.1.1. Magnetic field correction factors in parallel orientation

Figure 4 shows measured signals  $M_{\text{probe}}$  corrected for temperature and atmospheric pressure for all ionization chamber measurements conducted in the MR-linac. The values were normalized to the average value over all measurements using the same ionization chamber, in the same orientation  $\bar{M}_{\text{probe}}$ . The distribution of  $M_{\text{probe}}/\bar{M}_{\text{probe}}$  can be interpreted as a quantification of the experimental reproducibility. All values are within 0.3%, for both orientations and all ionization chambers.

The values for  $c_{\text{rot}}$  and  $k_{\parallel}$  are shown in table 6. The change of the orientation of the Farmer ionization chamber PTW 30013 from parallel to perpendicular increased the response by 2.9%. Again, the opposite effect was observed for the smaller ionization chambers PTW 31010 and PTW 31021. For the PTW 31010 the response decreases by about 2.1% and for the PTW 31021 by 6.0%. No significant intra-type variations for the ionization chambers used were observed. Tables 5 and 6 also include values for  $k_{\vec{B},Q}$ . For this  $k_{\perp,Q=7\text{MV}}$  was multiplied with the same  $c_{\vec{B}}$  that was calculated by Monte Carlo for the determination of  $k_{\text{alanine}}$ .

The total influence of the magnetic field on the response of the ionization chambers was between 0.7% and 1.6% for the parallel orientation.



### 3.2. Magnetic field correction factors based on alanine measurements

Figure 5 shows the beam profile acquired with the alanine measurements. The maximum dose per MU was found between the position of the third and fourth alanine pellet as  $D_{\text{max}} = 0.01366 \text{ GyMU}^{-1}$ .

The values for all correction factors can be found in table 7. The most prominent correction was the correction for the beam quality  $k_Q$ , whereas  $k_{\text{alanine}}$  (see equation (10)) quantifies the total influence of the magnetic field on the signal of the ionization chamber.

The simulation of the influence of the magnetic field on the dose resulted in  $c_{\vec{B}} = 0.9936(20)$ .

### 3.3. Magnetic field correction factors for alanine

The direct measurement of the alanine quality correction factor for the presence of a magnetic field ( $k_{\text{al},\vec{B},Q}$ ) resulted in  $k_{\text{al},\vec{B},Q} = 1.0010(28)$  and  $k_{\text{al},\vec{B},Q} = 0.9989(28)$  for the parallel and perpendicular orientation, respectively. The results for the parallel orientation was used for the determination of  $k_{\text{alanine}}$ .

**Table 7.** Quantities needed for the determination of  $k_{\text{alanine}}$ , as well as the results for  $k_{\text{alanine}}$  and  $k_{\vec{B},Q}$ .

Detector	PTW 30013	PTW 31010	PTW 31021
S/N	006762	03289	141576
$k_p$	1.0000(12)	0.9990(11)	0.9965(12)
$k_Q$	0.9851(62)	0.9845(62)	0.9865(62)
$k_s$	1.00563(51)	1.00361(51)	1.00432(51)
$k_V$	1.0033(10)	1.0003(10)	1.0002(10)
$N$ ( $\mu\text{Gy C}^{-1}$ )	0.5384(14)	2.9530(74)	5.776(15)
$k_{\text{alanine}}$	0.9965(80)	1.0019(80)	0.9949(80)
$k_{\text{alanine}}c_{\vec{B}} = k_{\vec{B},Q}$	0.9901(72)	0.9955(72)	0.9885(71)

## 4. Discussion

This work utilized alanine dosimetry as well as high precision measurements inside an electromagnet in a conventional linac for the determination of magnetic field correction factors  $k_{\vec{B},Q}$  for several ionization chambers.  $k_{\vec{B},Q}$  was measured for the parallel ionization chamber orientation (figure 1). This was done for Farmer type as well as for small volume ionization chambers. For this purpose, two independent methods were presented and described in detail.

Several parameters presented in this work quantify the reproducibility of the proposed methods. The results based on measurements in the electromagnet showed an SEM below 0.3% for all measurements. This was already shown for other magnetic flux densities in a previous publication (Pojtinger *et al* 2019). To quantify the reproducibility of the experiments at the MR-linac, we have determined the ratio  $M_{\text{probe}}/\bar{M}_{\text{probe}}$ . As the measurements at the MR-linac were carried out on three different days, this value gives a representative impression of the stability of the internal monitor chamber.  $M_{\text{probe}}/\bar{M}_{\text{probe}}$  was shown to vary by at most  $\pm 0.3\%$  for all measurements, proving a high level of repeatability and reproducibility.

Figure 4 gives an impression about the accuracy (and precision) of the positioning. The maximum of the alanine beam profile has an offset of 1 mm to the fourth alanine pellet. As the alanine holder is designed like a Farmer-type ionization chamber and was positioned in the same way as the ionization chambers, it can be speculated, that there was an offset in the in-bore direction of approximately 1 mm during the ionization chamber measurement.

In contrast to the work of Billas *et al* (2020) our investigations show, that measurements based on alanine dosimetry are not influenced by a 1.5 T magnetic field for a 7 MV beam quality. Billas *et al* (2020) reported that the alanine quality correction factor for the presence of a magnetic field might depend on the used alanine holder, this could be the reason for the observed discrepancy.

$k_{\parallel}$  can be directly compared to  $k_{\text{alanine}}$ . All presented values agree within the estimated uncertainties. Nevertheless, it must be mentioned that the uncertainty for  $k_{\text{alanine}}$  is large (0.80%). As shown in table 7, the highest contribution to the total uncertainty value is introduced by the correction for the beam quality. Anyway, this uncertainty is still comparable to the uncertainties of the values that are currently available in literature that in many cases are not based on a full uncertainty budget.

Recently, van Asselen *et al* (2018) have also determined values for  $k_{\vec{B},M,Q}$  for the Farmer ionization chamber PTW 30013. All values agree within the given uncertainty. In addition, all values presented for  $k_{\vec{B},Q}$  for the ionization chamber PTW 30013 are in agreement with the measurements of de Prez *et al* (2019).

Furthermore, this work confirms the value of  $c_{\vec{B}}$  that was calculated by van Asselen *et al* (2018). van Asselen *et al* (2018) have used the treatment planning software for the determination of  $c_{\vec{B}}$ . This work confirms the published value using the more accurate Monte Carlo algorithm implemented in EGSnrc. The value presented in this work also agrees with the value calculated by O'Brien *et al* (2016), which was calculated using Geant4.

All ionization chambers that were used for the experiments in this study have a similar radius of the sensitive volume but differ in length (table 1). Therefore, some assumptions can be derived from results, for the influence of the length of the sensitive volume of ionization chambers on magnetic field correction factors. In perpendicular orientations, the response of ionization chambers is increased for thimble-type ionization chambers with a long sensitive volume (like Farmer type ionization chambers). For short ionization chambers, the response is more likely to be decreased instead of increased. Also, short ionization chambers show a higher variability in  $k_{\vec{B},Q}$ . The measurements involving the two PTW 31021 ionization chambers show a variability in  $k_{\vec{B},Q}$  of more than 0.6%.

## 5. Conclusion

Two methods for the determination of magnetic field correction factors for ionization chambers for parallel and perpendicular orientations have been presented. One method is based on alanine dosimetry, the other method combines measurements inside an electromagnet with measurements inside an MR-linac. Both methods showed an excellent reproducibility and are thus suited for clinical usage in MR-guided radiotherapy.

## Acknowledgments

Parts of this work were funded by the German Research Council (DFG, ZI 736/2-1). M Nachbar and D Thorwarth report institutional collaborations with Elekta, Philips and PTW Freiburg.

We are grateful for the technical support of Larissa Meyer, Markus Meier, Markus Schrader and Thomas Hackel (PTB, Braunschweig, Germany), who greatly assisted the experimental work. The measurements at the Hôpital Riviera-Chablais were supported by Thierry Buchillier, Claude Bailat (IRA, Lausanne, Switzerland) and Neil Dodd (Elekta AB, Stockholm, Sweden). We thank Ilias Billas (NPL, Teddington, England) for providing measurement equipment for our measurements at the Hôpital Riviera-Chablais.

Furthermore, we acknowledge the support provided by the state of Baden-Württemberg through bwHPC and by the German Research Foundation (DFG) through Grant No. INST 39/963-1 FUGG. This work is part of the project (MRgRT-DOS) that has received funding from the EMPIR programme co-financed by the Participating States and from the European Union's Horizon 2020 research and innovation programme.

## ORCID iD

Stefan Pojtinger  <https://orcid.org/0000-0001-6397-4572>

## References

- Andreo P et al 2020 Determination of consensus  $k_Q$  values for megavoltage photon beams for the update of IAEA TRS-398 *Phys. Med. Biol.* **65** 095011
- Andreo P, Huq M S, Kanai T, Laitano F, Smyth V, Zealand N, Vynckier S, Burns D T and Hohlfield K 2006 IAEA TRS-398: *Absorbed Dose Determination in External Beam Radiotherapy: An International Code of Practice for Dosimetry based on Standards of Absorbed Dose to Water* vol 2004
- Anton M 2005 Development of a secondary standard for the absorbed dose to water based on the alanine EPR dosimetry system *Appl. Radiat. Isot.* **62** 779–95
- Anton M 2006 Uncertainties in alanine/ESR dosimetry at the Physikalisch-Technische Bundesanstalt *Phys. Med. Biol.* **51** 5419–40
- Billas I, Bouchard H, Oelfke U, Shipley D R, Gouldstone C A and Duane S 2020 Alanine dosimetry in strong magnetic fields: use as a transfer standard in MRI-guided radiotherapy *Phys. Med. Biol.* **10.1088/1361-6560/ab8148**
- Billas I, Costa D, Perik T, Kaas J and Duane S 2017 Determination of the magnetic field correction factor for ionisation chambers in an MR-Linac using alanine dosimetry *Proc. 5th MRinRT Symp.*
- de Prez L, Woodings S, de Pooter J, van Asselen B, Wolthaus J, Jansen B and Raaymakers B 2019 Direct measurement of ion chamber correction factors,  $k_Q$  and  $k_B$ , in a 7 MV MRI-linac *Phys. Med. Biol.* **64** 105025
- Delfs B, Schoenfeld A A, Poppinga D, Kapsch R P, Jiang P, Harder D, Poppe B and Looe H K 2018 Magnetic fields are causing small, but significant changes of the radiochromic EBT3 film response to 6 MV photons *Phys. Med. Biol.* **63** 035028
- Friedel M, Nachbar M, Mönnich D, Dohm O and Thorwarth D 2019 Development and validation of a 1.5 T MR-Linac full accelerator head and cryostat model for Monte Carlo dose simulations *Med. Phys.* **46** 5304–13
- Gohil P, Agnew J, Berresford J, Budgell G, Billas I and Duane S 2018 PO-0885: measurement of magnetic field correction factors for multiple radiation detectors for MR linacs *Radiother. Oncol.* **127** S468–9
- IAEA and AAPM 2017 TRS-483: *Dosimetry of Small Static Fields Used in External Beam Radiotherapy: an International Code of Practice for Reference and Relative Dose Determination* (Vienna: IAEA)
- JCGM 2008 JCGM 100:2008, *Evaluation of Measurement Data: Guide to the Expression of Uncertainty in Measurement* (JCGM)
- Kapsch R P and Krauss A 2009 On the performance of monitor chambers to measure the output of medical linear accelerators for high-precision dosimetric investigations *IFMBE Proc.* **25** 85–88
- Kawrakow I, Mainegra-Hing E, Rogers D W O, Tessier F and Walters B R B 2019 *The EGSnrc Code System: Monte Carlo Simulation of Electron and Photon Transport*
- Krauss A and Kapsch R P 2014 Experimental determination of  $k_Q$  factors for cylindrical ionization chambers in 10 cm × 10 cm and 3 cm × 3 cm photon beams from 4 MV to 25 MV *Phys. Med. Biol.* **59** 4227–46
- Malkov V N and Rogers D W O 2018 Monte Carlo study of ionization chamber magnetic field correction factors as a function of angle and beam quality *Med. Phys.* **45** 908–25
- Meijsing I, Raaymakers B W, Raaijmakers A J E, Kok J G M, Hogeweg L, Liu B and Lagendijk J J W 2009 Dosimetry for the MRI accelerator: the impact of a magnetic field on the response of a Farmer NE2571 ionization chamber *Phys. Med. Biol.* **54** 2993–3002
- O'Brien D J, Roberts D A, Ibbott G S and Sawakuchi G O 2016 Reference dosimetry in magnetic fields: formalism and ionization chamber correction factors *Med. Phys.* **43** 4915–27
- Pojtinger S, Dohm O S, Kapsch R-P and Thorwarth D 2018 Ionization chamber correction factors for MR-linacs *Phys. Med. Biol.* **63** 11NT03

- Pojtinger S, Kapsch R-P, Dohm O S and Thorwarth D 2019 A finite element method for the determination of the relative response of ionization chambers in MR-linacs: simulation and experimental validation up to 1.5 T *Phys. Med. Biol.* **64** 135011
- Rogers D W O, Walters B and Kawrakow I 2018 *BEAMnrc Users Manual*
- Smit K, van Asselen B, Kok J G M, Aalbers A H L, Legendijk J J W and Raaymakers B W 2013 Towards reference dosimetry for the MR-linac: magnetic field correction of the ionization chamber reading *Phys. Med. Biol.* **58** 5945–57
- Spindeldreier C K, Schrenk O, Bakenecker A, Kawrakow I, Burigo L, Karger C P, Greilich S and Pfaffenberger A 2017 Radiation dosimetry in magnetic fields with Farmer-type ionization chambers: determination of magnetic field correction factors for different magnetic field strengths and field orientations *Phys. Med. Biol.* **62** 6708–28
- van Asselen B, Woodings S J, Hackett S L, Van Soest T L, Kok J G M, Raaymakers B W and Wolthaus J W H 2018 A formalism for reference dosimetry in photon beams in the presence of a magnetic field *Phys. Med. Biol.* **63** 125008
- Wulff J, Heverhagen J T, Zink K and Kawrakow I 2010 Investigation of systematic uncertainties in Monte Carlo-calculated beam quality correction factors *Phys. Med. Biol.* **55** 4481–93
- Wulff J, Zink K and Kawrakow I 2008 Efficiency improvements for ion chamber calculations in high energy photon beams *Med. Phys.* **35** 1328–36